Role of Disorder in Quantum Crystals

A THESIS
SUBMITTED TO THE FACULTY OF THE GRADUATE SCHOOL
OF THE UNIVERSITY OF MINNESOTA
BY

Abdul Naseer Malmi Kakkada

IN PARTIAL FULFILLMENT OF THE REQUIREMENTS
FOR THE DEGREE OF
Doctor of Philosophy

Oriol T. Valls

August, 2015

Acknowledgements

Much gratitude and appreciation is owed to my advisor Dr. Oriol Valls from whom I learned a lot. I thank him for teaching me how to do research. His guidance, support and encouragement made this thesis possible. I thank Dr. Chandan Dasgupta for his help and guidance throughout graduate school. I would also like to thank my committee members, Dr. Jorge Vinals, Dr. James Kakalios and Dr. Robert Gehrz. I also thank Dr. Yuichi Kubota for his mentoring and assistance in the beginning years of graduate school.

There are many people that have earned my gratitude for their contribution during my time in graduate school. I particularly thank Dr. Imran Hayee and family for providing a home away from home in Minnesota. I thank my friends Chien-Te Wu, Gaurav Shukla, Ilana Percher, Xiaowei Zhang and many others.

A special thank you to my family whose support made this work possible. Your prayers sustain and inspire me. I owe special appreciation to my spouse, Touba Khurshid, whose love, companionship and care always provided a source of support.

Dedication

"No incongruity canst thou see in the creation of the Gracious God. Then look again: Seest thou any flaw?" The Holy Qur'an 67:4.

Abstract

I investigate the role of disorder and its impact on the properties of a novel quantum crystal: solid ^{4}He. The role of a superfluid field associated with edge dislocations on the properties of ^{4}He crystal is studied at different levels of coarse graining.

Initially, a study of the hydrodynamics of compressible superfluids in confined geometries as a coarse grained representation of superfluidity confined to complex networks is presented. The corrections due to finite compressibility to superfluid flow behavior are, as expected, negligible for liquid He. They are important but amenable to the perturbative treatment for typical ultracold atomic systems.

Next, a study of the equilibrium properties of an Ising model on a disordered random network with quenched or annealed disorder is presented. The emphasis is on nonuniversal properties and we consider the transition temperature and other equilibrium thermodynamic properties, including those associated with one dimensional fluctuations arising from the chains. The transition temperature and the entropy associated with one dimensional fluctuations are always higher for quenched disorder than in the annealed case. These differences increase with the strength of the disorder up to a saturating value.

The effect of the superfluid field on dislocation motion as a result of stress applied on the crystal is also studied. Damping of the dislocation motion, calculated in the presence of the superfluid field, is related to the shear modulus of the crystal. As the temperature increases, we find that a sharp drop in the shear modulus will occur at the temperature where the superfluid field disappears. We relate the drop in shear modulus of the crystal arising from the temperature dependence of the damping contribution due to the superfluid field, to the experimental observation of the same phenomena in solid ^{4}He and find good agreement.

The response of the superfluid field to dislocation motion is studied within the quantum Gross-Pitaevskii formalism. The Dissipative Gross-Pitaevskii equation is used to investigate the effect of dislocation climb and glide motion on the superfluid field near it. Asymmetry introduced in the superfluid distribution due to dislocation climb

is quantified. Unlike climb, glide motion does not affect the asymmetry characteristic of the superfluid distribution in the vicinity of an edge dislocation.

Contents

List of Figures

Chapter 1

Introduction

1.1 Basics of superfluidity

In 1938, Pyotr Kapitza [1] and independently J.F. Allen and A.D. Misener [2] discovered superfluidity in ^{4}He. At 2.17K, liquid ^{4}He undergoes a phase transition into a superfluid state characterized by frictionless flow [1]. Superfluidity is observed in both ^{4}He and ^{3}He whereas the underlying mechanism responsible for superfluidity in both the isotopes is vastly different owing to their respective bosonic and fermionic nature. Superfluidity in ^{4}He is characterized by a condensate analogous to Bose-Einstein Condensation (i.e. the tendency of bosonic particles to occupy the lowest energy single particle state at low temperatures) in non-interacting systems. However, the density of ^{4}He atoms in the ground state (ρ_0) is not equal to the superfluid density(ρ_s). In fact, at T$\sim$ 0K, ρ_0 is approximately 10% of the total density while $\frac{\rho_s}{\rho} \sim 1$. On the other hand, ^{3}He being fermionic - owing to an odd number of nucleons - form Cooper pairs in order to turn superfluid [3].

Superfluidity is a state of matter in which a fluid is characterized by zero viscosity. Due to the ability of superfluids to flow without friction, a container which seemed to be leak tight could start to leak helium as the superfluid can now move through a microscopic hole. When liquid ^{4}He is rotated in a container at some angular velocity, the superfluid component (ρ_s) will not rotate with the container because it feels no friction from the walls of the container. Hess and Fairbanks [4] conducted an experiment in which liquid ^{4}He in a rotating cylinder was cooled through the superfluid transition

temperature, referred to as T_λ. They observed that at sufficiently low angular velocities, superfluid forms in a state of zero angular momentum causing the container to rotate faster. Also, the temperature dependent moment of inertia, I(T), was understood to depend on the superfluid density fraction $\frac{\rho_s}{\rho}$ as:

$$I(T) = I_{Classical}[1 - \frac{\rho_s}{\rho}]. \tag{1.1}$$

This unique property of the dependence of moment of inertia on superfluid density is referred to as Non Classical Rotational Inertia (NCRI).

1.2 From Liquid to Solid ^{4}He

Helium at its own vapor pressure is the only substance known to resist solidification down to the lowest of temperatures [5]. This property of ^{4}He is due to a quantum mechanical effect called zero point motion where atoms in a crystal vibrate down to the lowest of temperatures. Atoms in a crystal with lattice spacing, a, possess kinetic energy due to vibrational motion

$$E_{kinetic} = \frac{\hbar^2}{ma^2} \tag{1.2}$$

where $\hbar$ is the Planck's constant and m the atomic mass. Comparing the kinetic energy to the interaction energy, α, between atoms in the crystal one obtains a dimensionless parameter (referred to as the de Boer parameter [6]),

$$\Lambda = (\frac{E_{kinetic}}{E_{interaction}})^{1/2} = \frac{\hbar}{\sqrt{m\alpha}a}. \tag{1.3}$$

Larger values of Λ imply that kinetic energy of atoms is dominant compared to the interaction energy. Since kinetic energy is associated with the vibrational motion of the atoms, the larger the amplitude of vibrations the harder it will be to localize atoms in the low temperature limit. Values of $\Lambda \geq 0.2 - 0.3$ implies that the crystal is unstable with respect to zero point motion even at T $\rightarrow$ 0, a phenomenon referred to as quantum melting[6]. The parameter Λ can therefore be used as a measure of how 'quantum' a crystal is. The solid phase of ^{4}He with $\Lambda \approx 0.4$ is, therefore, an excellent candidate for a quantum crystal. This property of solid ^{4}He also means that the solid phase is

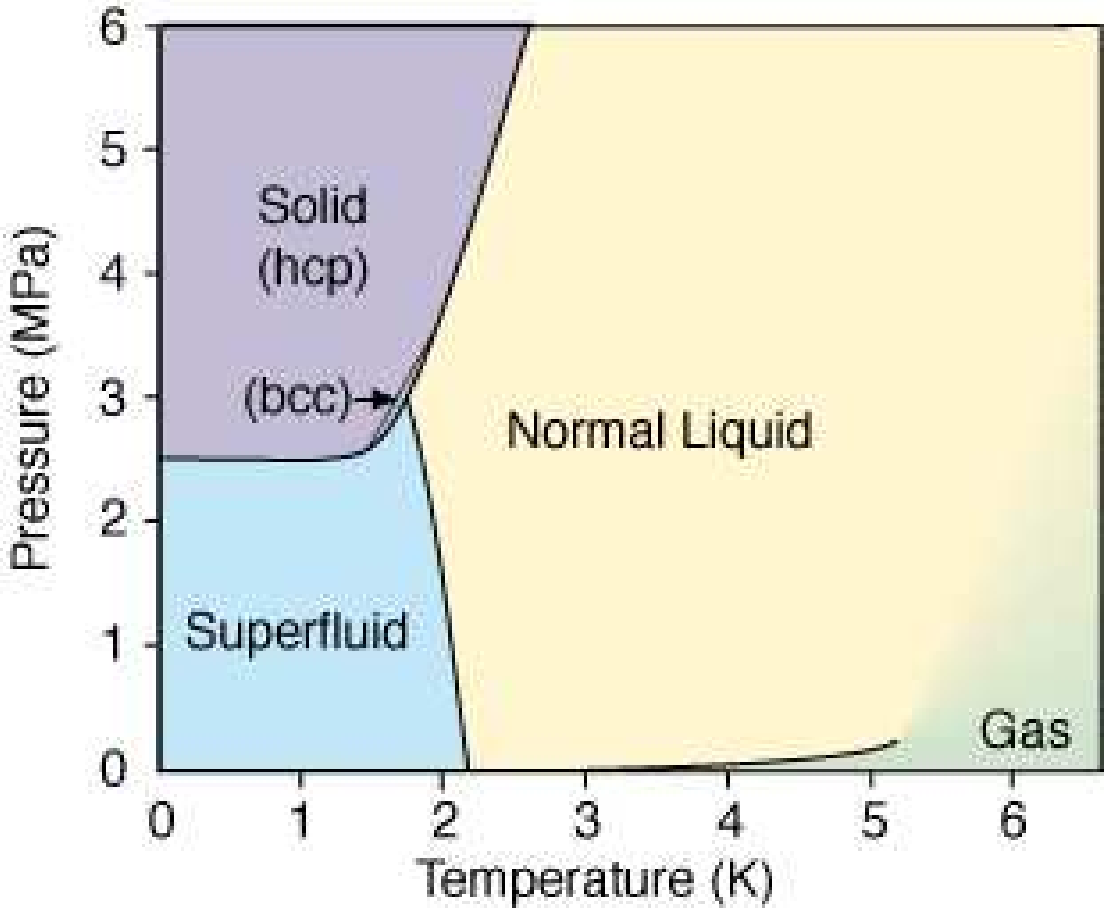

Figure 1.1: Phase Diagram of ^{4}Helium below 6K.

only attained at very high pressures - above 2.5 MPa - and very low temperatures. See Fig. 1.1 for the phase diagram of ^{4}He [7].

Given the quantum nature of solid ^{4}He, theorists began to ponder about the possibility of a phenomenon similar to superfluidity in solid ^{4}He where part of the crystal could 'flow' without friction. As early as the 1960s, Chester proposed how a crystal could undergo Bose-Einstein condensation [8] thereby forming a 'super'solid. Following the initial predictions by Chester, Leggett proposed how a NCRI signal could be utilized in order to experimentally detect supersolidity [9]. However, finding a sensitive probe to observe the onset of NCRI turned out be particularly challenging partly due to the difficulties associated with solidifying ^{4}He. Efforts at observing NCRI via measurements of mobility, heat transfer, and other methods turned out to be futile [10]. Eventually, Kim and Chan [11], utilizing a torsional oscillator technique that is extremely sensitive to changes in the moment of inertia claimed to have observed NCRI in solid ^{4}He. This purported observation of NCRI in solid ^{4}He renewed the experimental and theoretical interest on topics relating to the quantum nature of ^{4}He crystals.

More recently, however, the validity of the observation of period drop in torsional oscillator experiments attributed to NCRI in solid ^{4}He has been called into question. This is because solid ^{4}He was also shown to undergo an anomalous softening of the shear modulus in the same temperature range as the purported observation of NCRI: a phenomenon referred to as "quantum plasticity" [12]. Most recent experimental results suggest that the anomalous drop in shear modulus of ^{4}He crystal rather than the change in inertial mass set into motion by the oscillator maybe responsible for the observed drop in the period in torsional oscillator experiments [13, 14]. Other alternative theories have also been proposed. For instance, it has been argued [15] that some of the experimental results can be understood in terms of a phenomenological description of glassy response of the solid. As such, the question of whether or not NCRI effect exists in solid ^{4}He continues to be a controversial topic. Experimental evidence [16] for superfluidlike mass transport through solid ^{4}He was initially reported in Ref. [17]. Observation of mass superflow in solid ^{4}He, using an experimental technique other than the torsion oscillator method, further added to the controversy on whether or not NCRI exists. Considering these recent developments, it is clear that even though torsional oscillator experiments may not provide conclusive evidence for NCRI in solid ^{4}He, other phenomena such

as superfluidlike transport associated with crystal disorder and quantum plasticity are equally interesting.

The observed anomalous drop in shear modulus of ^{4}He crystal brought into focus the role that defects and disorder present within the crystal may play. Given that the mechanical properties of crystals are largely dictated by dislocation lines and other defects present within the crystal, the observed anomalous shear modulus behavior can provide fundamental insights into the behavior of defects in quantum crystals such as solid ^{4}He. Moreover, some of the features associated with the behavior of defects in solid ^{4}He crystal may be due to quantum crystalline effects and therefore not be ordinarily observed in classical crystals. For example, Ref. [18] studied a phenomenological model coupling superfluidity to the elastic field associated with a dislocation line. It was observed that the coupling induced a local variation of the superfluid transition temperature: the presence of a dislocation line enhanced the superfluid transition temperature in its vicinity. Thus, questions involving the nature of the defects and its coupling to a superfluid field are at the core of the basic physical issues that are addressed in this thesis.

1.3 Disorder in Solid ^{4}He Crystals

Crystals found in nature contain imperfections which could be categorized as point, line, surface or volume defects. Examples of point defects are vacancy sites or interstitial atoms while dislocation lines are examples of line defects. The presence of such defects can significantly alter the properties of crystalline materials. Although we focus specifically in this thesis on dislocation lines, we note that the various types of defects present within a crystal could interact with one another and are therefore related.

Dislocation lines are line defects that arise either during crystal growth or due to mechanical deformation of a crystal. Different types of dislocation lines exist. Two common types of dislocation lines found in crystals are edge and screw dislocations. These defects in the crystal structure can also affect properties such as thermal and electrical conductivity of a material. A characteristic length associated with a dislocation line is the Burgers vector. The Burgers vector is defined as the vector needed to close a Burgers circuit which is any atom-to-atom path taken around a dislocation line and

forms a closed loop [19]. The Burgers vector for an edge dislocation is normal to the line of the dislocation.

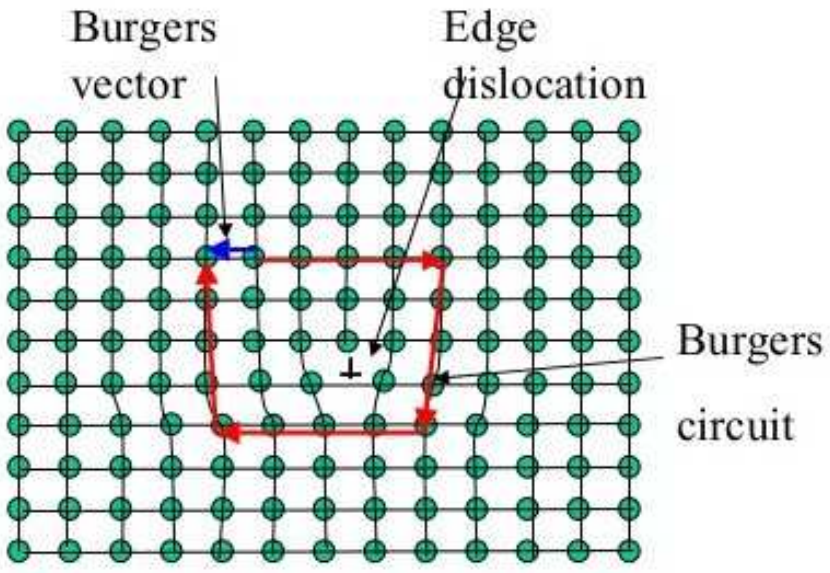

Figure 1.2: An edge dislocation line in a crystal. The extra half plane within an otherwise ordered crystal arrangement forms an edge dislocation.

Dislocation lines can move within a crystal in response to an applied stress. When dislocations move along a surface that contains the dislocation line and the Burgers vector, it is said to execute gliding motion. Glide of dislocations could result in slip which is a manifestation of plastic deformation in a crystal. Movement of a dislocation line out of the glide surface, therefore, normal to the Burgers vector is referred to as climb.

1.3.1 Dislocation Networks, ^{3}He Impurities and Superfluidity

It has been known since the 1980s that ^{3}He impurities pin dislocation lines in ^{4}He crystals [20]. Pinning and depinning of dislocation lines by ^{3}He impurities is thought to be evident from its effect on elastic properties of ^{4}He crystals. It was observed that ^{4}He crystals become soft [21] in the absence of pinning due to ^{3}He impurities which

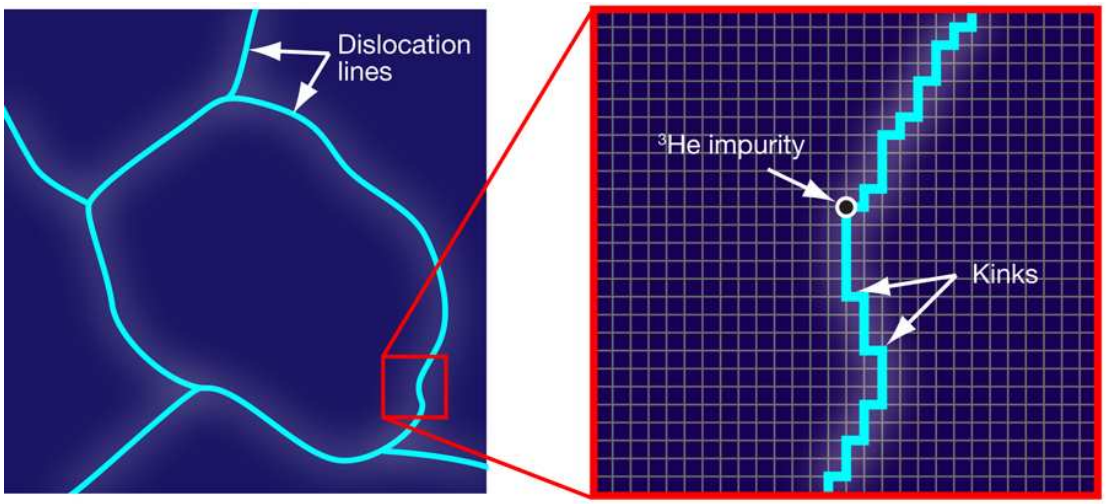

Figure 1.3: Dislocation lines in a crystal and how ^{3}He binds to dislocation lines.

correspond to a situation whereby dislocation lines are free to move. This is reminiscent of a technique used in past whereby impurities were introduced into a crystal to act as pinning centers. These pinning centers would then lock dislocations into place thereby limiting the motion of dislocation lines. This would result in improving the ability of materials to resist plastic deformation. Fig. 1.3 gives an illustration of dislocation lines within a crystal and how an example of a point defect interacts with it [22]. ^{3}He impurities present within the crystal pin dislocation lines and thereby influence the elastic properties of a crystal.

Another clue as to the role of defects in solid ^{4}He came from the purported observation of NCRI in solid ^{4}He and its sensitivity to defects present within the crystal. It was hypothesized that superfluid ^{4}He wets the area between crystalline grains and their superflow could result in NCRI [23]. This is an example of an effort to incorporate crystalline defects and superfluidity into understanding the properties of solid ^{4}He.

The possibility of the transition of the core of dislocations in quantum crystals into a fluid state and the appearance of one-dimensional superfluidity along dislocation lines was looked into in Ref. [24]. More recently, computer simulations [25, 26, 27] showed that superfluidity could occur along dislocation cores. As a result, it became reasonable to consider the possibility that quantum liquid state of dislocation lines could play an

important role in quantum plasticity as well as the purported observation of superfluidlike mass flow in ^{4}He crystals. Motivated by the fact that in superconductors T_c was elevated [28] near edge dislocation lines, it was proposed that superfluidity would also be enhanced [18, 29] near a dislocation line. Considering a quenched edge dislocation with an associated superfluid field in the context of a Landau theory, it was shown [29] that superfluid ordering could take place at higher temperatures in the proximity of a dislocation line. It was observed that local compression or dilation fields associated with an edge dislocation line could increase the local transition temperature. These results in essence set the motivation for the work that is discussed in this thesis.

1.4 Theoretical Background

The primary objective of research presented in this thesis is to understand the experimentally observed quantum behavior in solid ^{4}He and the role that superfluidity induced near the cores of dislocation lines plays in dictating the quantum behavior. Motivation for our theoretical considerations will be largely based on coarse-grained models of superfluidity, similar to the models proposed by Shevchenko [24] and by Dorsey, Goldbart and Toner (DGT) [18, 29]. The strain field due to the dislocation lines is coupled to the superfluid order parameter in these models. Here I introduce the DGT model starting with a X-Y model Landau free energy of the form:

$$F = \int [\frac{1}{2} C_{\alpha\beta} \partial_\alpha \Psi \partial_\beta \Psi^* + \frac{1}{2} a(T) |\Psi|^2 + \frac{1}{4!} w |\Psi|^4] d^3 r \tag{1.4}$$

where $\Psi(r)$ (a complex scalar field) is the X-Y model order parameter and $C_{\alpha\beta}$ takes into account the spatial anisotropy of the crystal. Coupling between the X-Y order parameter and the local displacement field $\vec{u}(\vec{r})$ for the lattice points within a crystal is introduced by taking the Landau parameters in Eq.[1.4], $a(T)$ and w, to depend on the local value of $\vec{u}(\vec{r})$. If the free energy is to be invariant under rotations and translations, it can only depend on $\vec{u}(\vec{r})$ through the symmetric strain tensor $u_{\alpha\beta}(\vec{r})$[30]. Thus expanding the Landau parameter $a(T)$ in terms of the strain tensor(and doing the same for w)

$$a(T) \rightarrow a^{(0)} + a^{(2)}_{\alpha\beta\gamma\lambda} u_{\alpha\beta} u_{\gamma\lambda} \tag{1.5}$$

DGT obtained from these considerations a minimal model of free energy

$$F = \int [\frac{1}{2} C_{\alpha\beta} \partial_\alpha \Psi \partial_\beta \Psi^* + \frac{1}{2} a^{(0)} |\Psi|^2 + \frac{1}{4!} w |\Psi|^4 + \frac{1}{2} \lambda_{\alpha\beta\gamma\delta} u_{\alpha\beta} u_{\gamma\delta} + \frac{1}{2} a^{(1)}_{\alpha\beta} u_{\alpha\beta} |\Psi|^2] d^3 r \tag{1.6}$$

where $\lambda_{\alpha\beta\gamma\delta}$ are the bare elastic constants and other variables are as defined above. The last term in Eq.[1.6] above couples the X-Y order parameter to the strain tensor and therefore allows one to study the effect of the displacement field $\vec{u}(\vec{r})$ on superfluidity within a crystal.

Strain fields $u_{\alpha\beta}(\vec{r})$ in a crystal result from dislocations. In studying the effect of dislocations on the X-Y order parameter, an appropriate expression for $u_{\alpha\beta}(\vec{r})$ arising from dislocations within a crystal should be considered. Toner [29] considered a straight edge dislocation with a corresponding strain field of the form

$$u_{\alpha\alpha} = \frac{4\Sigma}{2\Sigma + \lambda} \frac{b \cos\theta}{r_\perp} \tag{1.7}$$

where $\vec{b}$ is the Burgers vector along the y-axis (for an edge dislocation running along the z axis) and Σ, λ are elastic constants. Based on the DGT free energy above, Ref. [29] looked at the role that strain due to quenched dislocation would play in the superfluid to normal fluid transition of associated ^{4}He atoms. It was shown that edge dislocations can enhance the normal to superfluid transition. These models, in general, couple the strain field($u_{\alpha\beta}$) of quenched (stationary) dislocations to the X-Y order parameter $\Psi(r)$ and do not include the dynamics of dislocation lines. The network of dislocation lines is assumed to be 'quenched' (frozen in time). Results presented in this thesis will therefore delve into studying scenarios when this assumption is relaxed and the dynamics of the network of dislocation lines is taken to be relevant.

1.5 Dynamics of Defects

In this section, the question of how the dynamics of a coupled system of the superfluid order parameter and the dislocation lines can be modeled is addressed. As discussed in detail in subsequent chapters of this thesis, this question will be addressed, both analytically and numerically, at different levels of coarse-graining. An important issue in this context is how the motion of dislocation line affects superfluidity in its vicinity. It has been suggested [22] that a moving dislocation line is less effective compared to a stationary one in causing the ^{4}He atoms around it to become superfluid. The suggestion appears reasonable assuming that the strain field of a dislocation increases the "local transition temperature" for superfluidity. The motion of a dislocation line could then

"smear out" this effect over a wider region which may suppress the effectiveness of the dislocation line in enhancing superfluidity in comparison to a stationary dislocation line. Our results, presented below, tell us whether this actually happens.

Initially, before delving into microscropic models on the role of dynamics of defects, I studied the hydrodynamics of superfluids confined to complex geometries. This represents a very coarse-grained view of the behavior of superfluid field associated with dislocation lines in crystal ^{4}He. Motivated by experimental results associated with superfluidity in solid ^{4}He, the flow behavior of superfluid confined to complex geometries such as blocked rings, wedges and solids containing grain boundaries was studied in Ref. [31] in the incompressible limit. Understanding the flow properties of superfluid constrained to complex geometries could give interesting insights into how superfluidity associated with defects behave. This study was also partly motivated by the recent interest in experimental and theoretical studies of superfluidity and other quantum phenomena in trapped, ultracold atomic systems. We considered the case where the superfluid confined to complex geometries was characterized by finite compressibility.

Moving toward less coarse-grained models coupling superfluid field and dislocation lines, we studied analytically and numerically a coupled spin model characterized by a simplified version of the dynamics of defects. In this model, the system of dislocation lines is represented by a network of Ising spins. The superfluid order parameter is modeled by one type of Ising spins and the tendency of dislocation lines to enhance or suppress superfluidity in its vicinity is represented by a suitably chosen coupled secondary field. The equilibrium and dynamic behavior of the coupled spin model was then studied using approximate analytic methods and numerical simulations.

Next the mobility of a dislocation line in bulk crystal ^{4}He was calculated. Mobility of a dislocation line tells us how easy it is to move a dislocation line in response to an applied force. It is quite likely that given the quantum nature of solid ^{4}He crystals, dramatic effects unique to the quantum nature of the solid could be observed. Considering that solid ^{4}He has an additional Goldstone mode (in this case superflow) that couples to the elastic fields of dislocations, interesting effects relating to material properties of ^{4}He crystals may arise. Also, the superfluid velocity field must change when dislocations move which may then feed back into the dynamics of the dislocation motion itself, thereby changing its mobility. I calculate the dislocation mobility in ^{4}He crystals using

the techniques of Ref. [32]. In this approach, a gedanken experiment is performed in which a constant force F_D is applied to a dislocation, causing it to move at a constant velocity V_D. One can then solve the continuum, hydrodynamic equations of motion for the system under consideration, subject to the condition implied by the dislocation motion. In our case, these are the well-known [33, 34] hydrodynamic equations for a quantum solid. One can then obtain the force F_D -velocity - V_D relation for the dislocation by balancing the energy loss in the time-dependent dislocation fields against the work done by the external force F_D. This first analytic calculation was done for a system in which the superfluid order can develop without the aid of the dislocations. Based on the mobility calculation, a model for the temperature dependence of the anomalous shear modulus and the dissipation associated with dislocation motion was developed. These results are shown to be in agreement with experiments.

In the next calculation, I determine based on a fully quantum model how dislocation motion affects the superfluid field around it. In particular, the issue of whether dislocation motion increases or reduces the dislocation's efficacy at inducing superfluid order is analyzed. The methodology used in performing this calculation was to extend the techniques of the hydrodynamic calculation so as to include fluctuations in the amplitude of the superfluid order parameter. These are not included in the hydrodynamic equations of motion, because this amplitude is a non-hydrodynamic variable (i.e. since it relaxes quickly at long wavelengths). However, it is obviously essential to include it in order to understand how moving dislocations can induce a non-zero value of this amplitude when it is zero far from the dislocation. I extend the hydrodynamic theory [33, 34] to include such amplitude fluctuations via the Gross-Pitaevskii formalism. This extension will include excitations due to a moving dislocation line and how these excitations affect the superfluid order parameter. In this regard, the dissipative Gross-Pitaevskii formalism is an excellent framework to study how excitations associated with a moving dislocation line affects the superfluid field. After writing the equations of motion for a coupled system of superfluid field and the dislocation line, I solve it in the presence of a moving dislocation line. From this solution the position dependent amplitude of the superfluid order parameter is obtained, and learn, among other things, whether it is enhanced or suppressed, compared to the static solution, by the motion of dislocation line.

Therefore, through these various approaches, the main objective of studying how dislocation motion affects the superfluid field in its vicinity for models at different levels of coarse-graining is implemented. Relevant details of the analytic and numerical calculations performed and the results obtained are presented below in the following chapters.

- Chapter 2 describes the flow behavior of compressible superfluids confined to complex geometries.
- Chapter 3 presents a study of the coupled field spin model comparing quenched and annealed dislocation networks.
- In Chapter 4 the mobility calculation and its relation to the shear modulus of solid ^{4}He crystal is outlined. The good agreement obtained for the shear modulus and the dissipation associated with dislocation motion in solid ^{4}He in comparison to experimental results is shown.
- Chapter 5 describes the effect of dislocation motion on the superfluid field near it within the dissipative Gross-Pitaevskii formalism.

Results presented in Chapter 2, 3 are edited versions of published journal papers and a paper on Chapter is 4 currently under review. Chapter 5 is to be rewritten in paper form and submitted.

Chapter 2

Hydrodynamics of compressible superfluids in confined geometries

2.1 Introduction

The hydrodynamics of superfluids confined in containers or channels of complex geometry is relevant to a variety of experimentally studied systems. Crystalline defects such as dislocation lines in solid ^{4}He form complex disordered structures. A study of the flow properties of a superfluid confined in irregular-shaped channels could provide interesting insights into the behavior of superfluidity associated with disordered structures within crystal ^{4}He. Moreover, the absence of friction in a superfluid and the irrotational nature of superfluid flow (in the absence of vortices) lead to a variety of unusual hydrodynamic effects that depend crucially on the confining geometry.

A large number of experimental investigations into superfluidity in trapped, ultracold atomic systems [35, 36, 37] have been carried out in recent years. Various signatures of superfluidity, such as persistent flow, reduction in the moment of inertia due to the frictionless nature of the superfluid (the so-called non-classical rotational inertia (NCRI)) and formation of quantized vortices have been observed in both bosonic [38, 39, 40, 41] and fermionic [42] systems. In all these experiments, the superfluid is confined in a small region by an external trapping potential. While the early experiments on such systems were carried out for traps with simple geometry, more recent ones have begun to explore the properties of superfluid condensates in traps with a more complex

structure. Superfluid flow in a toroidal trap has been observed [40], and the effects of a repulsive optical barrier that tends to block the superflow have been investigated in recent experiments [43, 44]. Studies of superfluid hydrodynamics in containers with complex geometry are obviously relevant for understanding the results of experiments on superfluidity in atomic systems confined in such traps.

Motivation for studies of superfluid hydrodynamics in confined geometries is also provided by reports [11, 45] of an abrupt change in the resonant period of a torsional oscillator filled with solid ^{4}He, initially interpreted as NCRI in solid ^{4}He, at sufficiently low temperatures. While the interpretation is controversial [46], a possible explanation [25, 26, 18, 47] is that superfluidity occurs in solid ^{4}He along extended crystal defects such as dislocation lines and grain boundaries which form complex disordered networks. Studies of the flow properties of a superfluid confined in channels and networks of irregular geometry are obviously useful for assessing the validity of such theories.

The hydrodynamics of superfluids confined in containers of simple geometries, such as spherical, cylindrical or rectangular, has been studied extensively [48, 49] in the past. These studies, all in the incompressible limit, were recently extended [31] to more complex geometries, such as wedges and blocked rings, both in the case where there are no vortices (so that the superfluid flow is irrotational) and the case where a single vortex was present. The study [47] looked into the effects of superfluidity along grain boundaries in a two-dimensional bosonic system. While the results of these studies could be applied to experiments involving superfluid ^{4}He, they were not directly applicable to cold atomic systems because of the incompressibility assumption. This assumption constrains the local density in equilibrium to be uniform throughout the system. While this is an extremely good approximation for superfluid ^{4}He, it is not a good one for cold atomic systems in which the presence of a confining potential causes the equilibrium density to be substantially inhomogeneous. This inhomogeneity has significant effects on the superfluid properties of the confined atomic system, as found in both experimental [35] and theoretical [50, 51] investigations. Therefore, it was doubtful if the results of these earlier studies [47, 31] would be valid for cold atomic systems. For example, calculations in Ref. [31] showed that the velocity field for a superfluid confined in a two-dimensional wedge with opening angle $\beta > \pi$ diverges at the tip of the wedge for *any* nonzero value of the angular velocity Ω of the wedge about an axis perpendicular

to it and passing through its tip. This divergence could be removed by the nucleation of a single vortex. This implies that either a normal region near the tip of the wedge or a vortex must be present for any nonzero value of Ω. The size of the region near the tip where the velocity exceeds the critical velocity was estimated to be too small to be experimentally observable for liquid ^{4}He, but it was found that it may be observable in cold atomic systems. However, the validity of the results for cold atomic systems could not be established because the calculation was carried out for an incompressible superfluid. In general, firm conclusions for cold atomic systems cannot be drawn from hydrodynamic calculations performed under the assumption of incompressibility and uniform equilibrium density. Clearly, a method in which this assumption is removed is needed for studies of the hydrodynamic of these systems.

To accomplish this purpose, we start, in this chapter, with the hydrodynamic equations for a compressible superfluid. Although the effect of compressibility in cold atomic systems has been studied via the Gross-Pitaevskii (GP) equation [51, 52], it is simpler for our purpose of perturbatively studying the compressibility corrections, to start directly with the hydrodynamic limit and the associated coarse grained equations based on conservation of mass and momentum. The hydrodynamic equations we consider can be obtained [51, 52] from the GP equation if a quantum stress term, known [53] to be unimportant in the hydrodynamic regime, is neglected. The procedure we use to solve the hydrodynamic equations is based on an expansion in parameter $(v/v_s)^2$, the square of the Mach number, where v is some characteristic speed of the problem and v_s is the speed of sound. Such expansions have been previously used [54, 55] in other quantum fluids problems. Our expansion procedure leads to linear differential equations, which makes it much easier to find analytic solutions: this is a considerable advantage of our method. At zeroth order in this small parameter one recovers the incompressible results, since v_s is then formally infinite. Our expansion, as it will be seen, is particulary convenient to the study of situations where a flow is imposed on the system by external means. We then proceed to apply this procedure to two specific situations in this category. Although these have been chosen largely because analytic solutions in the incompressible limit can either be easily obtained or already exist, both of these situations have been realized in experiments on cold atomic systems. In the first case, we assume that external constraints confine the superfluid in such a way as to

produce a gaussian profile for the local density of the stationary superfluid, a situation similar to that considered experimentally in Ref. [56] and theoretically in Refs. [50, 57]. The specific force fields required to establish this distribution drop out of the equations: only the resulting density distribution matters. We then, for this example, assume that a flow corresponding to one quantum of axial circulation (i.e. a single vortex) is established in such a way that it is a solution of the zeroth order hydrodynamic equations, and evaluate the first order corrections to the velocity field and to the density due to finite compressibility. In the second problem we consider afresh the obstructed cylinder situation previously studied [31] in the incompressible limit and again evaluate the first order corrections to both components of the velocity field, and to the density, due to the finite compressibility. The geometry considered here is similar to that of recent experiments [43, 44] on Bose-Einstein condensates in a toroidal trap with a repulsive barrier. In both cases we find, as expected, that the corrections are vanishingly small for liquid He. On the other hand, we find that for typical cold atomic systems the corrections due to finite compressibility are often not negligible but that they are sufficiently small to be amenable to our perturbative solution. The observation that corrections due to finite compressibility in cold atomic systems in the hydrodynamic regime are amenable to perturbative solution for the two widely different problems considered here is interesting because it suggests that similar perturbative treatments would be possible for other problems of interest in studies of superfluidity in cold atomic systems .

The rest of this chapter is organized as follows. In section 2.2, we present the details of the perturbative method of calculation used here. The results obtained from application of this method to the problems mentioned above are described in detail in section 2.3. Section 2.4 contains a summary of the main results.

2.2 Methods

As explained above, our objective in this chapter is to study the effect of compressibility on superfluid hydrodynamics in confined geometries, starting with the results for incompressible fluids. The behavior of compressible normal liquids has been studied as early as 1883 [58]. Starting with the general equations governing inviscid fluid flow

-the continuity and Euler equations - we use a perturbative method to study the effect of finite compressibility in the limit where the perturbation parameter, while low, is nonzero. We will see that this is a realistic limit for cold atomic systems of experimental interest. Our perturbative method has similarities to that used in Ref. [59]. That study focuses on the propagation of sound waves, a limit where the perturbation parameter cannot be assumed to be much smaller than unity. The small dimensionless parameter associated with the perturbative expansion is the Mach number, the ratio of the characteristic fluid velocity to the sound speed. For quantum systems, such expansions have been used earlier in Ref. [54, 55] which address a very different problem of the critical speed for the nucleation of vortices in superfluid flow around a disk as compared to our present work on flow patterns for superfluids in confined geometries. The procedure will be illustrated by calculating, for two examples of confined superfluids, the corrections to the velocity field and the density distribution in the low temperature limit where viscosity effects can be neglected.

2.2.1 General

As a simpler alternative to deriving the equations of compressible superfluid hydrodynamics via the GP equation (the model discussed in Chapter5), we start with the fundamental hydrodynamic equations governing fluid flow in the steady state i.e. mass conservation as given by the continuity equation:

$$\nabla \cdot (\rho \vec{v}) = (\nabla \rho) \cdot \vec{v} + \rho(\nabla \cdot \vec{v}) = 0 \tag{2.1}$$

and momentum conservation as given by the Euler equation:

$$(\vec{v} \cdot \nabla)\vec{v} = -\frac{\nabla p}{\rho} + \frac{\vec{f}}{\rho} \tag{2.2}$$

where ρ is the mass density, $\vec{v}$ represents the velocity field, p the pressure, and $\vec{f}$ is the external force per unit volume. The steady state assumption means, as usual, that we are averaging over microscopic scale time fluctuations. Hydrodynamics can also be derived by starting from microscopic or quasi microscopic equations of motion and then coarse graining. When one does that from the GP equations [51, 52, 54, 55] one obtains in the Euler equation an additional quantum stress term. This term need

not be included here for two reasons: first, as explained on page 170 of Ref. [52] (see also Ref. [53]) the order of magnitude of this term (which involves third derivatives of the density) is down by a factor of $(\ell/L)^2$ where ℓ is a microscopic quantum length and L the characteristic length associated with macroscopic pressure variations: it is hence negligible for the hydrodynamic problems considered here. Secondly, this term (involving as it does density derivatives) vanishes at $\kappa = 0$ and, since it appears in the same way as the term $\vec{f}$, it would similarly acquire an explicit factor of κ in Eq. (2.3) below. It is therefore a second or higher order correction in our small parameter. Short range fluctuations may exist, just as they do in classical fluids, but they are averaged over the macroscopic distance L in the hydrodynamic limit. Such a scale clearly exists in experimental Bose systems: the Thomas-Fermi radius of trapped Bose gases can be between two or three orders of magnitude larger than the microscopic coherence length. From experiments on superfluid flow in Bose systems [38, 60, 61] it can be seen that the characteristic Mach number squared, our dimensionless expansion parameter $(v/v_s)^2$, is of order $10^{-2} - 10^{-4}$ and hence small in these systems. The Thomas-Fermi approximation predicts an abrupt drop to zero in the density of the condensate beyond the Thomas-Fermi radius, but this is an artifact of the Thomas-Fermi method: the actual variation in density is smoother. This does not affect the validity of our approach just as the abrupt density drop near a wall does not invalidate classical hydrodynamics given that a large region over which the parameter $(v/v_s)^2$ is small exists.

We consider ρ to be a function of p only (barotropic limit). This limit applies[62] in the very low temperature case that we consider, where the pressure can only be a function of the density. Using the definition of compressibility ($\kappa = \frac{1}{\rho}\frac{\partial \rho}{\partial p}$), Eq.(2.2) becomes:

$$\rho^2 \kappa (\vec{v} \cdot \nabla)\vec{v} = -\nabla \rho + \rho \kappa \vec{f}. \tag{2.3}$$

We now start the perturbative calculation by writing:

$$\rho = \rho_0 + \rho_1 \tag{2.4}$$

$$\vec{v} = \vec{v}_0 + \vec{v}_1 \tag{2.5}$$

where the zero index denotes quantities in the incompressible ($\kappa = 0$) limit and the index one in v_1, ρ_1 denotes the changes in velocity field and density distribution due to the finite compressibility. Substituting Eqs. (2.4) into Eqs (2.1) and (2.2), the Euler

equation at zeroth order takes the form:

$$\nabla\rho_0 = \rho_0\kappa\vec{f} \tag{2.6}$$

which reflects the fact that at $\kappa = 0$ it would take an infinite force to induce a density gradient (here and below, we consider the product κf to be finite, of order unity). For future convenience, let us assume that such a density gradient has somehow been induced by external means. In that case the zero order continuity equation would take the form:

$$(\nabla\rho_0)\cdot\vec{v}_0 + \rho_0(\nabla\cdot\vec{v}_0) \equiv \mathcal{D}^0\vec{v}_0 = 0, \tag{2.7}$$

which reduces to the usual form $\nabla\cdot\vec{v}_0 = 0$ in the absence of external forces. Here we have introduced the operator:

$$\mathcal{D}^0 \equiv \rho_0(\nabla)\cdot + (\nabla\rho_0)\cdot . \tag{2.8}$$

Proceeding now to first order, the corresponding terms in the continuity equation yield:

$$-(\nabla\rho_1)\cdot\vec{v}_0 = \mathcal{D}^0\vec{v}_1 + \rho_1(\nabla\cdot\vec{v}_0) \tag{2.9}$$

while from those in the Euler equation we have:

$$\rho_0^2\kappa(\vec{v}_0\cdot\nabla)\vec{v}_0 = -\nabla\rho_1 + \rho_1\kappa\vec{f}. \tag{2.10}$$

Taking the scalar product of Eq. (2.10) with $\vec{v}_0$ and making use of Eqs. (2.9) and (2.7) one obtains:

$$\mathcal{D}^0\vec{v}_1 = \rho_0^2\kappa\vec{v}_0\cdot(\vec{v}_0\cdot\nabla)\vec{v}_0. \tag{2.11}$$

By this procedure the external force has been eliminated from the equations. The reason this is possible is that the only role of the force is to impose the zeroth order density profile, ρ_0, which alone has physical meaning. Eqns. (2.7), (2.9) and (2.11) are the basic set of equations needed. In general, the best course to obtain the first order results, after getting the zeroth order solution, is to solve first Eq. (2.11) and then obtain the first order density profile from Eq. (2.9).

We now verify the physical meaning of the dimensionless perturbation parameter associated with the low compressibility limit, as discussed above. Dividing through

Eq. (2.10) by ρ_0, introducing the average speed of sound v_s via $\rho_0\kappa = v_s^{-2}$ and introducing the dimensionless variable $\widetilde{\rho} \equiv \rho_1/\rho_0$ (i.e. the dimensionless density correction) we have:

$$-\nabla\widetilde{\rho_1} + \widetilde{\rho_1}\kappa\vec{f} = (\frac{\vec{v}_0}{v_s} \cdot \nabla)\frac{\vec{v}_0}{v_s}, \tag{2.12}$$

where we recall that the product κf must be viewed as finite. We see from this result that the dimensionless perturbation parameter associated with the correction to the density due to compressibility is indeed of order $(v_0/v_s)^2$. Proceeding in a similar way to evaluate the order of magnitude of the correction to the velocity ($\vec{v}_1$) due to the finite compressibility, it can be seen that the dimensionless perturbation parameter associated with the correction to velocity field ($\vec{v}_1$) is $\lambda \equiv (v_0/v_s)^2$.

2.2.2 Zero applied force

As explained above, the equations obtained from the perturbative analysis are quite general and can be used when $\rho_0(r)$ is uniform, as well as when it takes on a specific inhomogeneous form due to the application of some external force $\vec{f}$ which need not be specified. In the case where no external force is imposed on the fluid, the zeroth order density distribution is of course a constant. This applies to the calculations performed in Ref. [31], for an obstructed annular cylinder as explained in the Introduction. In this case it is more convenient to start by simplifying the basic equations from the beginning. Since $\nabla\rho_0 = 0$ and $\nabla \cdot \vec{v}_0 = 0$, one has for the continuity equation at first order:

$$(\nabla\rho_1) \cdot \vec{v}_0 + \rho_0(\nabla \cdot \vec{v}_1) = 0. \tag{2.13}$$

In this limit the first order Euler equation Eq. (2.10) is:

$$-\nabla\rho_1 = \rho_0^2\kappa(\vec{v}_0 \cdot \nabla)\vec{v}_0 \tag{2.14}$$

Combining the two equations above, we obtain the following equation for $\vec{v}_1$:

$$\nabla \cdot \vec{v}_1 = \rho_0\kappa\vec{v}_0 \cdot (\vec{v}_0 \cdot \nabla)\vec{v}_0 \tag{2.15}$$

with the right side known from the solution of the zeroth order equations. Since one of these equations is $\nabla \cdot \vec{v}_0 = 0$, similar Green function methods lead to solutions for both

$\vec{v}_0$ and $\vec{v}_1$. Specializing to the curl free case (absence of vortices) we introduce a scalar potential, $V(\vec{r})$, such that $\vec{v}_1(\vec{r}) = \nabla V(\vec{r})$. Eq. (2.15) then becomes:

$$\nabla^2 V = \rho_0 \kappa \vec{v}_0 \cdot (\vec{v}_0 \cdot \nabla)\vec{v}_0, \tag{2.16}$$

which we solve by finding the appropriate Green function with specified boundary conditions. Once this is done we solve for $\vec{v}_1$ from:

$$V(\vec{r}) = \int d\vec{r}' G(\vec{r}', \vec{r}) \rho_0 \kappa \vec{v}_0 \cdot (\vec{v}_0 \cdot \nabla)\vec{v}_0 \tag{2.17}$$

recalling that $\vec{v}_1 = \nabla V(\vec{r})$.The correction to the density profile due to nonzero compressibility - ρ_1 - is calculated from Eq. (2.14) using the result for $\vec{v}_0$ obtained from solving the equation $\nabla \cdot \vec{v}_0 = 0$.

We conclude this general discussion with a brief discussion of the relation of our method to the Thomas-Fermi approximation. Eqn. (2.6) is an equilibrium relation ($v = 0$) and in that respect it is analogous to neglecting the kinetic terms in the GP equation: in this sense it resembles the Thomas-Fermi approximation in equilibrium. Corrections to the equilibrium Thomas-Fermi approximation have been studied previously. For example, Ref. [63] keeps terms linear in the velocity in the context of studying collective modes. This is different from our current study where, as explained in the Introduction, we consider induced flows.

2.3 Results

In this section we present the results of calculations of the corrections to the velocity field ($\vec{v}_1$) and density (ρ_1) due to finite compressibility using the perturbative method described in the section above. We study the effect of nonzero compressibility on the velocity field and density distribution of confined superfluids in two different situations. In the first case, an external force imposed on the fluid leads to an equilibrium gaussian density profile. The other case, in the $f = 0$ limit, deals with the compressibility corrections for superfluid flow in an obstructed cylinder, as discussed in Ref. [31]. In the case of an obstructed cylinder, the fluid is driven by an obstruction and therefore the Thomas-Fermi approximation is not valid as the kinetic energy term cannot be neglected.

2.3.1 Gaussian density profile

We consider first the case of a cylindrical sample where an external force imposed on the fluid in equilibrium results in a gaussian density profile i.e.

$$\rho_0(r) = \rho_a e^{-(\frac{r}{\sigma})^2} \tag{2.18}$$

where σ is the characteristic length scale associated with the density profile and r the cylindrical radial coordinate. We assume the cylinder is long enough so that we can neglect edge effects and solve the problem as a quasi two-dimensional one. Density profiles other than a gaussian can also be considered by the same method: here we focus on this case as an example. In order to calculate ρ_1 and $\vec{v}_1$ we use equations (2.9) and (2.11) respectively, which requires us to calculate first an appropriate zeroth order velocity field $\vec{v}_0$ corresponding to the incompressible limit.

To calculate $\vec{v}_0$, we use the zeroth order continuity equation (Eq. (2.7)) with the gaussian density profile, ρ_0, specified above. Calculating $\nabla\rho_0$ and defining a velocity potential such that $\vec{v}_0 = \nabla V_0(r)$, Eq. (2.7) takes the form:

$$\nabla^2 V_0 = \frac{2r}{\sigma^2}\frac{\partial V_0}{\partial r}. \tag{2.19}$$

This equation has a variety of solutions reflecting the many possibilities for the velocity field. For our example, we restrict ourselves to begin with to the case where $\vec{v}_0$ has no azimuthal dependence. Assuming then a purely radial solution i.e. $V_0(r,\phi) = F(r)$ we obtain $\mathcal{D}_r^0 F(r) = 0$ where

$$\mathcal{D}_r^0 \equiv r\frac{\partial}{\partial r} + r^2\frac{\partial^2}{\partial r^2} - \frac{r^3}{\sigma^2}\frac{\partial}{\partial r}. \tag{2.20}$$

The solution is:

$$F(r) = C_1 Ei((r/\sigma)^2) \tag{2.21}$$

where Ei is the usual exponential integral function. We obtain from this a purely radial part of v_0 namely:

$$\vec{v}_{0r} = \frac{C_1}{r}e^{(\frac{r}{\sigma})^2}\hat{r} \tag{2.22}$$

where the integration constant C_1 is a quantity with units of circulation. The increase in the velocity with r appears strange until one recalls that the density decreases (see

Eq.(2.18)) exponentially so that the current decreases with r. To this particular solution we add an azimuthal component corresponding to a vortex centered at the origin. This amounts to adding to the velocity potential a term proportional to ϕ, which of course also satisfies the linear Eq. (2.19). This leads to an azimuthal component:

$$\vec{v}_{0\phi} = \frac{C_2}{r}\hat{\phi} \tag{2.23}$$

Introducing this vortex in the fluid implies that the curl of the zeroth order velocity field, $\nabla \times \vec{v}_0 = 2\pi\delta(\vec{r})\hat{z}$ is non-zero. This does not contradict the definition of $\vec{v}_0$ as a gradient of a velocity potential since one is dealing with a singular field. The singularity at the origin requires the imposition of a small r cutoff. At the vortex core radius in a Bose fluid, the characteristic velocity of fluid flow is of the same order of magnitude as the sound velocity [51]. The region near the vortex core is also characterized by faster density variations, making the quantum pressure term important. Therefore, we introduce a short distance cutoff near the vortex of order few times the vortex core radius. Outside this region our assumptions of small Mach number squared and negligible quantum pressure term hold true. The circulation around the origin due to the azimuthal component of the velocity is $2\pi C_2$. Physically, we know that the circulation must be quantized. It follows that, as opposed to C_1, C_2 is not a completely arbitrary constant, but must be an integer number of circulation quanta h/m. To make an estimate of the order of magnitude of the effect of nonzero compressibility, we assume in our numerical work that there is one quantum of circulation.

We now proceed to the first order calculation taking as our zeroth order results the density distribution Eq. (2.18) and the velocity field given by the sum of Eqs. (2.22) and (2.23). In the results presented in this subsection, we measure lengths in units of σ, and choose for our illustrative example $C_1 = C_2$. This choice of C_2 leads to some formal simplifications.

To evaluate the first order corrections, we now turn to Eq. (2.11) in order to solve for the correction to the velocity field ($\vec{v}_1$). We use the Green function method for this purpose. It is not hard to see that the azimuthal part of $\vec{v}_0$ does not contribute to the right side of Eq. (2.11). Hence it is sufficient to find the Green function corresponding to the operator $\mathcal{D}_r^0$ introduced in Eq. (2.20):

$$\mathcal{D}_r^0 G(r, r') = \frac{1}{r}\delta(r - r') \tag{2.24}$$

Solving the second order differential Eq. (2.24), we find this Green function to be:

$$G(r,r') = \frac{Ei(\frac{r_>^2}{\sigma^2})}{2} \tag{2.25}$$

where $r_>$ is the larger one of the two radial coordinates r, r'. Introducing then a velocity potential V_1 such that $\vec{v}_1 = \nabla V_1(r)$, Eq. (2.11) leads us to V_1:

$$V_1 = \int r'dr' G(r,r')[\rho_0^2 \kappa \vec{v}_0 \cdot (\vec{v}_0 \cdot \nabla)\vec{v}_0] \tag{2.26}$$

Evaluating the expression on the right side of Eq.(2.26) with the Green function given above and the zeroth order velocity fields, we obtain analytically the potential associated with the correction to the velocity field ($\vec{v}_1$) due to nonzero compressibility. The quantity $\vec{v}_1$ itself can then be evaluated. As already anticipated in our zeroth order results, the divergence of the azimuthal field at $r = 0$ requires the introduction of a small r cutoff, which we denote as b. It is chosen as discussed above, which also ensures that v_0 does not exceed the critical velocity. The result for $\vec{v}_1$ is found to be:

$$\begin{aligned} \vec{v}_1 = \quad & \rho_a \kappa \frac{e^{s^2}}{r\sigma^2}[\frac{C_1^3}{2}(F_1(s^2,\delta^2)) - \frac{C_1 C_2^2}{2}(F_1(-s^2,-\delta^2) + \\ & 2(Ei(-\delta^2) - Ei(-s^2)))]\widehat{r} \end{aligned} \tag{2.27}$$

where we have introduced the dimensionless length $s \equiv r/\sigma$ and the dimensionless cutoff $\delta \equiv b/\sigma$. We have also introduced the auxiliary function F_1 as:

$$F_1(s^2,\delta^2) = -\frac{e^{\delta^2}}{\delta^2} + \frac{e^{s^2}}{s^2} - Ei(\delta^2) + Ei(s^2). \tag{2.28}$$

Although the zeroth order velocity has both radial and azimuthal components, the correction is purely radial. Nevertheless, the azimuthal component of $\vec{v}_0$ has a large effect on the result via the C_2^2 dependence of the second term in Eq. (2.27). When $C_1 = C_2$ it is possible to further simplify the result. Expressing in that case $\vec{v}_1$ in the natural dimensionless form, that is, in units of $C_1/\sigma \equiv v$ we have:

$$\frac{\vec{v}_1}{v} = \frac{1}{2}(\frac{v}{v_s})^2 \frac{e^{s^2}}{s}(H(\delta) - H(s))\widehat{r}, \tag{2.29}$$

where $v_s^2 \equiv 1/\rho_a\kappa$ and the function $H(\xi)$ is defined as

$$H(\xi) = -\frac{e^{\xi^2}}{\xi^2} - \frac{e^{-\xi^2}}{\xi^2} - Ei(\xi^2) - Ei(-\xi^2). \tag{2.30}$$

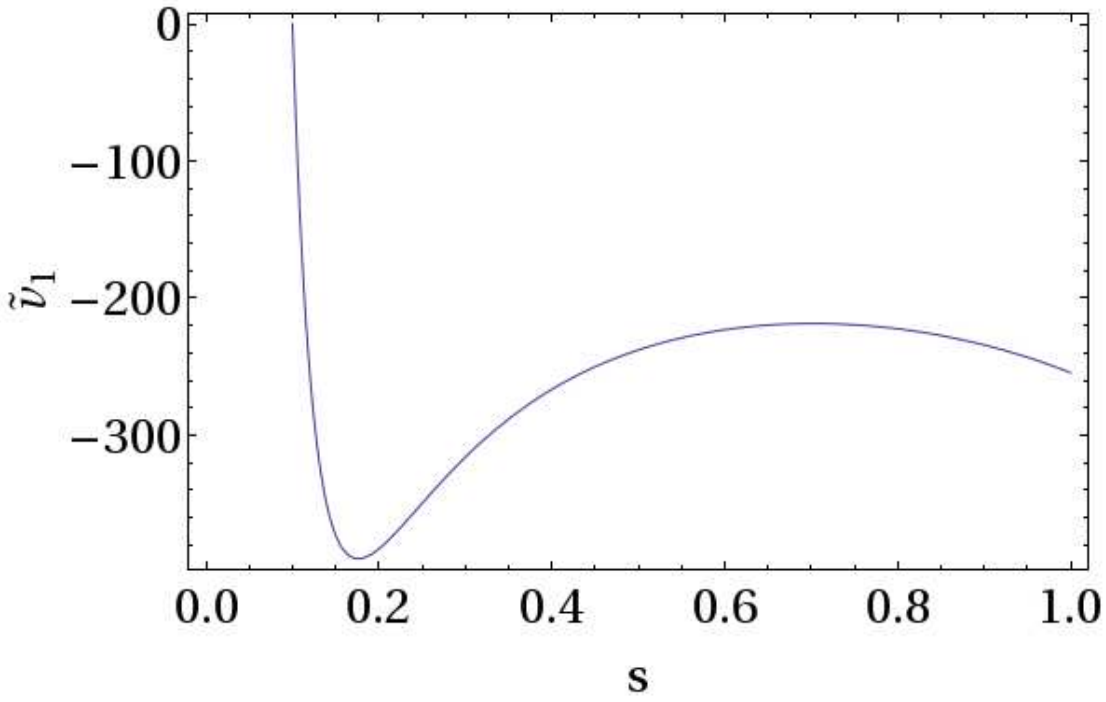

Figure 2.1: The dimensionless first order correction to the velocity field due to finite compressibility, plotted versus s. The quantity plotted, $\widetilde{v}_1$, is defined as $v_1/\lambda v$.

In Eq. (2.29) the dimensionless perturbation parameter λ discussed above can be clearly identified as the prefactor appearing in the right side. Figure 2.1 shows the magnitude of the correction to the velocity, $\vec{v_1}$, in units of λv for the case where $C_1 = C_2$ as in Eq. (2.29). This quantity is plotted as a function of the dimensionless radial coordinate s. The value of the cutoff parameter has been set so that $\delta = 0.1$. The numbers in the vertical scale seem to be large. This can easily be seen (see Eq. (2.29)) to arise from the smallness of our choice for the cutoff parameter δ. We will see that in actual situations, the parameter λ is small enough so that the first order velocity correction is indeed much smaller than the zeroth order velocity scale. A similar remark applies to the density correction discussed below.

We can now study the correction to the density profile (ρ_1) and eventually to the physical current associated with fluid flow. Using Eq. (2.9) we find that a solution with azimuthal symmetry exists and satisfies the first order inhomogeneous differential equation:

$$-\frac{\partial \rho_1}{\partial r}(v_{0r}) = \rho_0 \frac{\partial v_1}{\partial r} + \rho_1(\frac{\partial v_{0r}}{\partial r} + \frac{v_{0r}}{r}) + \frac{\partial \rho_0}{\partial r} v_{1r} \tag{2.31}$$

It is straightforward to solve this differential equation using the method of integrating factors, and we find the correction ρ_1 to the density to be:

$$\frac{\rho_1}{\lambda \rho_a} = \frac{e^{-s^2}}{2}(G_1(\delta) - G_1(s)) \tag{2.32}$$

where the function G_1 is defined as

$$\begin{aligned} G_1(\xi) = \quad & \frac{e^{-\xi^2}}{\xi^2} + \frac{e^{\xi^2}}{\xi^2} - 2\Gamma[0, -\xi^2] - 2\log(\xi^2) \\ & -Ei(\xi^2) + Ei(-\xi^2). \end{aligned} \tag{2.33}$$

Here $\Gamma[a, z]$ represents the incomplete Gamma function. Figure 2.2 shows a plot of the first order correction to the density. The quantity plotted is the left side of Eq. (2.32) as a function of the dimensionless radial coordinate s for the same conditions as in Fig. 2.1.

We can now look at the corresponding current $\vec{j}$ that is a characteristic physical property of the system. The total current is the sum of zeroth and first order terms: $\vec{j}_{total} = \vec{j}_0 + \vec{j}_1$, where $\vec{j}_0 = \rho_0 \vec{v}_0$, and $\vec{j}_1 = \rho_0 \vec{v}_1 + \rho_1 \vec{v}_0$ is the first order correction. In Figure 2.3 we present a vector plot of $\vec{j}_1$. The conditions, units and parameter values are

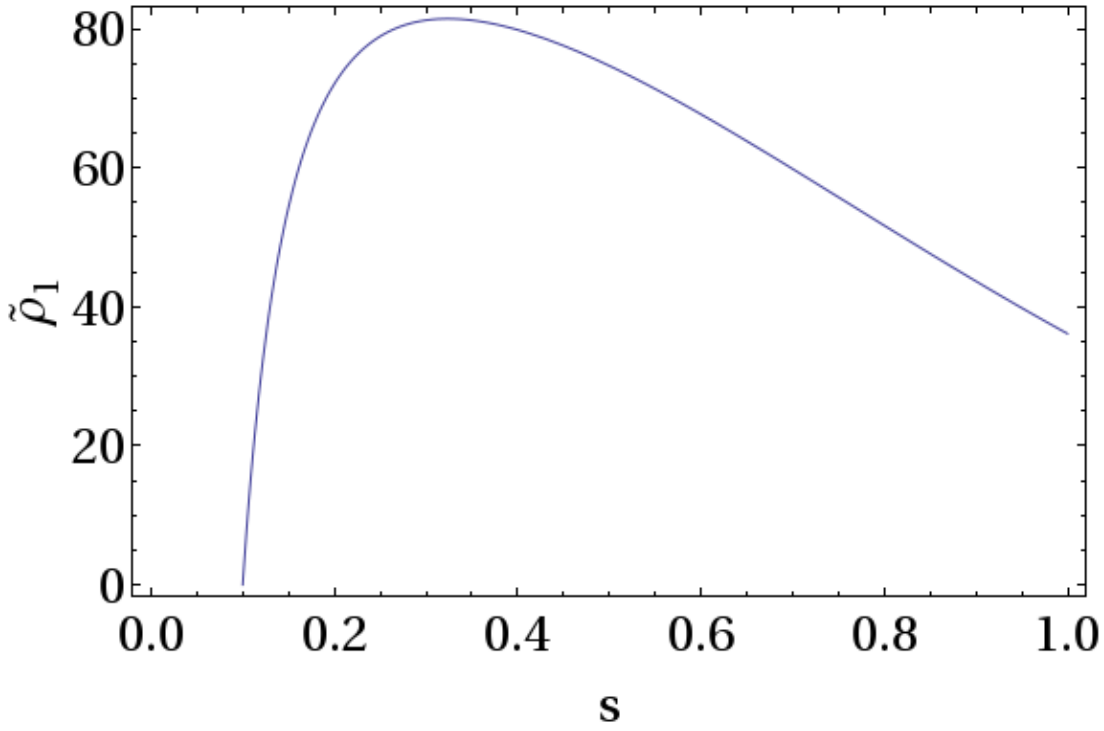

Figure 2.2: Plot of the dimensionless first order correction to the density due to finite compressibility versus s. The quantity plotted, $\widetilde{\rho_1}$, is defined as $\rho_1/\lambda\rho_a$.

as in Figs. 2.1 and 2.2. The calculation described in subsection 2.3.1 is used to obtain $\vec{j}_1$. We see that the magnitude of the physical current arising from finite compressibility is more pronounced closer to the central region of the cylinder.

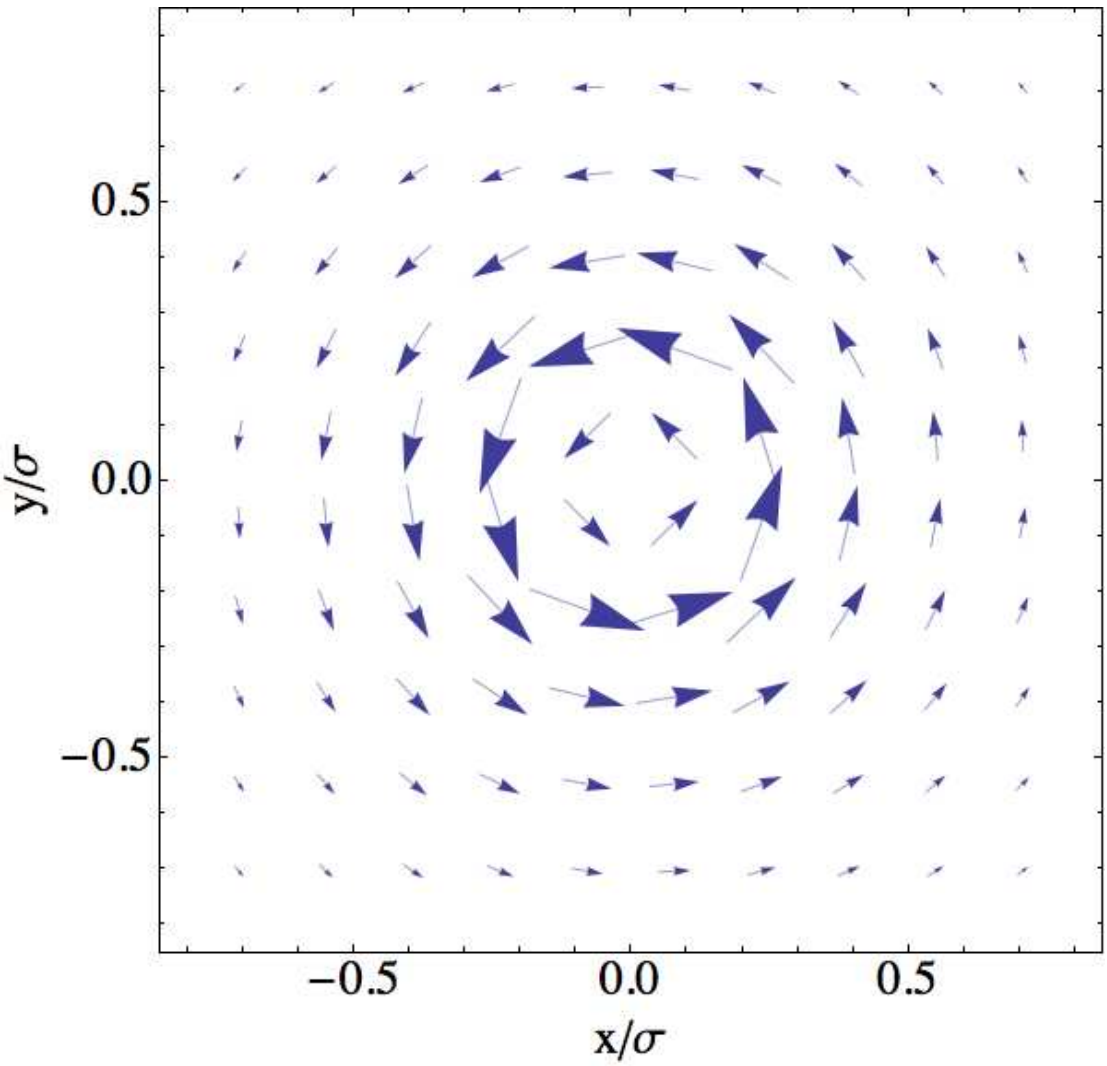

Figure 2.3: Vector plot of the first order correction to the current due to finite compressibility.

To check the validity of the perturbative treatment developed here, it is necessary to examine the order of magnitude of the perturbation parameter λ for typical cold atomic systems. We assume that C_2 corresponds to one quantum of circulation. Thus

we take, as orders of magnitude, $\sigma \approx 10^{-5}m$ [56], $C_2 \approx 10^{-9}m^2/s$ and [38, 60, 61, 64] $v_s \approx 10^{-2}m/s$. This leads to the estimate $\lambda \approx 10^{-4}$. Thus, for cold atomic systems, while λ may be quite small, the corrections are far from negligible since the quantities plotted in Figs. 2.1 and 2.2 can be as large as several hundreds. Thus, corrections up to the level of $\sim 10\%$ can easily arise. Hence, we conclude that compressibility effects in the hydrodynamics of cold atomic systems, as seen from the analytic perturbative method used here, cannot be neglected. For superfluid Helium, however, the circulation quantum is much larger (a factor of 20 compared to Rb), the speed of sound much larger [65] and system sizes also larger: thus a similar estimate yields $\lambda \approx 10^{-14}$ and the corrections are negligible, as expected.

2.3.2 Obstructed Cylinder

We now consider the second problem, which is perhaps of clearer physical relevance: we calculate the compressibility corrections for the obstructed rotating cylinder geometry studied in Ref. [31]. This geometry is that of a circular cylinder of radius a with a thin radial wall extending from the axis to the outer wall of the cylinder. We assume that the cylinder is long enough for end effects to be negligible. We define an angle ϕ from the line of obstruction so that $\phi = 0$ defines the location of the radial wall. In this case there is no applied force in equilibrium: thus when the cylinder does not rotate the density is uniform, at a value which we take as our unit of density. When the cylinder rotates about its axis with angular speed Ω a velocity field is induced in it. In the zero compressibility limit, this velocity field is known [31]. We will calculate here the corrections to the velocity field and the density profile due to non-zero compressibility within the perturbative method described in Sec. 2.2. The field $\vec{v}_0$ for the geometry under consideration was obtained in Ref. [31] via both scalar and vector potential methods. It can be expressed in series form:

$$\begin{aligned} v_{0r}(r,\phi) = \quad & \Omega r \sin(2\phi) \\ & + \frac{16\Omega a}{\pi} \sum_{n \text{ odd}} \left(\frac{r}{a}\right)^{n/2-1} \frac{1}{n^2-16} \cos(n\phi/2) \end{aligned} \tag{2.34}$$

$$\begin{aligned} v_{0\phi}(r,\phi) = \quad & \Omega r \cos(2\phi) \\ & - \frac{16\Omega a}{\pi} \sum_{n \text{ odd}} \left(\frac{r}{a}\right)^{n/2-1} \frac{1}{n^2-16} \sin(n\phi/2). \end{aligned} \tag{2.35}$$

To obtain the correction to the zeroth order velocity field ($\vec{v}_1$) due to finite compressibility we solve Eq. (2.15) by the Green function method. We introduce a scalar velocity potential V_1 so that $\vec{v}_1(\mathbf{r}) = \nabla V_1(\mathbf{r})$, and calculate the Green function associated with the operator ∇^2 (see Eq. (2.16)) for appropriate boundary conditions. We recall [31] that the boundary condition on the total velocity field, $\mathbf{v}(\mathbf{r})_\perp = (\mathbf{\Omega} \times \mathbf{r})_\perp$, where $\mathbf{r}$ is a vector from the center to a point on the boundary, and $\perp$ denotes the component normal to the boundary, is already satisfied by the zeroth order velocity in Eq. (2.34). Hence, $V_1(\mathbf{r})$ satisfies zero Neumann boundary conditions at the cylinder surface. The Green function in this case is then found by standard procedures [66] with the result:

$$G(r,\phi;r',\phi') = -\frac{1}{\pi}\sum_{n=2}^{\infty}\frac{1}{n}r_<^{n/2}\left(\frac{1}{r_>^{n/2}}+\frac{r_>^{n/2}}{a^n}\right)\cos(n\phi/2)\cos(n\phi'/2), \tag{2.36}$$

where $r_>$ ($r_<$) is the larger (smaller) one of the two radial coordinates r and r'. One then gets an expression for the velocity potential in the form of Eq. (2.17), with $G(\vec{r},\vec{r}')$ given by Eq. (2.36) and the $\vec{v}_0.(\vec{v}_0.\nabla)\vec{v}_0$ evaluated from Eqns. (2.34) and (2.35). Taking then the gradient, the correction to the velocity field is calculated. In our subsequent calculations, we introduce a radial cutoff, which we take to be $0.1a$, to exclude the small r region where [31] the zeroth order velocity has a weak square root singularity.

In principle, this procedure involves no advanced mathematical steps. However, one can readily see that it is very lengthy and intricate. Since the right side of Eq. (2.17) is cubic in $\vec{v}_0$, the components of which are in the form of a series, and the Green function Eq. (2.36) involves an additional sum, the expression has the form of a quadruple sum, plus integrals over the angle ϕ' and the radial coordinate r'. This is done analytically: the angular integrals are performed first and lead to Kronecker deltas that reduce the number of sums. The radial integrals are done next and finally, the remaining (convergent) summations are evaluated. The resulting expression, however, is much too involved to be written here, and it would be truly very difficult even to keep track of all the terms without the help of a symbolic package (we have used Mathematica). The results can then be plotted and the plots are much more illuminating than the lengthy expressions.

One can however see from the basic structure of the equations that overall $\vec{v}_1$ is proportional to the basic velocity scale of the system, which is Ωa, times a factor of $\lambda = (\Omega a/v_s)^2$ where $v_s^2 = 1/(\kappa\rho_0)$. It is rather obvious also from the equations that $\vec{v}_1$

has both radial and azimuthal components. Results for these components are shown in the next two figures. There, the dimensionless quantity plotted is a component of v_1, divided by $\lambda\Omega a$. These are shown as functions of angle and dimensionless radial distance r/a.

In Figure 2.4 we present a plot of the radial component (v_{1r}) in the units described above, at several fixed values of the angle ϕ. One can see that the radial correction to the velocity field goes to zero at $r/a = 1$ satisfying the radial boundary condition discussed above. The magnitude of the correction to the radial velocity (v_{1r}) peaks at different values of r/a depending on how far one is from the line of obstruction along the azimuthal direction. At $\phi = \pi/8$, the peak in the magnitude of v_{1r} occurs closer to $r/a = 1$ than at $\phi = \pi/2$ where it occurs closer to the lower cut-off. At $\phi = \pi$, v_{1r} is identically zero owing to the symmetry of the problem over an angle of 2π.

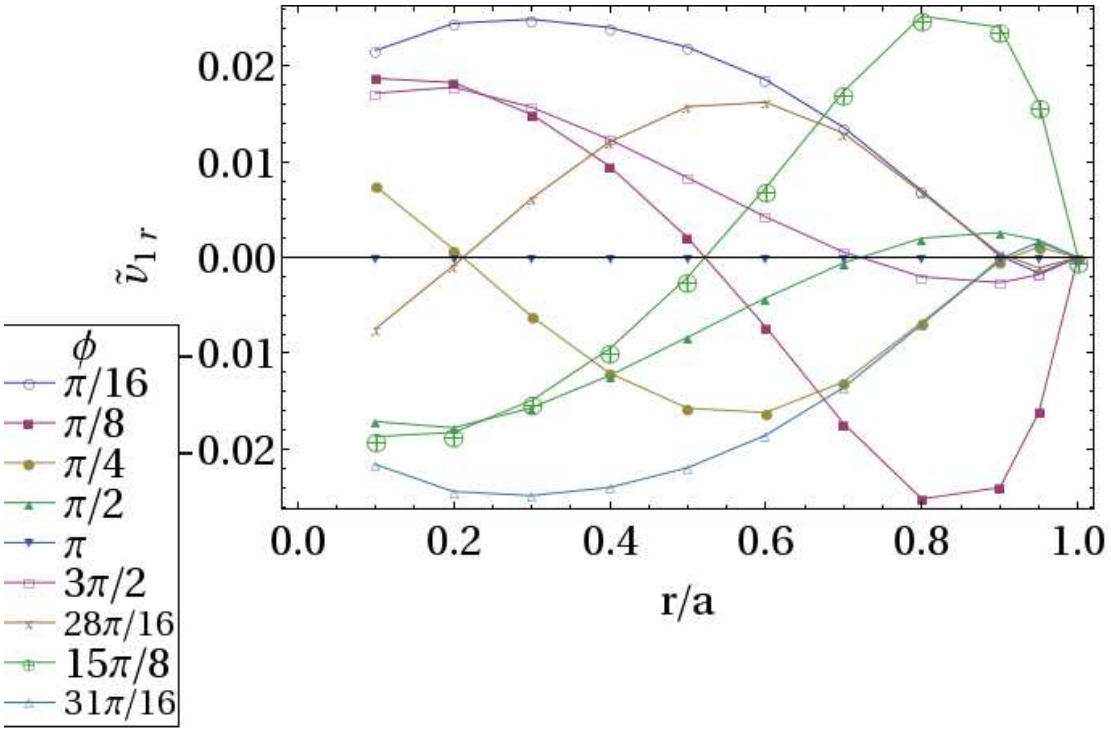

Figure 2.4: Plot of the radial component of the correction to the velocity field $\vec{v}_1$ for an obstructed cylinder. The dimensionless quantity shown is $\widetilde{v}_{1r} \equiv v_{1r}/(\lambda v)$, plotted versus r/a at different angles ϕ.

The corresponding azimuthal component ($v_{1\phi}$) is presented in Figure 2.5. The quantity $v_{1\phi}$ is now plotted in dimensionless units at several values of the dimensionless distance r/a. It can be seen that oscillations, in which one can discern traces corresponding to the $n = 3$ and $n = 5$ terms of the expression for $v_{0\phi}$ in Eq. (2.34), are present in the azimuthal correction to the velocity. This arises from the cubic (in v_0) nature of the perturbation. Again, the boundary conditions at $\phi = 0, 2\pi$ are satisfied with the velocity correction being zero at these values of ϕ.

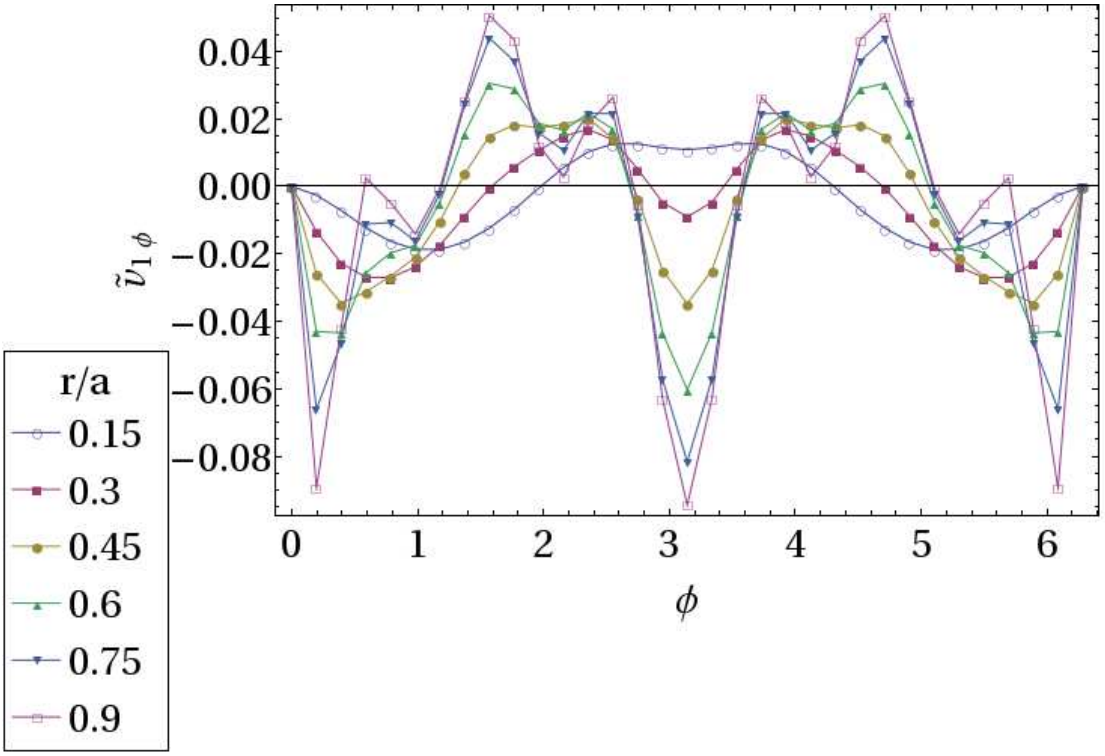

Figure 2.5: Plot of the azimuthal component of the correction to the velocity field $\vec{v}_1$. The dimensionless quantity shown is $\widetilde{v}_{1\phi} \equiv v_{1\phi}/(\lambda v)$, plotted versus ϕ at different values of r/a.

Having calculated the correction to the velocity field due to finite compressibility, we can next study the correction to the density profile (ρ_1). This turns out to be computationally much simpler. Starting with Eq. (2.14), a line integral over $d\vec{r}$ enables us to calculate ρ_1. Since the right side of Eq. (2.14) can be expressed as the gradient of

a scalar quantity, doing an integral over $\vec{r}$,

$$\int \nabla\rho_1 \cdot d\vec{r} = -\int \rho_0^2 \kappa(\vec{v}_0 \cdot \nabla)\vec{v}_0 \cdot d\vec{r} \tag{2.37}$$

enables us to calculate ρ_1 independent of the path chosen within the obstructed cylinder. Using this property of $\nabla\rho_1$, we calculate $\rho_1(r,\phi)$ from a line integral over two different paths and confirm that our result is indeed path independent. We determine the arbitrary constant associated with the integration by enforcing the condition that the total integral of ρ_1 over the relevant region be zero i.e. $\int \rho_1 r dr d\phi = 0$. This condition makes sense physically since the constraint imposed by the container implies that the total mass change due to the compressibility correction must be zero. This gives us the full function $\rho_1(r,\phi)$. Because of the nonlinearities in v_0 present in the equations, the results, although formally analytic in terms of convergent double series, are again quite intricate and will not be written down explicitly here. Instead, as before, results are plotted in the next two figures. The quantity plotted is the dimensionless $(\rho_1/(\rho_0\lambda))$ and we plot it at different values of ϕ in Figure 2.6. One can see that that radial dependence of the density correction is more prominent closer to the line of obstruction within the cylinder, which makes sense physically. Also, it is positive or close to zero near the outer boundary, and negative at smaller values of r/a. This could be a direct consequence of the fact that the higher the velocity of fluid flow, the lower is the condensate density [67]. Similarly, the azimuthal dependence of $\rho_1(r,\phi)$, is plotted at different values of r/a in Figure 2.7. The angular dependence of these results reflects again the nature of the perturbation.

We proceed now to analyze the order of magnitude of these corrections in typical cold atomic systems. For this problem (as opposed to the gaussian profile situation) the values of the dimensionless quantities plotted do not exceed unity, so that the corrections are now smaller and the perturbation theory is valid for larger values of λ. Our results show that compressibility corrections for fixed Ω are smaller for more confined geometries. In this case, it is best to phrase the issue in terms of the validity of the theory (or the need for it) in the upper part of the relevant range of Ω. This range of Ω values is limited by the requirement that the circulation created by the zeroth order velocity does not exceed a flux quantum. The velocities involved are roughly [31] of order $10^{-1}\Omega a$. Demanding then that this speed, times a, be of order of one flux

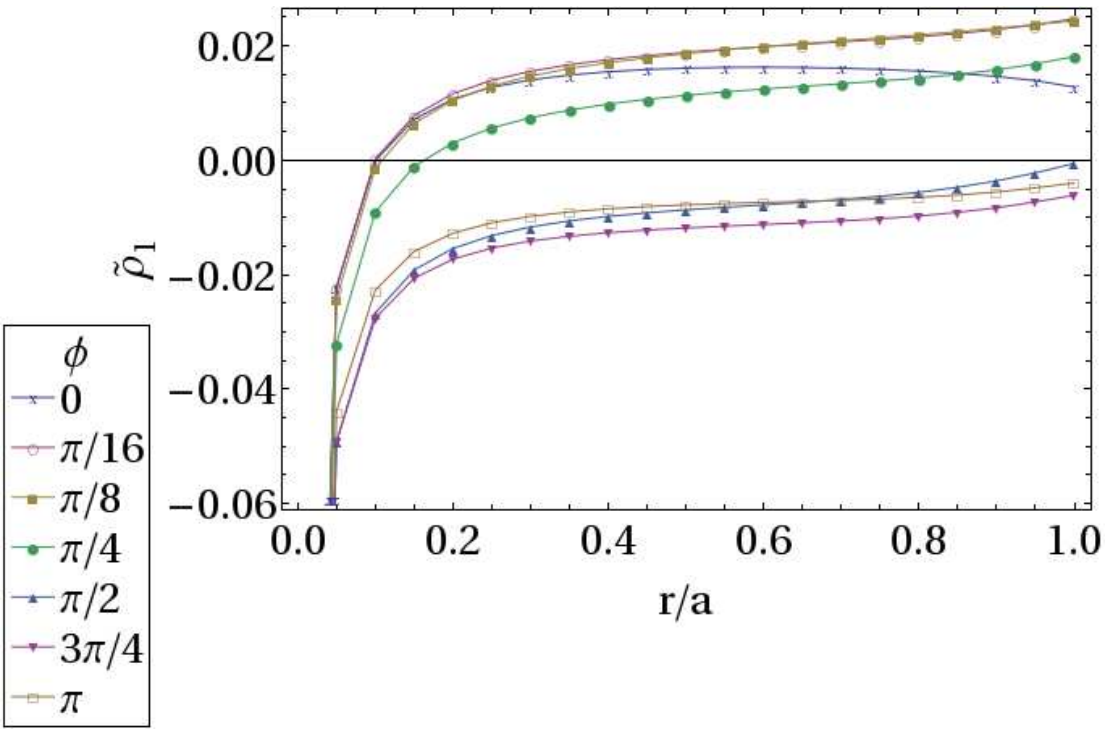

Figure 2.6: Plot of the radial dependence of the dimensionless correction to the density - $\widetilde{\rho}_1 \equiv \rho_1/(\lambda\rho_0)$ - due to finite compressibility at different values of ϕ.

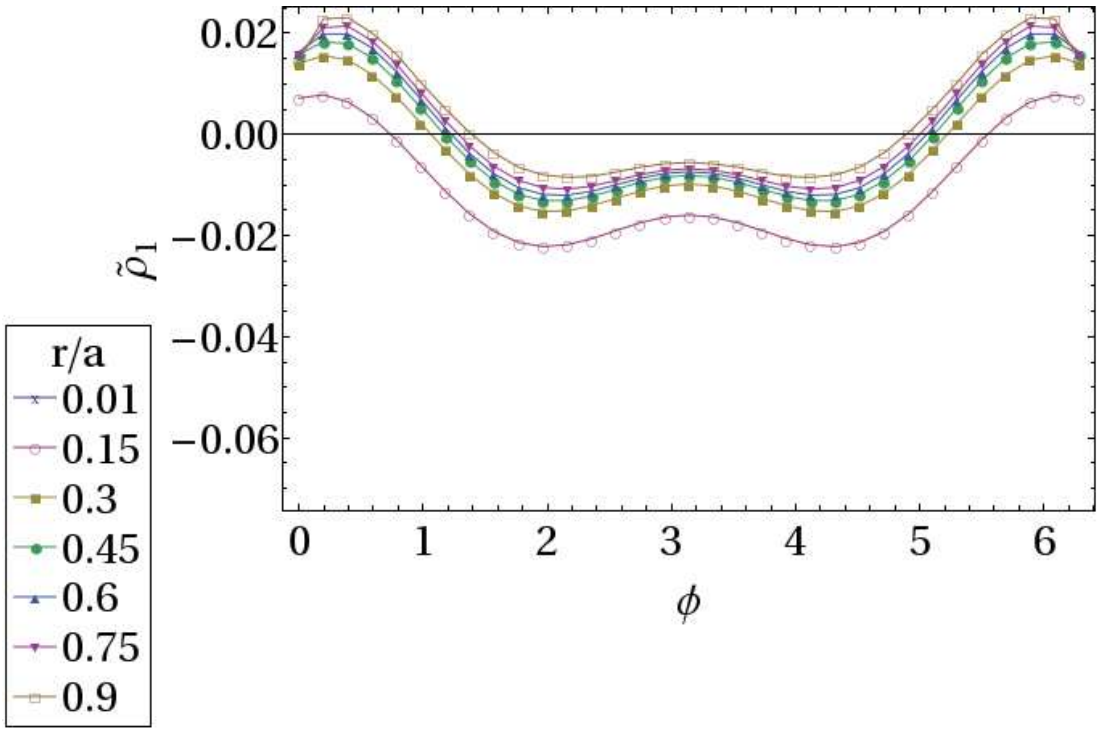

Figure 2.7: Plot of the azimuthal dependence of the dimensionless correction to the density - $\widetilde{\rho}_1 = \rho_1/(\lambda\rho_0)$ - due to finite compressibility at different values of r/a.

quantum and using the order of magnitude values discussed previously, we find that the corresponding λ for cold atomic systems may reach values up to 10^{-2}. Thus, we find that for these systems finite compressibility corrections are not always negligible but on the other hand they are, at least for samples that are not too small, amenable to our perturbation approach. For superfluid helium we find, as expected, that λ is much smaller and the incompressible limit calculations are perfectly adequate.

2.4 Conclusions

In this chapter, we have studied, by means of an analytic method, the hydrodynamics of compressible superfluids in confined geometries as a coarse-grained model for the flow properties of superfluid associated with disorder networks. We have shown that for practical cases of interest in cold atomic systems confined to complex geometries the corrections to the zero compressibility results are not negligible, but they can in many realistic cases be treated in a perturbative manner with the relevant dimensionless parameter being the square of the ratio of the typical speed to the sound speed (the Mach number). This method may be used in very general situations. We have illustrated the procedure by working out two examples. In the first, confining forces that need not be specified constrict the fluid to having a Gaussian density distribution at zeroth order. In the second, we have considered the case of a rotating obstructed cylinder filled with superfluid, with the density being uniform when the cylinder is at rest. The zeroth order (incompressible limit) solution to the problem is available [31] and the perturbative method is used to evaluate the corrections, again essentially in an analytic way. The general usefulness of the method is therefore illustrated by these examples. The general nature of the perturbative method applied to superfluids in confined geometries makes it useful for describing the results of relevant experiments on cold atomic systems, some of which have been mentioned in Section 2.1. One of the main advantages of our procedure is that, since the resulting equations are linear, it is very amenable to analytic solution. We expect that this method will complement numerical calculations based on more microscopic descriptions such as the GP equation studied in Chapter 5. Starting directly from the hydrodynamic equations is, in the appropriate limit, a good alternative to using the full GP equations, for situations where a hydrodynamic scale

flow is imposed on the system.

Compared to the hydrodynamic model presented in this chapter, a less coarse-grained picture of a dislocation network and superfluidity is presented in Chapter 3. A dislocation network and the associated superfluid field is modeled using a coupled field random Ising network.

Chapter 3

Random Network Ising Model with Quenched or Annealed Disorder

3.1 Introduction

Spin models on random networks are relevant to many physical phenomena and therefore have been studied in a variety of contexts. Early studies of phase transitions in spin models on random networks were concerned with the critical behavior of randomly diluted magnetic systems [68, 69]. The system-spanning percolation cluster [70] just above the percolation threshold has a ramified network structure with fractal dimension less than the physical dimension of the system: hence it is necessary to work out the critical behavior of spin models defined on a random network to develop an understanding of phase transitions in dilute magnets near the percolation point. The well-known "node-link-blob" descriptions of percolation clusters [71, 72] were developed to address this problem. Spin models on artificially constructed regular fractal networks were also studied: [73, 74] an advantage of these models is that their equilibrium thermodynamic properties could be calculated exactly for some of the relevant networks. Also, such studies were expected to provide some insight on the behavior of spin systems on real fractal networks.

More recently, there has been an explosion of research activity on random networks that are believed to describe various systems of interest in physics, biology, engineering and social sciences [75, 76, 77, 78, 79]. Some of these studies have concentrated on structural aspects of random networks, [80, 81, 82] while others have investigated the collective behavior of interacting objects residing on different kinds of random networks of interest. Models in which spin variables defined on random networks interact with one another provide examples of systems that exhibit nontrivial collective behavior, such as phase transitions [83]. For this reason, a variety of models with Ising, [84, 85, 86, 87, 88] Potts [89, 90] and[91, 92] XY spins, defined on different kinds of random networks, have been studied in recent years using both analytic and numerical methods. These studies have revealed many interesting features [93] in the equilibrium and dynamic behavior of spin systems on random networks.

Disorder is an essential aspect of spin models defined on random networks. Depending on the network being considered, disorder may appear in different aspects of the spin model, such as in the number of spins interacting with a particular one (the degree of connectivity may be different [94, 95] for different nodes at which the spins are located) and the strength of the interaction between pairs of spins (the interaction strength may be different for spin pairs in the network that are separated by different distances). The disorder in such systems, arising from the randomness in the structure of the network, is generally assumed to be *quenched* in the sense that for any realization of the model the thermodynamic degrees of freedom associated with the network structure are fixed, and therefore the network does not evolve in time. In theoretical treatments of the equilibrium behavior of such spin systems, the free energy is therefore averaged over different realizations of the disorder [35]. However, the validity of the assumption of the disorder being quenched depends crucially on the comparison of relative time scales - real networks do evolve in time and the assumption of quenched disorder would not be valid unless the time scale over which the network changes is orders of magnitude larger than the time scale of the spin fluctuations. If these two time scales are comparable to each other, or at least not too different, then the disorder should be considered to be *annealed* and the partition function of the spin system (not the free energy) should be thermodynamically averaged over different realizations of the disorder in the network, to obtain a correct theoretical description of the equilibrium behavior. Thus, the disorder

in the spin system would change from quenched to annealed if the time scale for the evolution of the network structure decreases from being much longer than that for spin fluctuations to values roughly comparable to, or shorter, than the typical relaxation time of the spin variables. In this chapter, we address, within the context of a simple specific model, the question of how the equilibrium behavior of a disordered spin system (specifically, its behavior near a phase transition) would be affected by such a change in the dynamics of the network on which the spins reside, so that the fluctuations associated with the disorder would have to be properly included in the thermodynamics calculations.

The question of how disorder affects the critical behavior near a phase transition has been extensively studied. Here, we consider spin systems in which the disorder does not introduce frustration as it might arise, for example, from the presence of both ferromagnetic and antiferromagnetic interactions. In such systems, the presence of quenched disorder changes the universality class of the phase transition if the specific heat exponent for the transition in the system without disorder is positive (the Harris criterion [96]). The presence of annealed disorder usually does not change the universality class of the phase transition because one recovers an effective model without disorder after averaging the expression for the partition function over the disorder variables (in some cases, the presence of annealed disorder leads to a "Fisher renormalization" [97] of the critical exponents).

A question that has not received much attention in the recent literature, although touched upon in some older work [98, 99, 100], is how the transition temperature itself, and other thermodynamic quantities, are affected as the nature of the disorder is changed from quenched to annealed, reflecting a difference in the network dynamics. This is one of the main issues addressed in the present study. The answer to this question is not universal - it depends on the specifics of the system being considered. Earlier studies [98, 100] considered disordered spin models in which the distribution of the interaction parameter is narrow, such as magnetic systems with bond dilution in which the interaction parameter can have two values, J and 0, and models in which it has a Gaussian distribution with width much smaller than the average. These studies show that the thermodynamic behavior and the transition temperatures of quenched and annealed systems are similar. In contrast, in the model we consider here the distribution

of the interaction parameter is very broad (log-normal, see below). In such cases the differences between quenched and annealed properties with this kind of disorder have not been previously analyzed in any detail. We give below examples of systems for which this question is relevant – our work was partly motivated by these problems, although it is quite independent of them.

The possibility of supersolid behavior [101] in ^{4}He arising from superfluidity along a random network of dislocation lines has been considered [25, 26, 24, 18, 29, 102] recently. An illustration of dislocation lines forming a random network can be seen in Fig. 1.3. Quantum Monte Carlo simulations [25, 26] have shown that superfluidity can occur near the core of a dislocation line in solid ^{4}He or along grain boundaries [47]. The transition in a model in which superfluidity occurs near dislocation lines has been investigated [24, 18, 29] theoretically, assuming a frozen dislocation network (quenched disorder). However, dislocation line segments do fluctuate in time and it has been suggested [22] that this motion may suppress the local temperature of superfluid ordering. Since the dislocation motion changes the nature of the disorder in the superfluid problem (described by a ferromagnetic XY model) from quenched to annealed, a relevant question is how the nature of the disorder affects the transition temperature. Although the initial experiments [11] on supersolidity are now believed [13] to reflect an elastic anomaly (see next Chapter 4 for more details), the question of how the motion of dislocation line segments affects superfluid ordering is important because of the occurrence of supersolid behavior arising from superfluidity along a network of defects has been established in numerical studies [25, 26, 47]. The effective ferromagnetic interaction between superfluid variables located at nearest-neighbor nodes of a disordered dislocation network falls off exponentially [29] with the length of the network segment that connects the nodes. If the nodes are distributed randomly in space, then this effective interaction would be a random variable with a very broad distribution.

More generally, there are other systems of interest [103, 104, 105, 106] where the effective interaction between neighboring spins is a random variable with a broad distribution. A system of this kind that has received a lot of attention in recent years is dilute magnetic semiconductors [103, 104] in which spins of localized holes interact ferromagnetically via the spins of magnetic impurities present in the system. The quenched disorder here arises from the random locations of the holes, with the interaction strength

falling off exponentially with the distance between two holes. This results in a broad distribution of interaction strength – an essential feature of the model we study here. There is no reliable analytic method for calculating the transition temperature and thermodynamic properties of such quenched systems. A comparison of the properties of quenched and annealed versions of such models would be very useful: analytic calculations of the properties with annealed disorder are possible because they can be mapped exactly [98] to models without disorder. If the properties of quenched and annealed versions of models with a very broad distribution of the interaction strength were similar, (as in [98, 100] the case of a narrow distribution of the interaction strength), then an analytic calculation of the properties of the annealed model would be broadly valid for the physically relevant quenched model. The spin model we study here provides a simple example of disordered systems with a broad distribution of the interaction strength.

In this chapter, we present a study of the thermodynamics of a disordered ferromagnetic spin model defined on a two-dimensional random network, with emphasis on how the thermodynamics, including the transition temperature, is affected by a change in the nature (quenched or annealed) of the disorder. For simplicity, we consider Ising spins (instead of XY spins which would be appropriate for describing superfluid ordering). The network is assumed to have the same connectivity as the square lattice, i.e. every node is connected to four other nodes. Ising spins are defined both at these four-fold coordinated nodes and on the links that connect them. Spins on these one-dimensional links are placed uniformly so that the number of spins on a link is equal to its length measured in units of the spacing between nearest-neighbor sites. Each Ising spin (whatever its coordination number) interacts ferromagnetically with its nearest neighbors. The disorder arises from a distribution of the lengths of the one-dimensional links, i.e. the number of spins in these links. In the dislocation network problem, this distribution may arise from roughening of dislocation line segments [107]. We assume a Gaussian distribution for the number of spins in each link, and study the thermodynamic behavior for different values of the average and standard deviation of this distribution. Since the effective interaction between two spins at nearest-neighbor nodes falls off exponentially with the number of spins in the link that joins these nodes (see below), a Gaussian distribution of the number of spins in a link implies a very broad, log-normal distribution for the effective interaction. The thermodynamic behavior is studied analytically for

annealed randomness and via Monte Carlo simulations for quenched randomness. We find that the transition temperature with quenched disorder is always higher than that in the case of annealed disorder with the same distribution. This difference initially increases with the strength of the disorder, and eventually saturates for larger values of a parameter that characterizes the disorder. For both cases, the specific heat as a function of temperature exhibits two peaks: a sharp one at the phase transition and a rounded peak at a higher temperature, reflecting the one-dimensional fluctuations along the links. The qualitative behavior of the specific heat (and the associated entropy) in both cases is very similar, but there are quantitative differences that become more pronounced as the strength of the disorder increases.

The rest of the chapter is organized as follows. In section 3.2, we describe in more detail the model under study and describe the methods we follow both for analytic calculations and simulations. The results obtained from the study of this model and its relevance to the problems mentioned above are described in detail in section 3.3. Section 3.4 contains a summary of the main results and concluding remarks.

3.2 Model and methods

To study the situations described in Section 3.1, we consider a system of two coupled Ising models. It consists of a system of four-fold coordinated Ising spins (a two-dimensional system) connected by one-dimensional chains of two-fold coordinated Ising spins. In the chains, each spin interacts with its two nearest neighbors, while spins at the nodal sites (crossing points of the chains) interact with their four nearest neighbors. The scheme is illustrated in Fig. 3.1. In this figure, the nodal spins, indicated by red color, interact with their four nearest neighbors, which belong to four different chains, while the spins along the one dimensional chains, indicated by blue color, interact with their two nearest neighbors. In this simple network model, a distribution in the number of 1D spins in the chains leads to randomness in the effective interaction between 2D spins.

We will denote the two dimensional spins as S_i where i is a two dimensional index running from 1 to N^2 where N is a very large number. The number, n_{ij}, of spins in the chain connecting sites i and j dictates the effective "distance" between nodal spins.

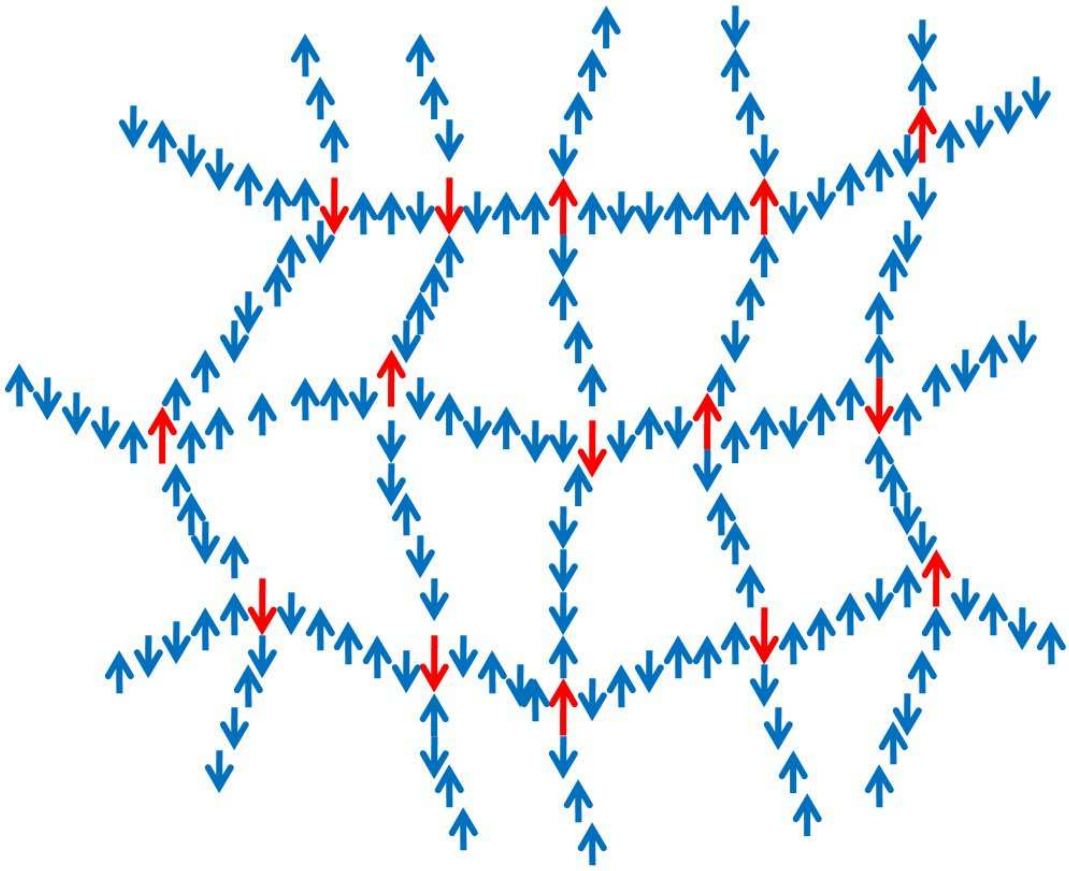

Figure 3.1: Sketch of part of the coupled Ising system under study. The (red) arrows at the nodes are four-fold coordinated Ising spins. They are connected by chains of Ising spins (blue). The chains have variable lengths.

Selecting the set n_{ij} randomly according to some probability distribution (see below) leads to the realization of a random network of coupled spins. The model Hamiltonian can then be written as:

$$H = -J\sum_{i=1}^{N^2}\sum_{\alpha=1}^{4} S_i\sigma_\alpha - J\sum_{<ij>}\sum_{\alpha=1}^{n_{ij}-1}\sigma_\alpha\sigma_{\alpha+1} \tag{3.1}$$

where $S_i = \pm 1$ and $\sigma_\alpha = \pm 1$ are the 2D and 1D spins respectively. The σ_α in the first term on the right are those connected directly to S_i, and the first summation in the last term denotes the sum over all chains, connecting neighboring sites i and j. The quantity J is the exchange energy, which we will set to unity in most of the calculations below. The above formula assumes all $n_{ij} > 1$. When one of the $n_{ij} = 0$ the corresponding S_i and S_j are connected directly. If all $n_{ij} = 0$ we recover the standard 2D Ising model result with a transition temperature of $T_c/J = 2.26$ (we set $k_B = 1$ throughout the chapter). When one of the $n_{ij} = 1$ Eq. (3.1) must be modified so that the term corresponding to the chain connecting S_i and S_j is omitted.

The limit in which all chains are of equal length, $n_{ij} \equiv n$, can easily be considered analytically. To do so, we first calculate the partition function for a finite 1D chain. Starting with the Hamiltonian

$$H_{1D} = -J\sum_{\alpha=1}^{n-1}\sigma_\alpha\sigma_{\alpha+1}, \tag{3.2}$$

it is easily shown from elementary transfer matrix methods that the entire system can be mapped onto an ordinary square lattice Ising model, with an effective interaction, $J^{(n)}$, between two four-fold coordinated spins, separated by a "distance" of n spins, given by:

$$\tanh(\frac{J^{(n)}}{T}) = \tanh^{n+1}(\frac{J}{T}). \tag{3.3}$$

The free energy for the coupled Ising model at fixed n can then be calculated based on the standard Onsager result, plus an additional contribution from the chains of 1D spins linking the nodal 2D spins. Setting henceforth $J = 1$, the contribution to the free energy from the chains can easily be shown to be (for one chain):

$$F_{1D} = -Tn\log(2) - T(n+1)\log(\cosh(\frac{1}{T})) + T\log(\cosh(\frac{J^{(n)}}{T})) \tag{3.4}$$

and the contribution from the 2D spins is:

$$F_{2D} = -T\log(2\cosh(\frac{2J^{(n)}}{T})) - \frac{T}{2\pi}\int_0^\pi \log(\frac{1}{2}(1+\sqrt{1-P^2\sin^2\phi}))\mathrm{d}\phi \tag{3.5}$$

where P is defined as:

$$P \equiv \frac{2\sinh(\frac{2J^{(n)}}{T})}{\cosh^2(\frac{2J^{(n)}}{T})}. \tag{3.6}$$

All thermodynamic quantities can then be calculated from the free energy. We will be interested in the behavior of thermodynamic quantities such as the specific heat and the entropy (S) since they are important in understanding how the behavior of the system near a phase transition is affected by changes in the dynamics of the network. Other thermodynamic quantities such as the spontaneous magnetization and the magnetic susceptibility can also be studied, but we will focus in this work on the entropy and its derivatives.

In general, we are interested in the case where the n_{ij} vary from chain to chain. Accordingly, we generate a random Ising network by choosing n_{ij} for each chain from a gaussian probability distribution:

$$P(n_{ij}) = \frac{e^{\frac{-(n_{ij}-\widetilde{n})^2}{2\delta^2}}}{\sqrt{(}2\pi)\delta} \tag{3.7}$$

where $\widetilde{n}$ is the average of n_{ij} (average number of 1D spins in a chain) and δ the standard deviation of the gaussian distribution.

Using this probability distribution, we will investigate, as explained in the Introduction, how the thermodynamic behavior is affected by quenched and annealed disorder in the network. In the quenched case, the value of n_{ij} in each individual 1D chain is fixed but it varies from one chain to the next according to the gaussian random distribution. This serves as a proxy for a disordered network in which the characteristic time scale for changes in the network is much longer than the characteristic time scale for spin fluctuations. For the annealed case, the values of n_{ij} are allowed to thermally fluctuate and this scenario serves as a proxy for a dynamic network whereby the two characteristic time scales mentioned above are comparable to each other. In studying the differences between quenched and annealed disorder, we will focus on features of the heat capacity such as how the temperatures at which C_v has peaks (corresponding to

2D and 1D behavior, see below) change between the two scenarios. Changes in the peak temperatures depending on the type of disorder will allow us to address the question of the role that the dynamics of the network plays in the ordering of the spins.

When one treats the disorder as annealed, the free energy of our system is:

$$F_a = -T \log\langle Z \rangle, \tag{3.8}$$

where the angular brackets denote an average over the gaussian probability distribution, Eq. (3.7). Therefore, $\langle Z(n_{ij})\rangle$ needs to be calculated. For a gaussian distribution, this calculation can be done analytically. By tracing over the 1D spins in the chains, the model becomes one in which the 2D spins occupying the nodes interact according to $J^{(n)}$ given in Eq. (3.3). Evaluating then the average of the partition function over the gaussian distribution, the annealed Ising model is mapped onto an effective ferromagnetic square lattice Ising model with equal interactions $J_a^{(\widetilde{n},\delta)}$, given by:

$$\tanh(\frac{J_a^{(\widetilde{n},\delta)}}{T}) = \frac{\langle \sinh(\frac{J^{(n)}}{T})\rangle}{\langle \cosh(\frac{J^{(n)}}{T})\rangle}, \tag{3.9}$$

where the average over the discrete gaussian probability distribution indicated by the angular brackets can be easily performed. Thus, the effective interaction for the annealed model is simply a function of $\widetilde{n}$ and δ. The annealed free energy can then be calculated based on a procedure similar to the case where n is fixed in each link (no disorder) as presented in Eqs. (3.4-3.5).

For a system with quenched disorder, the randomness is frozen in each realization of the network. We generate realizations of the network whereby the couplings $J^{(n_{ij})}$, satisfying Eq. (3.3), vary from node to node according to the probability distribution in Eq. (3.7) for n_{ij}. This corresponds to a model on a regular lattice with a random distribution of couplings $J^{(n_{ij})}$. The free energy in the quenched case takes the form:

$$F_q = -T\langle \log Z \rangle, \tag{3.10}$$

where the angular brackets still represent an average over the distribution of chain lengths. Since such a calculation is analytically intractable, we use Monte Carlo (MC) simulations to study the thermodynamic behavior of the model with quenched disorder. A standard MC procedure with Metropolis algorithm is used in our study. In each run

in the simulation, the heat capacity of the spin system can be obtained either from the fluctuations of the internal energy or by taking the derivative of $\bar{E}$, (the overbar denote MC averaging) the average energy per spin, with respect to the temperature. By subsequently averaging the heat capacity over a sufficiently large number of realizations of the chain length configurations (over twelve realizations in this study) of n_{ij}, we obtain the heat capacity for the random Ising model with frozen disorder. Each of the 12 realizations is characterized by a unique random set of the effective interaction ($J^{(n)}$) between 2D spins.

For the study of any random network, it is important to be able to tune the level of disorder. For the current model, the randomness of the network can be controlled by adjusting the values of $\widetilde{n}$ and δ, with the limit $\delta \to 0$ recovering the fixed n coupled Ising model discussed above. Since the number of 1D spins in the chains cannot be negative, we use values of δ and $\widetilde{n}$ such that $\delta/\widetilde{n} \leq 0.5$. With this choice, there is only a very small probability of obtaining negative values for n_{ij}. In such rare cases, in the MC simulation, we set the number of 1D spins in those chains to be two.

The quantity $\delta/\widetilde{n}$ can be used as a measure of the amount of disorder present in the network. A convenient and more physical alternative way to characterize the disorder in this random coupled field model, is via the standard deviation of $J^{(n)}$. Thus, we define a parameter

$$k_\delta = \frac{\sqrt{\langle [J^{(n)}]^2 \rangle - \langle J^{(n)} \rangle^2}}{\langle J^{(n)} \rangle}. \tag{3.11}$$

The quantity k_δ (which depends also on $\widetilde{n}$) quantifies the level of disorder in the random Ising model in terms of the spread in the effective interaction between 2D spins. The differences between the properties of quenched and annealed networks can be analyzed in terms of either $\delta/\widetilde{n}$ or k_δ with a wide range of values considered for both $\widetilde{n}$ and δ.

3.3 Results

In this section we present the results of our study on the random Ising model. We start by briefly discussing the fixed n model ($\delta = 0$, i.e. no disorder) and then proceed to the random model with $\delta \neq 0$. For the random model, we analyze differences between quenched and annealed disorder for both components of the coupled field - 1D and 2D - by studying the behavior of the heat capacity and entropy. For the numerical

(quenched) results, we have simulated samples with the number of 2D spins ($N \times N$) from 16×16 to 30×30, with periodic boundary conditions. Even though the values of N used in our simulation are relatively small, the total number of spins, including the 1D ones is much larger: for e.g. a sample network with $N = 20$ and $\widetilde{n} = 19$ the number of spins is approximately $N \times N + 2 \times N \times N \times \widetilde{n} = 15600$. Finite size effects in the numerical simulation are also analyzed in order to estimate the error margin associated with our results. These are indicated by error bars where warranted.

3.3.1 No Disorder

For fixed n, the energy and heat capacity can be calculated analytically starting from the free energy expressions in the previous Section, Eqs. (3.4)-(3.5). Typical results for the temperature dependence of the energy and heat capacity per spin are plotted in Fig. 3.2. Since, when considering the disordered ($\delta > 0$) case below we will have to take recourse, in part, to numerical methods, we have also computed the same quantities numerically, to test the same numerical procedures that will be employed later. These results are also plotted in Fig. 3.2. As mentioned above, the units of temperature throughout this discussion are such that $J = 1$. The numerical results shown there are based on obtaining the average $\bar{E}$ over a sufficiently large number of MC steps per spin: typically about 16,000 turn out to be needed, and then numerically taking the derivative of this average with respect to temperature to obtain the heat capacity. Despite the modest size of N chosen for this display, it is clear that the numerical results agree sufficiently well with the analytic results, thereby validating our numerical procedures.

In the heat capacity, features associated with both 2D and 1D spin fields can be seen - the sharp peak in C_v at $T \approx 0.5$ is associated with the 2D spin field (and the peak position will be henceforth referred to as T_c^{2D}) while the broad feature in the heat capacity above $T \approx 0.6$ is associated with the 1D spin field. The heat capacity eventually approaches zero at higher temperatures.

For this $\delta = 0$ case, we should recover the standard 2D Ising model results with an effective interaction $J^{(n)}$ and this provides an additional check. Thus, in Fig. 3.3, we plot T_c^{2D} vs n based on both the analytic calculation (that is, on the Onsager result for $J^{(n)}$) and the numerical simulation. Again, the numerical results agree with theory and the continous curve is scaling result from Eq. (3.12). At $n = 0$ we recover the

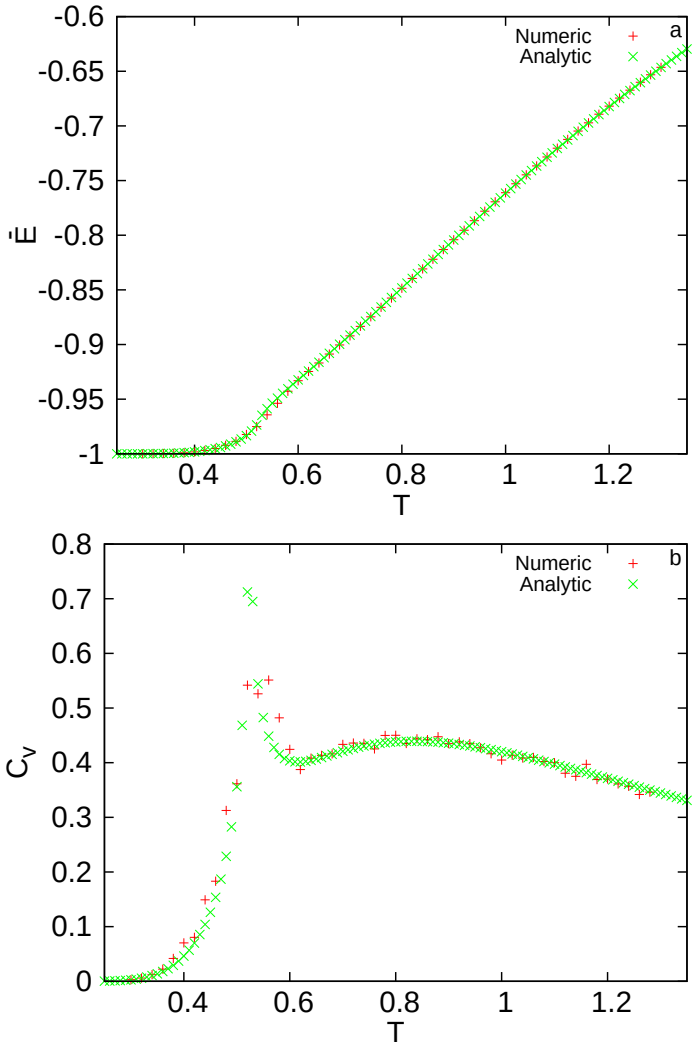

Figure 3.2: Comparison of analytic and MC results. (a) Plot of the average energy per spin $\bar{E}$ vs temperature, for fixed chain length. The numerical results are for $N = 16$ and $n = 19$. (b) Plot of the corresponding heat capacity per spin vs temperature. The parameters are the same as in part (a).

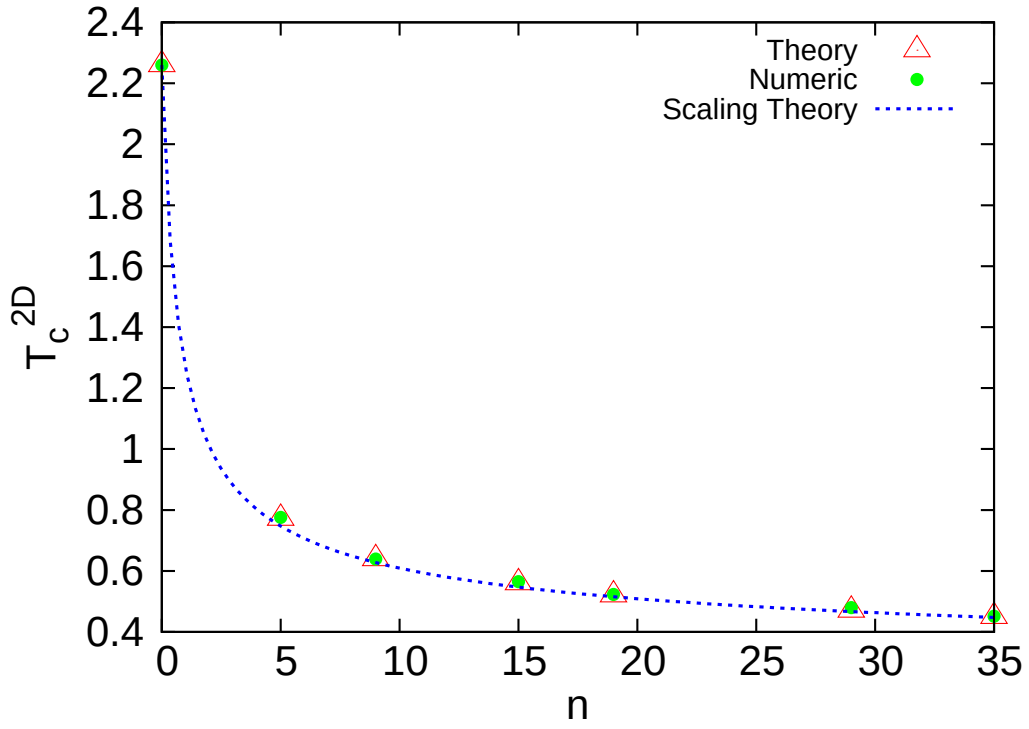

Figure 3.3: Plot of T_c^{2D} vs. number of spins (n) for the fixed n model ($\delta = 0$). The symbols represent, as indicated, analytic results from Onsager's formula and numerical results. Numerical results are for $N \times N = 20 \times 20$. The continous curve is the scaling result.

well known 2D Ising model transition temperature value, as expected. As n increases, T_c^{2D} decreases indicating that ordering occurs at lower temperatures as the effective coupling between 2D spins decreases or, viewing it in a different way, as the 1D part of the coupled fields becomes more prominent. The relation between T_c^{2D} and n can also be obtained (as an alternative to the $J^{(n)}$ calculation) via a simple scaling argument: the ratio of $n+1$ (the number of 1D links between the nodal spins in the network) to the 1D Ising correlation length - $\exp(\frac{2}{T})$ (at $T << 1$)- should remain a constant for all n at the 2D critical temperature. From this scaling argument, we obtain the following relation:

$$T_c^{2D}(n) = \frac{T_c^{2D}(n=0)}{1 + 0.5 T_c^{2D}(n=0)\log(n+1)}, \tag{3.12}$$

where $T_c^{2D}(n=0)$ is the 2D transition temperature at $n=0$. This result is plotted as the continuous curve in Fig. 3.3.

While comparing the analytic results (which are in the thermodynamic limit) to the numerical ones, for T_c^{2D}, as in Fig. 3.3, finite size corrections are inevitably present. It is shown in Ref. [97] that for a 2D Ising model, the difference in T_c between a finite size system (T_c for a finite system is defined to be the temperature at which the heat capacity peaks) and one in the thermodynamic limit is always positive and given by:

$$\frac{T_c(N) - T_c(\infty)}{T_c(\infty)} = \frac{a}{N} \tag{3.13}$$

where $a = 0.3603$, $T_c(N)$ and $T_c(\infty)$ are the critical temperatures for an $N \times N$ 2D Ising model and in the thermodynamic limit respectively. For the random coupled field model, the result above is modified due to the presence of n 1D spins. The modification to Eq. (3.13) due to n can be calculated by rewriting the equation above in terms of the network model with effective interaction given in Eq. (3.3):

$$\frac{J^{(n)}(\infty)/T - J^{(n)}(N)/T}{J^{(n)}(N)/T} = \frac{a}{N}, \tag{3.14}$$

where $J^{(n)}(N)$ denotes $J^{(n)}(T_c(N,n))$, with $T_c(N,n)$ being the 2D transition temperature for an $N \times N$ system with n spins in each link. It then follows that:

$$\frac{T_c(N,n) - T_c(n)}{T_c(n)} = \frac{a[1 - \tanh^2(J^{(n)}/T_c(n))]J^{(n)} \tanh(1/T_c(n))}{Nn \tanh(J^{(n)}/T_c(n))[1 - \tanh^2(1/T_c(n))]} \tag{3.15}$$

where $T_c(n) \equiv T_c(\infty, n)$ and $J^{(n)} \equiv J^{(n)}(\infty)$ are the 2D transition temperature and effective interaction in the thermodynamic limit. The n dependence in the equation above also enters through the effective interaction $J^{(n)}$. The finite size corrections to T_c^{2D} obtained for our numerical model agree well with the prediction in Eq. (3.15) above.

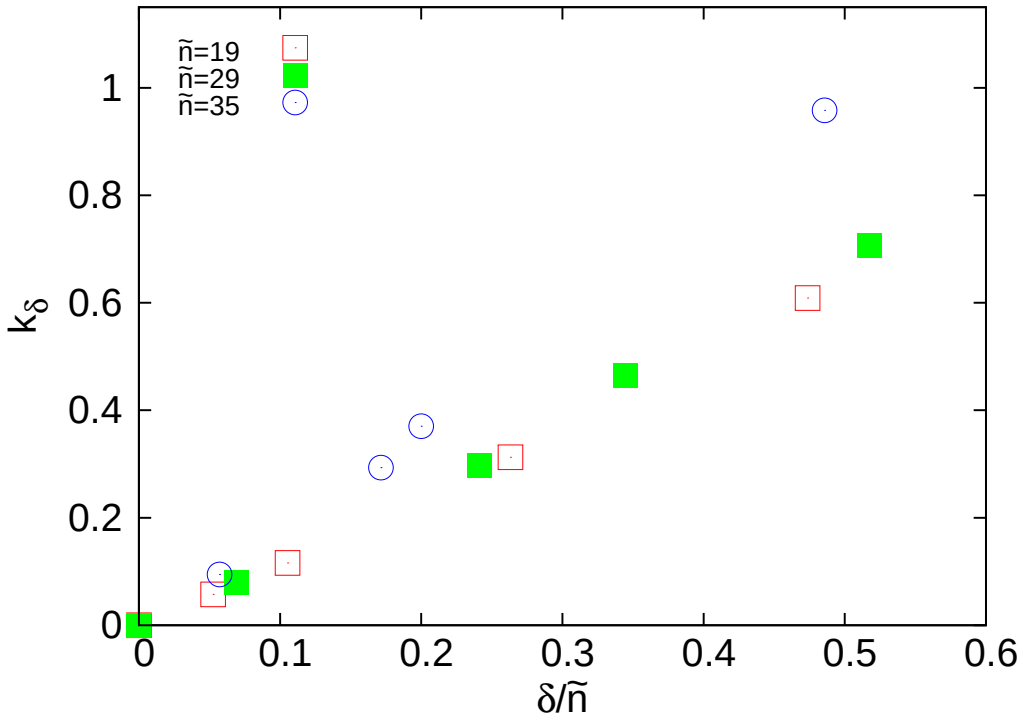

Figure 3.4: Plot of k_δ vs $\delta/\widetilde{n}$ for three different values of $\widetilde{n}$.

3.3.2 Disorder

After having validated our procedures through the fixed n version of our model, we now turn to the random coupled field case. We tune the level of disorder in the random network by adjusting the values $\widetilde{n}$ and δ of the gaussian distribution, Eq. (3.7). Larger values of δ imply a broader gaussian distribution. As mentioned above, a useful approach to characterize the level of disorder in terms of the effective interaction between 2D spins is the parameter k_δ as defined in Eq. (3.11). Since the effective interaction between the 2D spins depends on n_{ij}, randomness in n_{ij} is reflected on $J^{(n)}$ as well. In Fig. 3.4, we present a plot of k_δ vs $\delta/\widetilde{n}$. The parameter k_δ(see Eq. (3.11)) which is simply the

standard deviation of the effective interaction between 2D spins, increases with $\delta/\widetilde{n}$ as would be expected, and it is roughly proportional to it. Note that k_δ is also temperature dependent. This dependence is weak: in Fig. 3.4 we have set the temperature to the average annealed value of T_c^{2D} for each $\widetilde{n}$.

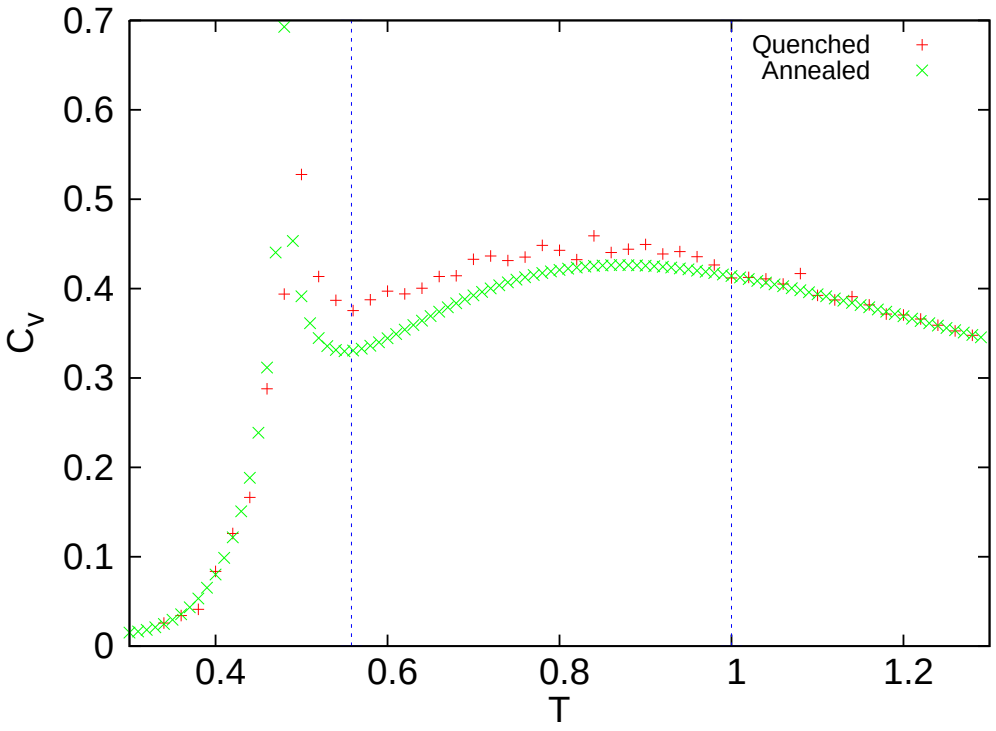

Figure 3.5: Plot of heat capacity vs temperature for $\widetilde{n} = 29$ and $\delta = 7$. Dashed lines indicate T_1 and T_2. T_1 is the lower temperature limit and T_2 the upper temperature limit.

Results for 1D fluctuations

In quantifying differences between quenched and annealed disorder we first look at the 1D field. In each case, we calculate the entropy associated with the 1D fluctuations (S^{1D}) from:

$$S^{1D} = \int_{T_1}^{T_2} \frac{C_v}{T} \mathrm{d}T \tag{3.16}$$

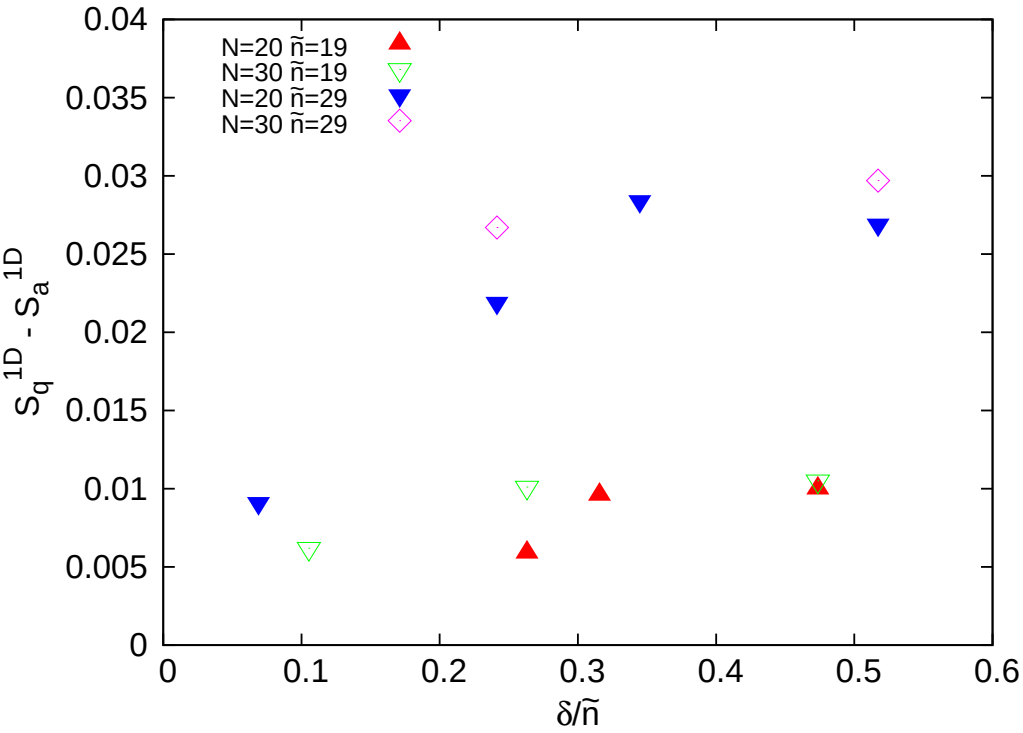

Figure 3.6: Plot of the difference between quenched and annealed entropy associated with 1D fluctuations vs $\delta/\widetilde{n}$.

where the temperature limits T_1 and T_2 are set, in order to take into account the 1D contribution to the total heat capacity, as follows: the lower limit T_1(in Eq. (3.16)) is that of the minimum occurring between the sharp 2D peak and the broad 1D peak (see Fig. 3.5), while the upper limit T_2 is taken to be sufficiently high so that there is no longer any difference between the quenched and annealed specific heats (one may therefore think of T_2 as being infinite). In Fig. 3.6, we plot this difference in the entropies for the quenched and annealed systems, associated with 1D fluctuations, for several values of N, $\widetilde{n}$ and δ as calculated from Eq. (3.16). The weak dependence on N is due to finite size effects in the numerical calculation for quenched disorder. The variation with $\delta/\widetilde{n}$ illustrates the actual dependence of this difference on the disorder. We observe that the quenched entropy S_q^{1D} is always greater than, S_a^{1D}, the annealed entropy.As the level of disorder in the 1D chains in the network increases, the entropy difference between the quenched and annealed cases increases and then saturates at $\delta/\widetilde{n} \approx 0.25$.

The heat capacity due to the 1D chains alone (in the absence of any 2D spins) can be calculated analytically for both quenched and annealed disorder from Eq. (3.4) and the rest of the discussion in Sec. 3.2. The temperature dependence of this 1D heat capacity, evaluated for both types of disorder, is shown in Fig. 3.7. For the example plotted there we see that beginning at $T \approx 0.6$, the quenched disorder heat capacity takes on a higher value than the annealed disorder heat capacity. This mostly accounts for the difference in the 1D contribution to the entropy of the coupled system, as evaluated above from Eq. (3.16) and plotted in Fig. 3.6.

Results for 2D fluctuations

We concentrate here on the differences between quenched and annealed heat capacity due to 2D fluctuations. Since the chain contribution to the heat capacity can be calculated analytically for both quenched and annealed disorder (see discussion in connection with Fig. 3.7), we isolate the 2D contribution to the specific heat by subtracting the chain contribution from the total heat capacity. The total C_v is evaluated analytically in the annealed case and numerically for quenched disorder. The heat capacity due to 2D fluctuations, as obtained in this manner, is shown in the two panels of Fig. 3.8, which correspond to two different sets of values of $\widetilde{n}$ and δ. We see that the results

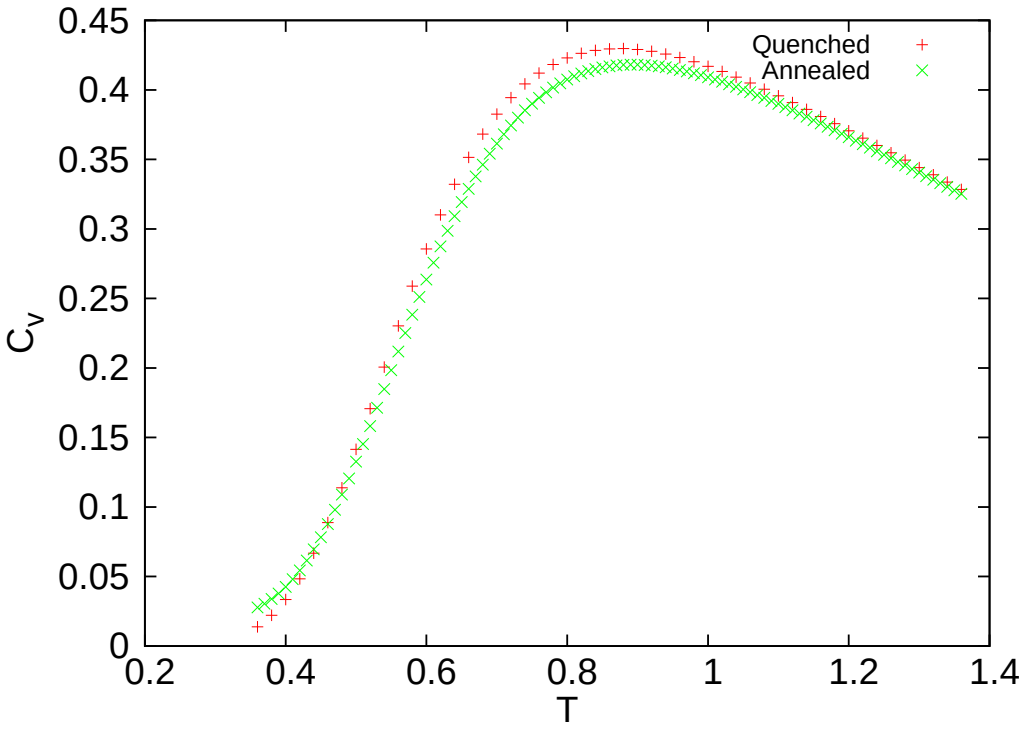

Figure 3.7: Plot of the contribution of the chains to the heat capacity (see text) for quenched and annealed disorder vs. temperature. The average number of spins in the 1D chains, $\widetilde{n}$, equals 19 and $\delta = 9$.

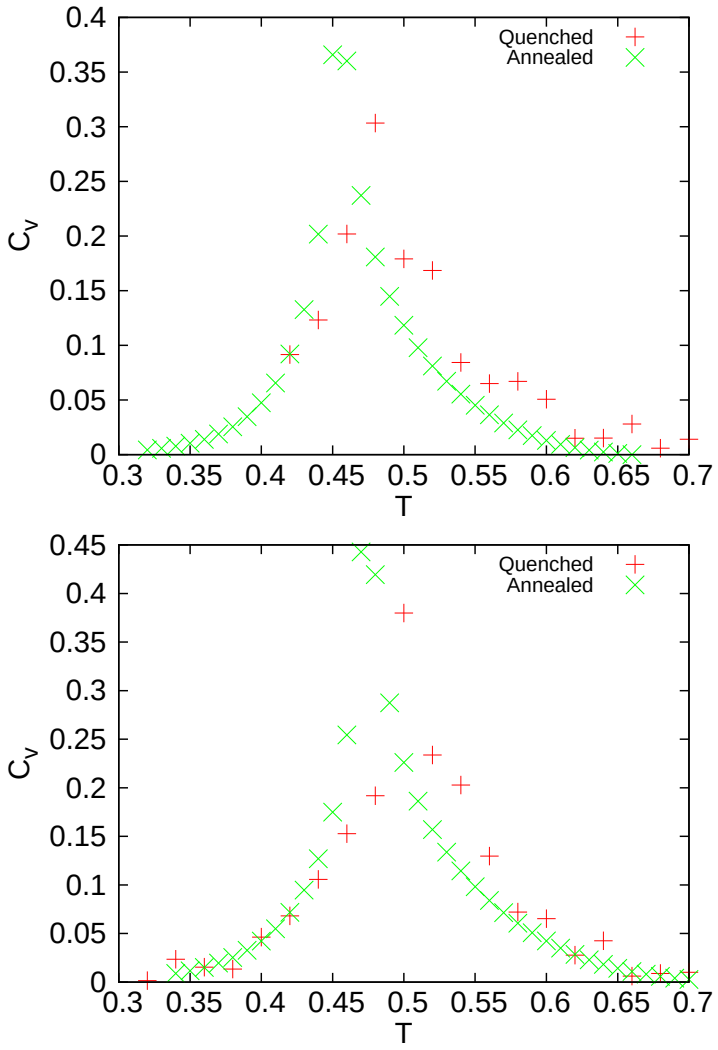

Figure 3.8: The contribution to the heat capacity from 2D fluctuations (see text), plotted vs temperature for both annealed and quenched disorder. The peak in the heat capacity occurs at $T = T_c^{2D}$. In the top panel $\widetilde{n} = 35$ and $\delta = 2$ and in the bottom panel $\widetilde{n} = 29$ and $\delta = 2$.

differ for quenched and annealed disorder. An important feature of this difference is that the 2D transition temperature (T_c^{2D}) for a frozen (quenched) random network is always higher than that obtained for the annealed network. In the context of our random network of Ising spins, these results imply that magnetic ordering always takes place at higher temperatures for frozen disorder than if the disorder is allowed to anneal. In other words, as the time scale associated with the dynamics of the network on which Ising spins reside changes from being much larger than the time scale of spin fluctuations (quenched disorder) to a scenario whereby the two time scales are comparable (annealed disorder), the phase transition of the spin system is suppressed. In terms of the dislocation network problem described in the Introduction, our results based on a simplified Ising model suggest that as the dynamics of the dislocation network become important (i.e. when motion of dislocation line segments takes place over time scales comparable to those of fluctuations in the superfluid field), the associated phase transition (in this case superfluid ordering) would be suppressed. Even though superfluid ordering is described by the ferromagnetic XY model, the simplified Ising model we have considered captures the underlying physical principle: the additional fluctuations present in the annealed case will lower the transition temperature.

In Fig. 3.9, we plot the difference in T_c^{2D} between networks with quenched and annealed disorder. The error bars arise solely from numerical uncertainties in the (quenched disorder) numerical results: for each point in Fig. (3.9), the quenched 2D transition temperature, $T_{c,q}^{2D}$, was obtained by averaging over twelve realizations of n_{ij} in the 1D chains in the network. The error bar associated with each data point is the standard deviation of the difference in T_c^{2D}. It turns out to be more illuminating to plot the results for this difference in terms of the parameter k_δ (see Eq. (3.11)) which characterizes the width of the distribution of effective couplings, rather than in terms of the gaussian width, δ, and average $\widetilde{n}$, of the distribution of n_{ij}. At $k_\delta \to 0$ we recover the ordered results: the difference would be zero in the thermodynamic limit and the small nonzero results arise from finite size effects in the numerical calculation: they are described by Eq. (3.15). The uncertainties due to finite size effects at higher values of k_δ remain the same as in the $\delta \to 0$ limit. Earlier studies [98, 99, 100] on the difference between annealed and quenched disorder, consider the case where the distribution of

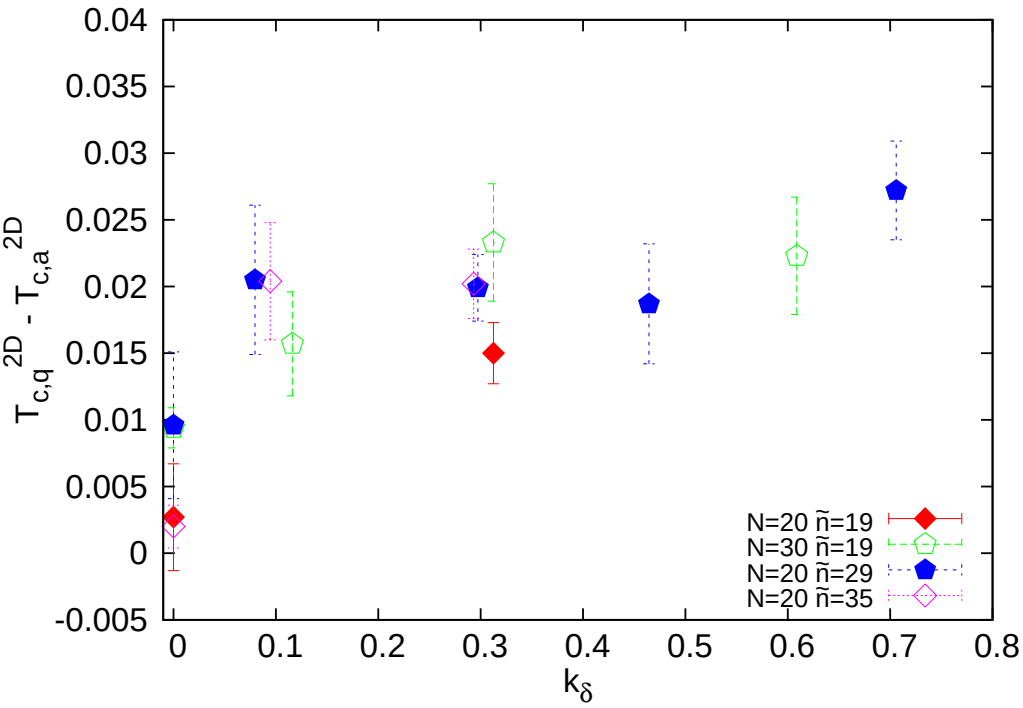

Figure 3.9: Plot of the difference between the 2D transition temperature (taken to be the temperature at the 2D peak of the specific heat) for quenched disorder, $T_{c,q}^{2D}$, and the corresponding value for annealed disorder, $T_{c,a}^{2D}$. This difference is plotted vs the parameter k_δ. The error bars denote numerical uncertainty. The difference between the 2D peak temperatures was studied for $\widetilde{n} = 19, 29$ and 35 with a range of values of δ setting the range for k_δ. Numerical results for the quenched case are labelled by the size of the lattice (N) used in the simulation.

spin interaction strengths is narrow, and speculate (without any explicit quenched results) that the difference between transition temperatures is small in that limit. Unlike these earlier studies, our model takes into account a broad distribution of effective interaction strengths and we obtain explicitly transition temperatures for both quenched and annealed models. Our results, as seen in the region where $k_\delta \to 0$ (corresponding to a narrow distribution of interaction strengths) of Fig. (3.9), show that difference in transition temperature is small in this limit. However, we find that as the level of disorder increases, i.e. for higher values of k_δ, the difference in T_c^{2D} between the quenched and annealed networks increases rapidly, until it saturates at $k_\delta \approx 0.1$. Beyond this value of k_δ all the points, regardless of the varying values of $\widetilde{n}$ and δ which were used in the calculation, lie within a narrow band of values. Thus, it seems indeed that k_δ is sufficient to characterize the phenomena associated with 2D fluctuations, rather than $\widetilde{n}$ and δ separately. Interpreting this result in the physical context of a network of dislocation lines, an increase in k_δ reflects an increase in the randomness of a network of dislocation lines due to increasing fluctuation in dislocation line lengths making up the network. Our results suggest that, as the randomness in the network increases, the role of the difference in network dynamics (quenched vs annealed) becomes more important.

3.4 Conclusions

In this chapter, we have studied the role that the type of disorder - quenched or annealed - plays in the thermodynamic behavior of an Ising model defined on a random network. This network consists of four-fold coordinated Ising spins connected by spin chains. The strength of the disorder can be tuned by varying the average value of the chain length and its standard deviation. We have emphasized both the transition temperature and the specific heat in the region dominated by one dimensional fluctuations. We have shown that the transition temperature for our Ising model on a random network in which the disorder is quenched (frozen) is always higher than the transition temperature for annealed disorder with the same distribution. The magnitude of the difference between the two transition temperatures is quantified by our study. We also show that the entropy associated with the one dimensional fluctuations is larger for the quenched case.

Our study quantifies the difference between the properties of quenched and annealed versions of disordered systems. The quenched assumption applies when the time scale over which the disorder changes is much longer than that for the spin fluctuations. In our model the strength of the effective interaction between neighboring sites has a very broad distribution. Its general interest is that it relates to a variety of experimentally studied systems in which the strength of the effective interaction between neighboring spins has a very broad distribution. An example is dilute magnetic semiconductors. Our results indicate that the transition temperature and other thermodynamic properties of dilute magnetic semiconductors might be approximated from an analytic calculation for the annealed model with the same distribution of interaction strengths. Our model may be relevant also to the renewed interest on dislocation networks in solid ^{4}He. It presents a simplified version of how the dynamics of a dislocation network may influence a superfluid field in its vicinity. Our results indicate that in the annealed scenario, when fluctuations of dislocation line segments within a network become important i.e. when the time scale for dislocation line fluctuations becomes comparable to or smaller than the time scale associated with fluctuations of the superfluid field, the associated phase transition is suppressed. On the other hand, superfluid ordering would be enhanced in the vicinity of a dislocation if the dislocation network can be considered to be frozen. While our results have been obtained for a simplified Ising version of the superfluid transition, we expect that the general conclusion about the transition being suppressed by fluctuations in the dislocation network will remain valid when the proper symmetry of the superfluid order parameter (XY model) is taken into account. Quantum effects, considered in Ref. [22], but not taken into account in this chapter, are expected to enhance the suppression of the superfluid transition due to the motion of dislocation lines. In Chapter 5, however, a quantum model for the interplay between dislocation line and superfluidity is considered. The effect of dislocation motion on superfluidity is studied at the microscopic level.

Prior to studying a quantum model, in Chapter 4, we focus on the elastic properties of crystal ^{4}He and explore the influence of the superfluid field on the motion of a dislocation line within the crystal.

Chapter 4

Dislocation Mobility and Anomalous Shear Modulus Effect in ^{4}He Crystals

4.1 Introduction

Solid ^{4}He is the archetype of a quantum crystal. Quantum effects in solid ^{4}He were pointed out as early as 1960s [108, 33], and extensive work on this and many other aspects of its properties [109] has been subsequently performed. Among the quantum mechanical effects it exhibits are those associated with crystalline defects some of which were discussed in Section 1.3.1 earlier. More recently, the observation of a marked period drop with temperature in torsional oscillator experiments [11, 110] in solid ^{4}He, originally interpreted as evidence for a "supersolid" state, renewed both theoretical and experimental interest on topics related to quantum crystals. Subsequently, solid ^{4}He was also shown to undergo an anomalous softening of the shear modulus [111, 112]. This drop in the shear modulus was observed at the same temperature range as the drop in period seen in torsional oscillator experiments. As noted in Section 1.2 of Chapter 1, these results suggest that the anomalous shear modulus effect, rather than the change in the inertial mass dragged by the oscillator, was responsible for the observed drop in torsional oscillator period [13, 14]. Nevertheless, the discovery of anomalous shear

modulus softening has led to new and important questions being posed on the elastic properties of solid ^{4}He and in particular on the role of dislocation lines in this material. Given that the mechanical properties of crystals are largely dictated by dislocation lines, the observed anomalous shear modulus behavior can provide important insights into the elastic properties of quantum crystals.

Indeed, as to the question of what is responsible for the anomalous shear modulus behavior in solid ^{4}He, and the role that quantum phenomena may play in it, a definitive answer is still lacking. One interpretation is that dislocation lines are pinned by ^{3}He impurities at low temperatures but become mobile (able to glide) at higher temperatures when impurities are no longer able to pin the dislocation network [111]. Other proposals [14, 113, 114] model dislocation lines as vibrating strings unable to execute free glide motion. String-like bowing of such dislocation lines in response to stress is taken into account in explaining the shear modulus behavior. Yet another proposal [115, 116] attempts to model the shear modulus behavior by taking into account the interactions between dislocation lines as well as the Peierls barrier contribution to the damping of the dislocation motion. Here, we propose that a superfluid field associated with the dislocation line cores may play an important role in pinning the dislocation motion and therefore affect the shear modulus behavior. Besides calculating the contribution to dislocation motion damping arising from the superfluid field surrounding a dislocation line, we will also address how our results are consistent with the experimental results on the temperature dependence of the shear modulus.

The role that a putative quantum field associated with the dislocation line could play in the anomalous shear modulus behavior has been recently explored in the literature [117]. At low temperatures we expect quantum effects other than impurity pinning and thermal phonon scattering to be important in terms of damping of dislocation line motion and the associated anomalous shear modulus behavior, particularly in the absence of ^{3}He impurities: experimental studies of ultra pure solid ^{4}He samples with negligible concentration of ^{3}He impurities also exhibit anomalous shear modulus behavior [118, 119]. Even for ^{4}He crystals essentially free of any ^{3}He impurities and characterized by distances between impurity atoms larger than the cell size in which ^{4}He is contained, anomalous shear softening is observed [21]. These experimental observations

inevitably point out, as noted in Ref. [119], that dislocation pinning by impurities cannot be the only mechanism responsible for anomalous shear modulus behavior. High quality ^{4}He crystals presumably with low dislocation density and low impurity concentration, also exhibit anomalous shear modulus behavior [122]. Therefore, we consider it pertinent to study the effect of superfluid field on dislocation motion within crystalline ^{4}He. Assuming a coupling [29] (see theoretical background in Section 1.4) between the dislocation line strain and the superfluid field, it is possible either that the superfluid field makes it easier for the dislocation line to move or that it contributes to the pinning of the dislocation line thereby making it harder for it to move. The study presented in Chapter 3 investigating the effect of dislocation network dynamics on the superfluid field showed that a quenched dislocation network enhances superfluidity near it while dynamic networks suppress superfluidity [120].

In this chapter, our main objective is to show that one can understand the the sharp decrease of the shear modulus with temperature observed in experimental studies [114, 121, 122] via the existence of a superfluid field associated with the dislocation lines. This requires as a preliminary step to study the effect of superfluid field on dislocation motion, i.e. to investigate the damping of dislocation line motion. To do so, we calculate the mobility of a gliding dislocation line, which in a conventional crystal corresponds to an inverse viscosity, in a quantum crystal. Our calculation of the dislocation motion mobility is performed by extending a method developed in earlier work on quasicrystals [32]. We extend this method to quantum crystals utilizing a hydrodynamic approach: the hydrodynamic equations for ^{4}He crystals as developed in Refs. [33, 34]. Based on earlier studies [123, 124] on the role that dislocation lines play in determining the elastic properties of solid ^{4}He crystal, we relate the dislocation mobility to the shear modulus of the crystal. We will then model existing shear modulus experimental data [114, 121, 122], and show that the drop in shear modulus with increasing temperature is consistent with the existence of an underlying rapid increase of the superfluid order parameter as the temperature decreases. Based on our model, we find that the damping of dislocation motion due to superfluid field is more important, in the low temperature limit, than that arising from other sources of damping such as ^{3}He impurities and thermal phonon scattering. The experiments [114, 121, 122] on the shear modulus behavior of solid ^{4}He use a procedure where a shear strain is applied on the crystal at

a set frequency, ω. At the lower frequencies utilized in experimental studies (as low as 2 Hz for the applied strain), the experiments are best analyzed, in agreement with the arguments presented in Ref. [125], in the limit, where the inertial mass of the dislocation line can be ignored and one can, moreover, focus on the quasi-static limit [126] for the strain due to dislocation motion. At higher frequencies the possibility arises of a phase shift between the applied strain and the resultant displacement of the dislocation line. Although for the purposes of our study, we focus mainly on understanding the mechanism behind the sharp drop in shear modulus as a function of temperature for a gliding dislocation line, we note that our model is amenable also to a higher frequency scenario where the dislocation executes some combination of gliding and string-like vibration, out of phase with the applied strain. Our procedure enables us, by making use of our results on dislocation pinning due to the superfluid field present within crystal ^{4}He, to model the low frequency shear modulus temperature behavior seen [111, 112, 127, 114] in strain experiments as well as that [114, 127] of the Q factor at higher frequencies.

The organization of the rest of the chapter is as follows. In section 4.2 we present the hydrodynamic method used to calculate the mobility of a dislocation in a quantum solid, and show how the mobility can be related to the shear modulus. In section 4.3 we illustrate how our results can be used to model the experimental data on shear modulus softening in response to increasing temperature. Two figures illustrate the comparison between theory and experiment: very satisfactory agreement is found. Finally, section 4.4 contains a summary of the main results and concluding remarks.

4.2 Methods

4.2.1 Dislocation Mobility

We begin here by describing the method we use to calculate the dislocation mobility in a quantum crystal. This is based on an extension of the procedure [32] previously employed to compute the dislocation mobility in quasicrystals, combined with the usual hydrodynamic equations [33, 34] for quantum crystals.

Consider an edge dislocation with Burgers vector of length b in a crystal subjected to a shear stress σ. The shear stress will result in a force per unit length on the dislocation line, $\vec{F}_D$, which will cause the dislocation line to move. The velocity($\vec{V}_D$) of

the dislocation line [32] is then proportional to $\vec{F}_D$:

$$\vec{V}_D = M\vec{F}_D \tag{4.1}$$

where M is, by definition, the mobility coefficient and, for simplicity, we consider the vectors $\vec{F}_D$ and $\vec{V}_D$ to be parallel to each other. The general approach seen in [32] and [128] to the calculation of the mobility involves equating the rate of work done by a force applied on the dislocation line, which causes the line to move with a constant speed V_D, to the energy dissipation rate due to the fields associated with the dislocation line motion. Thus, one has,

$$F_D V_D = -\frac{d}{dt}\int d^2 r E_{el}, \tag{4.2}$$

where the right hand side is the rate at which energy is dissipated in the elastic fields, as mentioned above, and the integral is over a two dimensional plane orthogonal to a straight edge dislocation. The left hand side is the rate at which energy is transferred onto the dislocation line due to the applied force F_D.

To calculate the mobility, one isolates the terms in the right side of Eq. (4.2) that are proportional to V_D^2. Then one extracts M from the relation:

$$F_D V_D = M^{-1} V_D^2, \tag{4.3}$$

where we have made use of Eq. (4.1). The left side of Eq. (4.3) is evaluated from the right side of Eq. (4.2) using hydrodynamic methods described below. Then, the constant of proportionality between the dissipation and the square of V_D is the inverse mobility of the dislocation line.

The contribution to the mobility of the dislocation line that we wish to calculate arises from physical phenomena at length scales much larger than the dislocation core size. Hence, as in Ref. [32], we can use hydrodynamic methods, which are valid at such length scales. The proper hydrodynamic approach in our case is as developed in Refs. [33, 34]. We particularly follow the notation of the latter.

We have for elastic energy density E_{el} and its differential, dE_{el}, the expressions:

$$\begin{aligned} dE_{el} &= Tds + \lambda_{ik} dw_{ik} + \phi d\rho + \vec{v}_n . d\vec{g} + \vec{j}_s . d\vec{v}_s, \\ E_{el} &= -P + Ts + \lambda_{ik} w_{ik} + \phi\rho + \vec{v}_n . \vec{g} + \vec{j}_s . \vec{v}_s, \end{aligned} \tag{4.4}$$

with the associated Gibbs-Duhem equation:

$$0 = -dP + sdT + w_{ik}d\lambda_{ik} + \rho d\phi + \vec{g}.d\vec{v}_n + \vec{v}_s.d\vec{j}_s. \tag{4.5}$$

In these expressions, T is the temperature, s is the entropy density, P the pressure, λ_{ik} the elastic tensor density, ϕ the chemical potential, ρ the mass density, $\vec{v}_n$ the normal fluid velocity, $\vec{g}$ the momentum density, $\vec{j}_s$ is the superfluid momentum density, and w_{ik} is the strain tensor defined as,

$$w_{ik} = \partial_i u_k, \tag{4.6}$$

associated with the lattice displacement $\vec{u}$. The subscripts n, s denote normal and superfluid components respectively while i, j, k are coordinate indices. Here and in the rest of the chapter summation over repeated coordinate indices is implied.

The linearized hydrodynamic equations of motion [34] are:

$$\begin{aligned} \partial_t \rho + \partial_i g_i &= 0, \\ \partial_t g_i + \partial_k \Pi_{ik} &= 0, \\ \partial_t s + \partial_i f_i &= -\frac{q_i}{T^2}\partial_i T, \\ \partial_t v_{si} + \partial_i \phi &= 0, \\ \partial_t u_i &= v_{ni}. \end{aligned} \tag{4.7}$$

where

$$\begin{aligned} g_i &= \rho_{sik}(v_{sk} - v_{nk}) + \rho v_{ni}, \\ \Pi_{ik} &= -\eta_{iklm}\partial_m v_{nl} - \zeta_{ik}\partial_l j_{sl} + P\delta_{ik} - \lambda_{ki}, \\ f_i &= s v_{ni} + \frac{q_i}{T}, \\ \phi &= -v_{sk}v_{nk} + \zeta_{ik}\partial_k v_{ni} + \chi \partial_k j_{sk}. \end{aligned} \tag{4.8}$$

These expressions can be found, with one minor [129] difference in Ref. [34]. In the expression for the momentum flux tensor (Π_{ik}) above, the tensor with components η_{iklm} is a shear viscosity arising from the normal component. On the other hand, the tensor ζ_{ik} and the scalar χ are "second viscosity" coefficients arising from coupling between normal and superfluid components. Also, f_i is the entropy flux and q_i is the thermal current.

Having established a framework for calculating the energy dissipation associated with dislocation motion, we now turn to the evaluation of the strain term contribution to the mobility.

4.2.2 Contribution of the strain term to the mobility

We now explain the procedure used to calculate the dislocation mobility. We illustrate the details by considering first the contribution to M arising from the energy dissipation E_{strain} associated with the strain field (w_{ik}) of the dislocation line. Other contributions will be discussed later. The expression for this source of energy dissipation is obtained by making use of Eqns. (4.4), (4.6) and (4.8):

$$\begin{aligned} \dot{E}_{strain} &= \lambda_{ik}\dot{w}_{ik} \\ &= (-\eta_{kilm}\partial_m v_{nl} - \zeta_{ki}\partial_l j_{sl} + P\delta_{ki} - \Pi_{ki})\partial_i \dot{u}_k, \end{aligned} \tag{4.9}$$

where the overdot denotes the time derivative. Following Ref. [32], $\vec{u}$ is the displacement field of the crystal lattice sites from their equilibrium positions due to a dislocation line moving with constant velocity $\vec{V}_D$. Thus, we assume the space and time dependence of $\vec{u}$ to be of the form

$$\vec{u}(\vec{r},t) = \vec{u}(\vec{r} - \vec{V}_D t), \tag{4.10}$$

which implies

$$\partial_t \vec{u} = -(\vec{V}_D \cdot \vec{\nabla})\vec{u} \tag{4.11}$$

corresponding to the velocity of atoms moving with the dislocation line. Also, $\vec{v}_s = \partial_t \vec{u}_s(\vec{r} - \vec{V}_D t)$, is the velocity of superfluid atoms due to the moving dislocation line. Keeping the relevant dissipative terms in $\dot{E}_{strain}$, which lead to a V_D^2 dependence (for example in the term $\eta_{kilm}\partial_m v_{nl}\partial_i \dot{u}_k$ both v_{nl} and $\dot{u}_k$ depend on V_D), we have:

$$\lambda_{ik}\dot{w}_{ik} = (-\eta_{kilm}\partial_m v_{nl} - \zeta_{ki}\partial_l j_{sl})\partial_i \dot{u}_k \tag{4.12}$$

where, $j_{sl} = \rho_{slk} v_{sk}$ and v_n are the supercurrent and the normal fluid velocity. Making then use of Eq. (4.2), we have for the energy dissipated in the strain field of the dislocation line:

$$\begin{aligned} F_D V_D|_{\eta,\zeta} &= -\int \dot{E}_{strain} d^2 r, \\ &= \int (\eta_{kilm}\partial_m v_{nl}\partial_i \dot{u}_k + \zeta_{ki}\partial_l j_{sl}\partial_i \dot{u}_k) d^2 r, \end{aligned} \tag{4.13}$$

where the notation in the left side denotes the contribution from the η and ζ tensors, under examination. We now establish a coordinate system with the z axis directed

along the dislocation line and the x axis along the velocity. We then perform a two dimensional Fourier transform for the displacement field in the transverse directions:

$$\vec{u}(\vec{r}) = \int \vec{u}(\vec{q}) e^{i\vec{q}.\vec{r}} d^2q. \tag{4.14}$$

We illustrate below the steps involved in evaluating the inverse dislocation mobility contribution due to the shear viscosity term η_{kilm} in Eq. (4.13) above. The inverse mobility contribution from the term ζ is evaluated in a very similar way. The next steps, then, involve collecting the contributions from different dissipative coefficients in Eqs. (4.4) and (4.8). Inserting the Fourier transform of the displacement field as in Eq.(4.14) into Eq.(4.13) (also using the last of Eq.(4.7)) we obtain

$$\begin{aligned} F_D V_D|_\eta &= \int (\eta_{kilm} \partial_m v_{nl} \partial_i \dot{u}_k) d^2r \\ &= \int [\eta_{kilm} \partial_m (\vec{V}_D \cdot \vec{\nabla}) \int u_l(\vec{q}_1) e^{i\vec{q}_1 \cdot \vec{r}} d^2q_1 \partial_i (\vec{V}_D \cdot \vec{\nabla}) \int u_k(\vec{q}_2) e^{i\vec{q}_2 \cdot \vec{r}} d^2q_2] d^2r \\ &= \eta_{kilm} \int \int i q_{1m} (i\vec{V}_D \cdot \vec{q}_1) u_l(\vec{q}_1) e^{i\vec{q}_1 \cdot \vec{r}} d^2q_1 \int i q_{2i} (i\vec{V}_D \cdot \vec{q}_2) u_k(\vec{q}_2) e^{i\vec{q}_2 \cdot \vec{r}} d^2q_2 d^2r. \end{aligned} \tag{4.15}$$

Noting that the integral over the 2D plane leads to a two-dimensional $\delta(\vec{q_1} + \vec{q_2})$ and using this delta function to integrate over $\vec{q_2}$ one then obtains

$$F_D V_D|_\eta = \eta_{kilm} \int q_{1m} q_{1i} u_l(\vec{q}_1) u_k(-\vec{q}_1) (V_D^2 q_{1x}^2) d^2q_1. \tag{4.16}$$

To estimate this contribution to the mobility it is sufficient to consider the diagonal component of the viscosity, the ordinary $\eta \equiv \eta_{iiii}$. Then, the rate of energy loss in the strain field of a dislocation line simplifies to:

$$F_D V_D|_\eta = \eta \int q_{1i} q_{1i} u_i(\vec{q}_1) u_i(-\vec{q}_1) (V_D^2 q_{1x}^2) d^2q_1. \tag{4.17}$$

By simplifying the equation above and finding the inverse mobility of the dislocation line as explained after Eq.(4.3) we obtain for this contribution to M^{-1}:

$$M^{-1}|_\eta = \eta \int_{q_{min}}^{q_{max}} q_{1i}^2 |u_i(\vec{q}_1)|^2 q_{1x}^2 d^2q_1 \tag{4.18}$$

where $q_{min} = 1/L$, L being a cutoff of order of the size of the crystal, or the distance between dislocations, and $q_{max} = 1/b$ with b (the magnitude of Burgers vector) approximately comparable to the interatomic spacing. To obtain $\vec{u}(\vec{q})$, (the Fourier transform

of the elastic displacement field) we note that the gradient of the elastic displacement field is roughly constant in magnitude over a circular path of radius r centered on the dislocation line [32] i.e.

$$(\nabla u) r \approx b. \tag{4.19}$$

Fourier transforming the elastic displacement field then leads to:

$$u(\vec{q}) \approx \frac{b}{q^2}. \tag{4.20}$$

Substituting Eq. (4.20) into Eq. (4.18) we finally have:

$$\begin{aligned} M^{-1}|_\eta &= \frac{\eta}{2}(1 - \frac{b^2}{L^2}), \\ &\sim \frac{\eta}{2}. \end{aligned} \tag{4.21}$$

since obviously $b \ll L$.

As mentioned above, in addition to this term arising from η, which we have discussed in detail, and the corresponding contribution from the ζ tensor, written down in Eq. (4.13) and computed in the same way as the η term, there are several additional contributions to the dissipation all arising from terms in Eq. (4.4). We can ignore the contribution from the $T\dot{S}$ because we are interested in the limit where $T \to 0$. Also, since we are interested in the limit where V_D is small compared to the speed of sound (in solid ^{4}He) the inertial contribution to energy dissipation, $\vec{v}_n \cdot \dot{\vec{g}}$, can be neglected [32]. There are additional contributions to the mobility of the dislocation line arising from the $\phi\dot{\rho} + \vec{j}_s \cdot \dot{\vec{v}}_s$ terms in Eq. (4.4). These involve again the tensor ζ, this time via the last of Eqs. (4.8) and also, via the same equation, the scalar χ. These contributions can be calculated following similar procedures to those discussed above and there is no need to repeat the details. Finally, putting together all of these contributions, the total inverse mobility of the dislocation line in a quantum crystal can be written as

$$M^{-1} \approx \frac{\eta}{2} + \frac{\rho_s}{\rho}(\zeta\rho + \chi\rho^2). \tag{4.22}$$

This is our basic result for the mobility.

4.2.3 Relation between shear modulus and mobility

We will now proceed further to relate the observed shear modulus of a quantum crystal to the mobility of a dislocation line. This will enable us to discuss the experimental

results of Ref. [114].

When a stress σ is applied to a crystal, the dislocation line feels a force per unit length, $F_D = b\sigma$. As the dislocation line glides in response to the applied force, the displacement of the dislocation line results of course in a strain ϵ_D in addition to the strain ϵ_{el}. Here the elastic strain ϵ_{el} is the response of the crystal in the absence of dislocation lines. Therefore, the effective shear modulus μ i.e. the ratio of applied stress to total strain is given by [114] $\mu = \sigma/(\epsilon_D + \epsilon_{el})$. This can also be written as

$$\mu = \frac{\mu_{el}}{1 + \frac{\epsilon_D}{\epsilon_{el}}}, \tag{4.23}$$

where $\mu_{el} = \sigma/\epsilon_{el}$ is the elastic shear modulus. The strain due to the motion of the dislocation line is known to be [130, 131]

$$\epsilon_D = \rho_D b x_a, \tag{4.24}$$

where ρ_D is the dislocation number density and x_a is the average displacement of the dislocation line through the crystal. In order to determine the average displacement, we look to the applicable equation of motion [132] of the dislocation line

$$M^{-1}\dot{x} = b\sigma \tag{4.25}$$

where x is the dislocation displacement as a function of time. We can then relate the average displacement of the dislocation to its velocity and to the mobility mobility via $x_a = V_D\tau$ (where τ is the characteristic time scale associated with the movement of the dislocation line) and Eq. (4.1) to obtain $\epsilon_D = F_D\tau\rho_D bM$, which agrees with Eq. (4.25) and $F_D = b\sigma$. For the purposes of estimating the the average displacement x_a, we will, working as in Ref. [126] in the quasistatic limit, replace τ by the inverse of the slowest range of frequencies for the strain ϵ applied to the crystal in the experimental [114] situation.

Putting together these considerations, the shear modulus of the crystal as a function of the mobility of the dislocation line is found to be

$$\mu = \frac{\mu_{el}}{1 + \frac{F_D\tau\rho_D bM}{\epsilon_{el}}}. \tag{4.26}$$

We will now be able to use this result, combined with that for the mobility in the previous subsection (Eq. (4.22)) to discuss the behavior of the elastic coefficient in solid Helium.

The expressions derived above for the amplitude of displacement and ϵ_D are valid under the standard [125, 126] quasistatic limit assumptions. This is applicable in the usual experimental situation since the dislocation acceleration time is small compared to the time over which strain is applied to the crystal [133]. However, we can also consider the higher-frequency limit (the "ac" limit) when the dislocation line executes elastic string motion *out of phase* with the applied strain. Considering then, $x(t) = x_0 e^{-i\omega t}$ and $\sigma(t) = \sigma_0 e^{-i\omega t}$ one obtains from Eq.(4.25):

$$x_0 = \frac{ib\sigma_0}{M^{-1}\omega}. \tag{4.27}$$

Following then the same steps as in the previous case we can easily find $\mu(\omega)$ in this "ac" limit. The quantity of interest here is the Q factor $\left|Q^{-1}\right| = |Im[\mu]/Re[\mu]| = \epsilon_R$. Defining $\epsilon_R(\omega) \equiv \frac{\rho_D b F_D M*(1/\omega)}{\epsilon_{el}}$ as a ratio involving strains, one finds that $Im[\mu] = -\epsilon_R Re[\mu]$, leading to the expression for the Q factor, $\left|Q^{-1}\right| = |Im[\mu]/Re[\mu]| = \epsilon_R(\omega)$.

4.3 Results - Modeling of Experimental Shear Modulus Data

Having derived the mobility of the dislocation line and its relation to the shear modulus of a quantum crystal, we now discuss how to connect our theory to the experimentally observed large and sudden softening of the shear modulus seen [114] in solid ^{4}He as the temperature is increased. Thus, we will seek to model the temperature dependence of the shear modulus data. Results in Ref. [114] show that at the higher temperatures studied, (up to 1K), the crystal is softer, with μ being independent of temperature. As the temperature is lowered, it is seen that between $T = 0.05$K and 0.1K μ rises sharply, and then, at lower temperatures, it saturates to a value identified with the intrinsic value μ_{el}. It is evident from earlier studies [123, 124] that dislocation lines play an important role in determining the elastic properties such as shear modulus of a crystal. Pinning due to impurity atoms and collision with thermal phonons have been considered to be the dominant source for damping of dislocation line motion in recent experiments [121, 122]: hence we have to compare these sources of damping with the superfluid contribution in order to ascertain their relative importance. In ^{4}He crystals, dislocation lines can glide almost freely along the basal planes of the hexagonal crystal

structure [121]. As a consequence, the effect of the shear viscosity (i.e. the dissipation due to η, arising from interactions between the dislocation line and the surrounding atoms) can be neglected. It follows from the above argument that the expression for the dislocation mobility, Eq. (4.22) then simplifies to:

$$M^{-1} \approx \frac{\rho_s}{\rho}(\zeta\rho + \chi\rho^2). \tag{4.28}$$

An important consequence of this result is that a superfluid field makes it harder for the dislocation line to move. Since the inverse mobility is directly proportional to the superfluid fraction, at lower temperatures (as $T \to 0$) when we expect ρ_s/ρ to be larger, it is harder for the dislocation line to move. Even though this appears to be counterintuitive, it can be understood by recalling that Couette viscometer [134] and vibrating wire [135] experiments show that liquid ^{4}He is characterized by a very small viscosity of order 10^{-5} kg/ms below 1K. This is relevant because the small viscosity contribution from the superfluid field could be the dominant source of dissipation for a dislocation line in a quantum solid.

We can now numerically estimate the inverse mobility of the dislocation line. To do so, we will use the values of the second viscosity coefficients $\rho\zeta \sim 10^{-5}$ kg/ms and $\rho^2\chi \sim 7 * 10^{-5}$ kg/ms for liquid ^{4}He [136, 137]. These coefficients are not known for solid ^{4}He. We will then obtain corresponding estimates for the dislocation mobility both above and below the assumed superfluid transition temperature (or crossover) in solid ^{4}He crystals. For the purposes of estimating the temperature at which a superfluid field associated with dislocations may arise in solid ^{4}He crystals, we consider a scenario where a loosely intersecting grid of dislocations forms. According to Refs. [24, 138] dislocation network superfluidity is characterized by two temperature scales - $T_0 \sim 1$K (comparable to the bulk λ temperature for liquid ^{4}He) and $T_c \sim T_0 a/L_f$, where a is the interatomic distance along a dislocation core and L_f is the free segment length of dislocation line. Within such a model for superfluidity associated with dislocation lines, the onset temperatures are roughly consistent with the experimentally [114, 139, 11] found range 0.1K to 0.075K where the onset of anomalous behavior is observed. As to the numerical value of the putative superfluid fraction ρ_s/ρ we look to quantum Monte Carlo calculations involving solid ^{4}He. For solid ^{4}He with hcp lattice configuration, the superfluid fraction (ρ_s/ρ) was calculated to have an upper limit in the range of 0.3 to

0.9 [34]. Monte Carlo simulations with dislocations characterized by core superfluidity find that nearly all atoms in the core of a dislocation line are in the superfluid state [26]. We will conservatively take the value $\rho_s/\rho \sim 0.1$ in the $T \to 0$ limit.

Using these order of magnitude values we can obtain, via Eq. (4.28), an approximate value for the inverse mobility (M^{-1}) at low T namely $\sim 10^{-5}$ kg/ms. In some of the previous work [140], damping of dislocation motion was thought to be mainly due to phonon collisions and pinning effect due to the presence of ^{3}He impurities, resulting in inverse mobilities of order 10^{-9}kg/ms and 10^{-8}kg/ms, respectively, at 1K. Hence, our results indicate that quenching of dislocation motion due to superfluid field may be the dominant source of damping for dislocation motion in the low temperature limit. In this limit, the superfluid contribution to dislocation damping is larger by at two or three orders of magnitude compared to the other sources of damping.

In order to estimate the magnitude of the shear modulus using Eq. (4.26), (with Eq. (4.28)), we need also the relevant values of the other parameters entering that equation. From experimental results [121, 114], we have $F_D \sim 10^{-11} N/m$, $\rho_D \sim 10^6 m^{-2}$, b $\sim 10^{-10} m$ and $\epsilon_{el} \sim 10^{-8}$. As mentioned above, we use the inverse of the applied frequency, in the low range, $\omega \sim 1$ Hz - 50 Hz, to estimate τ. This should be better at lower frequencies. Inserting the values of the various parameters into Eq. (4.26) and taking $M^{-1} \sim 10^{-5}$ kg/ms in the low T limit as mentioned above, we obtain the ratio in the denominator of that equation to be

$$\frac{F_D \rho_D b M \tau}{\epsilon_{el}} \sim 10^{-3} - 10^{-5}. \tag{4.29}$$

It can then be easily seen from Eq. (4.26) that $\mu \approx \mu_{el}$ in the low T regime. Thus, at low temperatures (below $T \sim 0.03$K), we find that the shear modulus becomes independent of T at $\mu \approx \mu_{el}$, a result that should not depend on frequency at low ω. In comparing the experimental results for the shear modulus with our model (see Fig.4.1), we note that the low temperature behavior of this shear modulus is well accounted for in our theory.

Examining now the behavior of the dislocation mobility above the temperature where the assumed superfluid behavior disappears, we note that the contribution to the inverse mobility due to the superfluid field approaches zero as $\rho_s/\rho \to 0$. Then, other damping effects such as phonon scattering and pinning due to impurities are likely to become

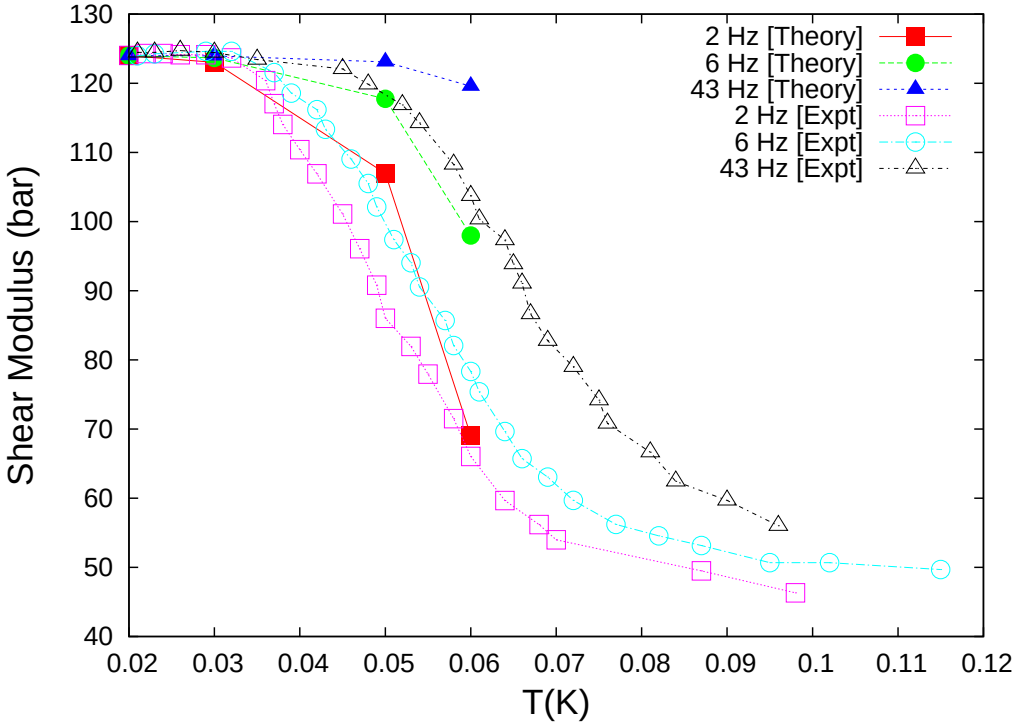

Figure 4.1: Experimental results for the shear modulus vs temperature at different frequencies, ω, of applied strain (see legend) are compared with theoretical results. See text for discussion.

more important. The experimental range of temperatures where the sharp change in shear modulus is found in solid ^{4}He (as mentioned above), is accounted for in our theory. In order to estimate the order of magnitude of the shear modulus in the higher temperature range (T $\geq$ 0.03K) we first note [114, 121] that $M^{-1} \sim 10^{-8}$ kg/ms at $T = 0.06K$. This implies that the ratio on Eq. (4.29) is of order unity and $\mu \approx 0.5\mu_{el}$. At the intermediate value $T = 0.05K$ we interpolate $M^{-1} \sim 5 * 10^{-7}$ kg/ms. At lower T the precise value of M^{-1} becomes irrelevant. The results thus obtained are displayed in Fig. 4.1 in comparison to experimental results from Ref. [114]. Other parameter values used there are, except of course for ρ_s, the same as in the low temperature range. As shown there, the drop in shear modulus is modeled quite well by Eq. (4.26) and the above considerations, specially at the lowest frequencies. In the higher frequency range considered the quasistatic approximations might start to break down. We also note that at a given temperature, as the frequency ω is lowered the value of the shear modulus decreases in agreement with experimental data.

Considering now the higher frequency "ac" limit, we focus, as mentioned above, on the Q factor. In Fig. 4.2, we plot the dissipation associated with dislocation line vibration, Q^{-1} (i.e. arising from the phase difference between σ and ϵ) as obtained from $\left|Q^{-1}\right| = \epsilon_R$ (see discussion at the end of Sec. 4.2.3). Dissipation is small at low temperatures and increases with T. The numerical values of the parameters used in calculating Q^{-1} are the same as for the shear modulus. The experimental results [114, 122] for Q^{-1} in the low T limit are again consistent with theory: the disagreement is now greater at very low frequencies, as one would expect. At temperatures near the superfluid onset temperature, we note that experimentally the dissipation decreases with larger values of ω.

Next, we discuss some of the limitations of our model. First, the calculated dislocation mobility in the hydrodynamic limit provides probably a lower limit to this quantity since we do not take into account the core strain effects of the dislocation line. Also, as noted above, the second viscosity coefficients used in calculating the mobility are for liquid ^{4}He rather than for solid ^{4}He, due to the lack of experimental data in the solid phase. Since one might reasonably expect the second viscosity coefficients for solid ^{4}He to be somewhat larger than in the liquid, it is possible that even for smaller ratios of ρ_s/ρ than the value $\rho_s/\rho \sim 0.1$ considered here the superfluid contribution to the

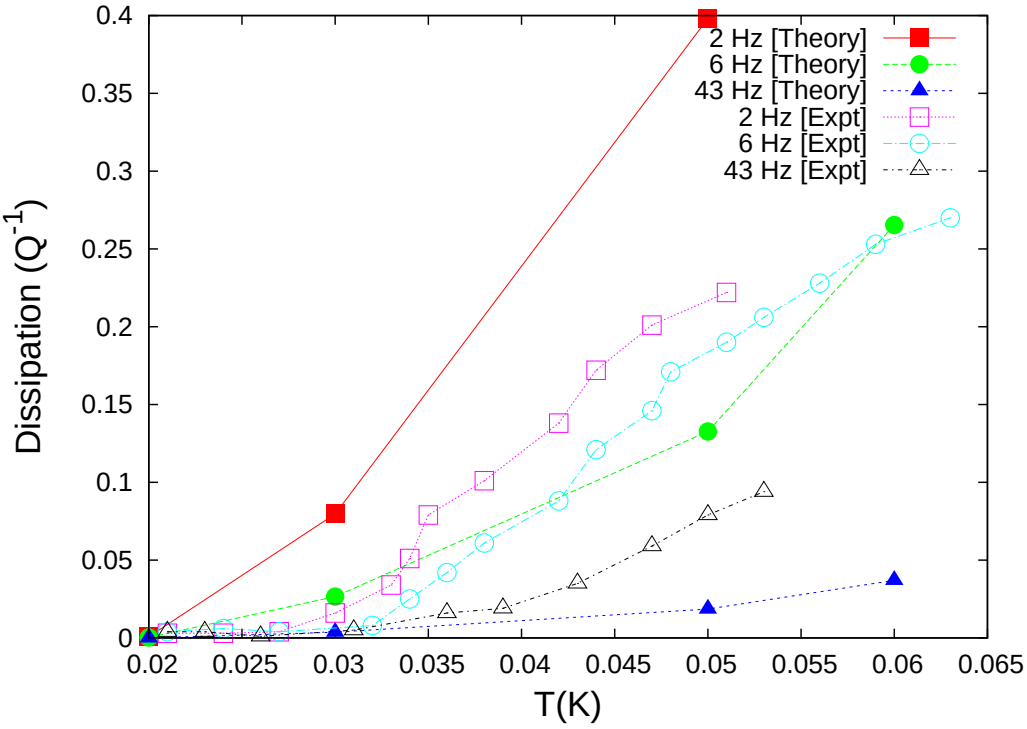

Figure 4.2: Dissipation (Q^{-1}) vs temperature at different frequencies, ω, of applied strain (legend). Experimental data are compared with theory, as discussed in the text.

dislocation mobility could still be significant compared to the contribution from phonon scattering or pinning effects due to impurities. These reasons, then, might account for the remaining differences in the magnitude of the temperature dependence of the shear modulus and dissipation as shown in Figs. 4.1 and 4.2. More detailed knowledge of the phonon and impurity effects is thus, we believe, likely to lead to a more quantitative agreement in the higher T limit.

4.4 Summary

We have begun, in section 4.2.1 of this chapter, by presenting a calculation of the dislocation mobility in solid ^{4}He. This calculation is based on well known hydrodynamic results [34] and follows a procedure developed in Ref. [32]. The result is expressed in terms of the bulk "second viscosities" of the superfluid crystal hydrodynamics, and the value of ρ_s. Numerical estimates of the mobility, although rather uncertain, indicate that an assumed superfluid field associated with dislocation lines, may play an important role in dislocation mobility and therefore in the stiffness of the crystal. An important consequence of this is that superfluid damping of dislocation motion can model the large and sudden increase in shear modulus observed experimentally in solid ^{4}He as the temperature is decreased, as seen in Fig. 4.1. At low temperatures, below 200mK, solid ^{4}He crystals stiffen considerably. This is thought to be due to pinning of dislocation network by ^{3}He impurities and damping of dislocation motion due to phonon collisions. However, we find that as the superfluid fraction increases at lower temperatures the dislocation mobility decreases resulting in the stiffening of the crystal. Numerical estimates of the change in shear modulus and the Q factor based on this effect model experimental behavior quite well, as can be seen from the figures. The quantitative agreement might be even better when it is taken into account that bulk viscosities of solid ^{4}He are likely be larger than the values for liquid ^{4}He used in the mobility estimates. We have used the known values of these quantities for the liquid, as information for their values in the solid is lacking.

Our results then show that quenching of dislocation motion due to a superfluid field could be the dominant source of damping for dislocation motion in the low temperature

limit. In this limit (i.e. $T \leq 0.04K$), we find that the superfluid contribution to dislocation damping is considerably larger than that due to other sources of damping (phonons and impurity pinning). The superfluid contribution dominates because, experimentally, it is seen that limitation of dislocation motion in conventional crystals due to Peierls barrier is absent in solid ^{4}He. The onset temperature of this unusual elastic behavior in solid ^{4}He is in the same temperature range as the onset of superfluid behavior in [24, 138] dislocation networks. As noted above, the superfluid contribution to dislocation mobility scales with the superfluid fraction i.e. ρ_s/ρ. The onset temperature of the superfluid fraction is reflected, in our model, in the temperature dependence of the shear modulus effect. This enables us to model both the magnitude and the temperature dependence of the change in shear modulus of solid ^{4}He crystal. At higher temperatures, the factor ρ_s/ρ becomes smaller and eventually approaches zero. In this limit, other contributions to damping (such as due to phonon collisions and ^{3}He impurities) become more important. Therefore, we believe that the interplay of these effects - superfluid field, ^{3}He impurities and phonon collisions - should be considered in understanding the anomalous softening of the ^{4}He crystal.

Given how the superfluid field influences dislocation mobility, the movement of the dislocation line could also have an effect on the associated superfluid field. For a dislocation line moving with constant velocity V_D, a study of how the associated superfluid field reacts forms the subject matter of the next chapter.

Chapter 5

Edge Dislocation Dynamics and Its Effect on the Superfluid Field

5.1 Introduction

Research on topics associated with NCRI and quantum crystals were given a new impetus after Kim and Chan claimed [11] to have observed a period drop in torsional oscillator (TO) experiments with solid ^{4}He. Evidence that disorder present in the crystal ^{4}He could play an important role became apparent early on (see Section 1.3.1 for details). It was observed that annealing the solid ^{4}He samples eliminated the purported drop in TO period attributed to NCRI at the time. TO results were also found to be strongly dependent on sample preparation methods and quality of samples [141]. Recently, the emerging consensus seems to be that defects present in the crystal, such as dislocation lines, could have an important role [45] to play in understanding a variety of experimental results associated with solid ^{4}He. The role that dislocation lines play in determining the elastic properties of solid ^{4}He crystals has been well known [111]. An example of this is the anomalous shear modulus effect in solid ^{4}He and subsequent explanation of it based on dislocation motion damping [114]. This effect was studied in detail in Chapter 4.

A quantum liquid state associated with disorder present in crystal ^{4}He was expected to lead to novel quantum phenomena. The possibility that a superfluid field present

within solid ^{4}He could be behind the 'torsion oscillator anomaly' was investigated immediately afterwards. Superfluid grain boundaries were proposed as a candidate to explain the torsion oscillator results [142]. Earlier work by Shevchenko [24] raised the possibility that superfluidity could be present along network of defects such as screw and edge dislocations. Recent theoretical work on quantum Monte Carlo calculations involving dislocation lines showed [25, 26] that cores of dislocation lines can be superfluid. As an example of a novel quantum effect, coupling between the superfluid field and the elastic strain field due to a dislocation line in the context of phenomenological Landau theories [29, 143] showed that a stationary edge dislocation line can enhance superfluidity in its vicinity. However, previous studies focused on the case where the dislocation line is quenched or stationary. The importance of considering the dynamics of dislocation lines was motivated previously in Section 3.1 in the context of annealed vs quenched dislocation network. In reality, dislocation lines are dynamic objects that execute a variety of motions. Dislocation line segments can undergo roughening [107] and in response to an applied stress can execute two basic types of motion: climb or glide motion. These two different types of motion are illustrated in Figs. 5.1 and 5.2. When a dislocation moves along the surface that contains both its line and Burgers vector it executes glide motion. Movement out of the glide surface perpendicular to the Burgers vector is referred to as climb. Glide and superclimb i.e. climb assisted by superfluidity associated with dislocation cores in solid ^{4}He were studied previously [138] in the context of elastic effects such as dislocation line tension and compressibility. Dislocation lines are known to glide freely along basal planes in solid ^{4}He at relatively higher speeds compared to other crystals. This is thought to be a quantum effect which causes the Peierls barrier to dislocation motion to be negligible [122].

Considering the quantum nature of dislocation lines and the prevalent experimental methods involved in solidifying ^{4}He confined to small cells at high pressures, it is important to study the effect of dynamics of the dislocation line. High stresses present will induce dislocation motion and this motion may significantly affect the superfluid field in its vicinity. In particular, I am interested in learning whether the motion of the dislocation line enhances or suppresses the associated superfluid field. Previously (see Chapter 3), I simulated a dislocation network using a coupled field Ising model in order to study the effect of the dynamics of the dislocation line on the associated superfluid

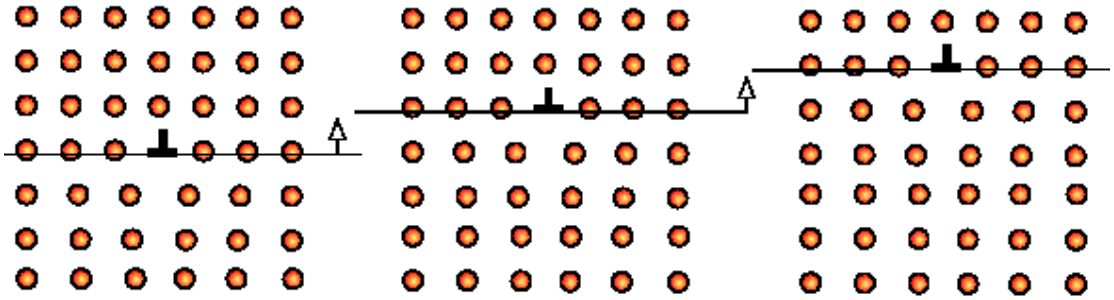

Figure 5.1: An edge dislocation is illustrated executing climb motion. Motion in the direction of the arrow indicates climb.

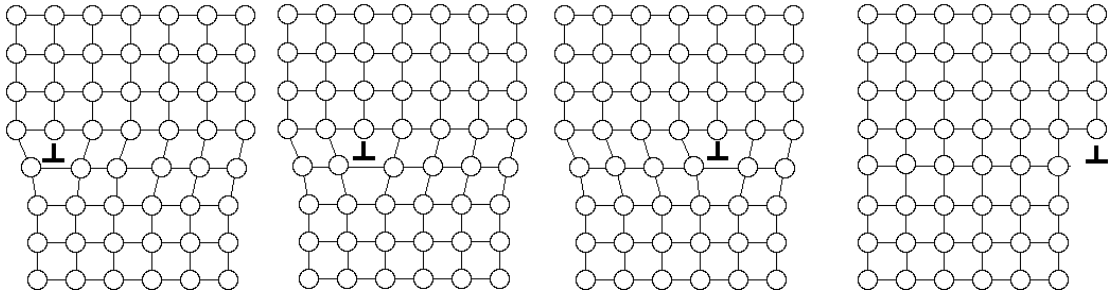

Figure 5.2: An edge dislocation is shown gliding.

field. Preliminary results based on mapping a dislocation network to a random Ising model showed that dynamics of the dislocation line can indeed have a measurable effect on the superfluid field in its vicinity. Further research into the motion of dislocation lines in solid ^{4}He showed that the superfluid field makes it harder for dislocation lines to move. This provided an alternative superfluid field based explanation for the anomalous shear modulus effect (see Chapter 4 for details). Given these results, studying a fully quantum model coupling superfluid field to the dislocation line forms the subject matter of this chapter.

I am interested here in studying the effect of the dynamics of a dislocation line on the superfluid field at the microscropic level i.e. at the quantum level. The response of the superfluid field due to an edge dislocation line assumed to be driven at constant velocity $\vec{V}_D$ for both climb and glide will be analyzed. Focusing on smaller length and time scales, fluctuations in the amplitude and phase of the superfluid order parameter are studied computationally. The fluctuation in amplitude was not included in the

coarse-grained models studied before, because this amplitude is a non-hydrodynamic variable (i.e. it relaxes quickly at long wavelengths). A mathematical model that is successful in describing superfluidity in ^{4}He is the Gross-Pitaevskii equation [144, 145]. The Gross-Pitaevskii equation (GPE), also referred to as the nonlinear Schrödinger equation (NLSE), describes the equilibrium state and dynamics of low-temperature superflow and Bose-Einstein condensates (BEC) [36] well. However, the GP formalism does not contain a description of damping and can only be used to study dissipationless fields. As I am interested in exploring what quantum models predict on how superfluid field near a dislocation is damped due to the motion of a dislocation line, a method to include dissipation in GPE is necessary. Dislocation motion is expected to smear the superfluid field over a wider region thereby counteracting the ability of the dislocation line to support superfluidity near it [22]. With this purpose in mind, an approach similar to Ref. [146] in order to study damping of superfluidity near the λ point is used. A required modification is introduced into the GPE, as in Ref. [146], in order to capture the effects associated with damping. This is referred to as the Dissipative Gross-Pitaevskii equation (DGPE) [147]. Based on the DGPE formalism, I present in this chapter a study of how the excitations associated with a moving dislocation line in solid ^{4}He affects the superfluid field near it.

The rest of the chapter is organized as follows. Introduction of the equations and details of the parameter values used are presented in Section 5.2. By coupling the elastic strain field due to the dislocation to the superfluid order parameter, I study within the DGPE formalism what effect the motion of a single edge dislocation line has on the superfluid field. Results from this study are presented in Section 5.3. I conclude this chapter by noting that the motion of the dislocation line plays an important role in determining the superfluid field distribution near it. During climb motion, part of the superfluid field associated with a stationary dislocation line is "left behind." Climb induces more asymmetry in the distribution of superfluidity near the dislocation line. No effect on the symmetry properties of the superfluid wavefunction is observed for glide. Decay of the superfluid field amplitude during climb and glide, although very small for experimentally realistic dissipation parameter, is observed.

5.2 Methods

Dissipative Gross-Pitaevskii equation

A single long, straight edge dislocation line running along the z axis is considered in this study (see Fig. 1.2). The Burgers vector for the edge dislocation is taken to be in the x-direction. The dislocation line is assumed to be long and straight so as to neglect edge effects and define the problem in the 2D $x-y$ plane orthogonal to it. The standard GPE which describes the motion of a field, ψ, is of the form (in 2D)

$$i\hbar\frac{\partial\psi}{\partial t} = \frac{-\hbar^2}{2m}\nabla^2_{x,y}\psi + v(x,y;t)\psi + g|\psi|^2\psi \tag{5.1}$$

where $\nabla^2_{x,y} = \frac{\partial^2}{\partial x^2} + \frac{\partial^2}{\partial y^2}$, m is the mass of an atom, $v(x,y)$ is the potential and g is the superfluid interaction parameter. On the right hand side, the first two terms are the kinetic and potential energy and the third nonlinear term describes the interaction energy between superfluid atoms. The repulsive interaction between superfluid atoms implies that $g > 0$ and is given by [152, 153]

$$g = \frac{4\pi\hbar^2 a_s N}{mL}. \tag{5.2}$$

Here a_s is the microscopic s-wave scattering length, N is the number of superfluid atoms and L is the size of the trap.

In the problem under study, the complex field ψ is the superfluid wavefunction and the coupling between ψ and the dislocation strain potential is introduced via the term $v(x,y;t)\psi$ [29]. For an edge dislocation along the z-axis (see Eq. (1.7)), the strain potential is of the form [29]

$$v(x,y) = \frac{A}{\sqrt{x^2+y^2}}\cos\phi, \tag{5.3}$$

where $\phi = \arctan(x/y)$ is an azimuthal angle defined in the $x-y$ plane with respect to the y axis. The parameter A, a positive quantity, denotes the strength of the dislocation potential and depends on the lattice and elastic constants of the solid. For $A > 0$, this potential is attractive for $y < 0$ thereby allowing for bound states. For $y > 0$ the potential is repulsive. The potential is symmetric along the x axis (i.e. along the direction of the Burgers vector). These characteristics of the potential should be reflected on the wavefunction ψ as well.

The solution of the non-linear equation noted above is complicated due to the non-central nature of the potential [155]. The equilibrium steady state of the superfluid field at very low temperatures, $T \to 0$, is described by the time independent GPE

$$-\frac{\hbar^2}{2m}\nabla^2_{x,y}\psi + v(x,y)\psi + g|\psi|^2\psi = \mu\psi, \tag{5.4}$$

where μ is the chemical potential. For the equilibrium solution, the wavefunction is normalized according to

$$\mathcal{N} = \int_{-\infty}^{+\infty}\int_{-\infty}^{+\infty} |\psi|^2\, dxdy = 1. \tag{5.5}$$

The standard GPE (Eq. (5.1) above) contain no dissipative terms. The motion of the dislocation line is dissipative as a result of the various damping mechanisms within the crystal as discussed in Chapter 4. An overview of how dissipation is introduced into the GP formalism is provided here. Dissipation is introduced into the GPE via a dimensionless damping factor γ as in Ref. [147]. The dissipative GPE is of the form

$$i\hbar\frac{\partial\psi}{\partial t} = (1 - i\gamma)[-\frac{\hbar^2}{2m}\nabla^2_{x,y}\psi + v(x,y)\psi + g|\psi|^2\psi - \mu\psi], \tag{5.6}$$

where the damping factor γ which must be positive is phenomenologically introduced in a manner similar to Ref. [146]. The terms in the square bracket in the right hand side represent the change from the equilibrium state of the superfluid wavefunction due to dynamics, in our case the moving dislocation line. The damping factor γ is inversely proportional to a relaxation time and due to it neither energy nor $\mathcal{N}$ is conserved in Eq. (5.6). In the original study by Pitaevskii [146], the parameter γ was expressed in terms of the second viscosity coefficients of superfluid Helium. The dynamics of the ψ field including its damping due to elementary excitations from a moving dislocation line can now be described within the framework of Eq.(5.6). A similar equation with the factor $(1 - i\gamma)$ has been used in the study of soliton decay and damping of vortices [149, 150].

By numerically solving the two-dimensional (2D) time dependent DGPE with a moving dislocation potential (for either climb or glide motion), the response of the superfluid order parameter ψ can now be evaluated. As in Section 4.2.1 of Chapter 4, we consider a scenario where the dislocation line moves at a constant velocity $\vec{V}_D$ due to external forces.

Prior to presenting the details of the numerical simulation, an overview of the co-ordinate system and units used is presented here. It is convenient to rescale the length and time in terms of natural units. We choose for our unit of length the elastic correlation length ξ_{el} defined by equating the kinetic energy of the superfluid atoms to the potential energy due to the dislocation line $\frac{\hbar^2}{2m\xi_{el}^2} = \frac{A}{\xi_{el}}$. Similarly, we rescale time by the characteristic frequency $\omega_{el} \equiv \frac{\hbar}{2m\xi_{el}^2}$. Rescaling the wave function, the co-ordinates (using the standard cartesian x, y co-ordinate system) and time via $\bar{t} = \omega_{el}t$, $\bar{\psi} = \psi\xi_{el}$, $\bar{x} = x/\xi_{el}$ (similarly for $\bar{y}$), $\bar{v} = v/\hbar\omega_{el}$, $\bar{g}|\bar{\psi}|^2 = \bar{g}|\bar{\psi}|^2/\hbar\omega_{el}$ and $\bar{\mu} = \mu/\hbar\omega_{el}$ one obtains

$$i\frac{\partial\bar{\psi}}{\partial\bar{t}} = (1 - i\gamma)[-\bar{\nabla}^2_{x,y} + \bar{v}(x, y; t) + \bar{g}|\bar{\psi}|^2 - \bar{\mu}]\bar{\psi}. \tag{5.7}$$

The coefficient of the non-linear term is $\bar{g} \equiv \frac{2mg}{\hbar^2}$ and the strength of the dislocation potential, A, is rescaled such that $\bar{A} = A/\hbar\omega_{el}\xi_{el} = 1$ because of the definition of ξ_{el} and ω_{el}.

Numerical parameters and initial condition

The numerical values of the parameters used in solving Eq. (5.7) are explained here. The time dependent strain potential $v(x, y; t)$ in the DGPE depends upon whether the dislocation line is climbing or gliding. For motion along the positive y-axis (perpendicular to the Burgers vector), the dislocation potential depends on the velocity V_D as

$$v(x, y; t) = \frac{A}{\sqrt{x^2 + (y - V_D t)^2}} \cos\phi. \tag{5.8}$$

Movement of the dislocation perpendicular to the Burgers vector (along the $y > 0$ direction) is called climb. When the dislocation is moved in the direction of the Burgers vector along the x axis, i.e. with the corresponding potential being

$$v(x, y; t) = \frac{A}{\sqrt{(x - V_D t)^2 + y^2}} \cos\phi \tag{5.9}$$

it executes glide motion. Climb and glide motion of the dislocation line are considered separately in this study.

The magnitude of the climb and glide velocity in classical crystals is expected to be small especially at low temperatures. In a quantum crystal such as solid ^{4}He, however, the possibility of superclimb and glide assisted by superfluidity [138] enables one to

consider larger values of velocity. Glide velocities up to 0.01 m/s are considered in an experimental study [140] of dislocation velocities in solid ^{4}He. We take V_D near its upper range to be better able to observe its effects. To estimate the order of magnitude of ξ_{el}, the strength of the dislocation potential A (see Eq.(5.3)) with dimensions of energy*length has to be known. The magnitude of the parameter A depends on the energy per unit length of an edge dislocation line $E_{el} = Gb^2$ where G is the shear modulus of a solid and b the magnitude of the Burgers vector [156]. Defining the parameter $A = E_{el} * b * \xi_{el}$, one obtains $\xi_{el} \sim 10^{-9}m$. ω_{el} is, then, approximately $10^{10}Hz$ and $\xi_{el}\omega_{el} \sim 10\ m/s$. The magnitude of the quantities ξ_{el} and ω_{el} sets the scale for length and time dimensions in the simulation respectively. The units for V_D are $\xi_{el}\omega_{el}$. Dimensionless values of V_D ranging from 5×10^{-4} to 1.5×10^{-3} (i.e. between 0.005 m/s and 0.015 m/s) are used for both climb and glide motion in this simulation.

The strength of the interaction coefficient can be re-written as $\bar{g} \equiv 8\pi a_s \rho_{2D} \xi_{el}$ based on its definition and Eq. (5.2). The number density of superfluid atoms in 2D is $\rho_{2D} = N/\xi_{el}^2$. According to Ref. [154], the atomic number density of solid ^{4}He is $\rho_{3D} = 10^{28}/m^3$. For the spacing between atomic planes at $\sim 3 \times 10^{-10}$m [157], the number density in 2D (i.e. per atomic plane) is $3 \times 10^{18}/m^2$. The scattering length a_s for ^{4}He atoms is $\simeq 10^{-10}m$ [52]. The strength of the nonlinear interaction parameter is then $\bar{g} \sim 7.5$. Since this study is focused on the superfluid condensate density near a dislocation line, the above value for ρ_{2D} would greatly overestimate the condensate density. Assuming that a small percentage of atoms of order 1% condense into the superfluid state [26, 34] near the dislocations, a smaller value for $\bar{g} \sim 0.075$ is obtained. This is the value of $\bar{g}$ we have used.

In order to solve Eq. (5.7), the value of the chemical potential $\bar{\mu}$ is needed. The steady state GPE (see Eq. (5.4)) is numerically solved using a relaxation method under the condition that ψ satisfies Eq. (5.5) to obtain $\bar{\mu}$. The accuracy of this method was tested using the two dimensional Coulomb potential, the solutions of which are well known [155]. Thus, the value for $\bar{\mu} = -0.13$ was obtained consistent with other calculations [155] of the same parameter for a two dimensional Schrödinger equation with a non-moving dislocation line potential.

The value of the dimensionless damping parameter γ is also needed in order to solve the DGPE. In Ref. [147], the magnitude of γ depended on the rate at which

thermal particles above Bose-Einstein condensate band enters the condensate. This rate compared to the relevant trap frequency sets the order of magnitude of γ. Using a similar approach, comparing the energy dissipated by a moving dislocation line to the energy scale $\hbar\omega_{el}$, an estimate for γ appropriate for the problem under consideration can be obtained. The energy dissipated during dislocation motion is roughly $F_D * L * b$ where F_D is the force per unit length applied on a dislocation, L is the typical length of a dislocation line and b the magnitude of Burgers vector. The order of magnitude of these quantities for a dislocation line in solid ^{4}He were obtained from Ref. [114]. The value of the parameter γ thus obtained is $\sim 10^{-3}$.

An overview of initial condition and the numerical method used in the simulation is presented here. The equilibrium solution obtained from the time independent GPE (Eq. (5.4)) is set as the initial condition for ψ in the time dependent Eq. (5.7). At, $\bar{t} = 0$, the dislocation line is stationary and the superfluid distribution around it corresponds to the equilibrium case. As the dislocation line starts to move, the superfluid field ψ near it reacts. The response of the superfluid field is then studied for both glide and climb motion separately. Eq. (5.7) is solved using a split-step Crank-Nicolson method presented in Ref. [151]. For the simulation, a 1200×1200 square grid system with the size of each grid being $0.05\ \xi_{el}$ is used. A time step of $\delta\bar{t} = 0.01$ turns out to be adequate. A small cutoff is used in order to avoid the singularity associated with the dislocation potential at the origin. The results have been verified to be cutoff independent.

In relating the scenarios considered here to experiments, applying a stress on ^{4}He crystal causes the dislocation lines to move. Contribution of factors such as the superfluid field, thermal phonons or other impurities present within the crystal toward damping of dislocation motion was discussed in Chapter 4. The parameter γ takes into account the effect on the superfluid field due to the excitations that are induced by the dissipative motion of a dislocation line. In the results presented below, I investigate how climb and glide motion affects the superfluid field in its vicinity.

5.3 Results

In this section, I present the results of the DGPE simulation coupling a moving edge dislocation line to superfluidity. The effect of the movement of a dislocation line on

superfluidity near it is analyzed. The first part of this section deals with climb and the latter with glide motion of the dislocation line.

To obtain the initial condition, the time independent GPE (Eq. (5.4)) is solved to get the equilibrium solution for the superfluid field $|\bar{\psi}|$ near an edge dislocation line. The stationary potential Eq.(5.3) is used in solving Eq.(5.4). All lengths are in units of ξ_{el}, time in units of ω_{el} and velocity in terms of $\xi_{el}\omega_{el}$. The absolute value of the dimensionless wave function, $|\bar{\psi}|$ is plotted. 3D plots of the equilibrium superfluid distribution near an edge dislocation line at two different viewing orientations are shown in Fig. 5.3. Views along the $\bar{y}$ axis and $\bar{x}$ axis are presented in the top and bottom panel respectively. It can be seen that the bound state of the superfluid field forms in the attractive part of the dislocation potential (in the $\bar{y} < 0$ region). The dislocation potential is symmetric along the $\bar{x}$ axis with respect to the origin and asymmetric along the $\bar{y}$ axis. The symmetry characteristics of the potential can be seen in $|\bar{\psi}|$: an asymmetric accumulation of the superfluid field in the region $\bar{y} < 0$ can be observed.

We present now results for the climb case where Eq. (5.7) is solved with the dislocation potential in Eq. (5.8). Given that a stationary dislocation line enhances superfluidity near it, one naively expects that the motion of the dislocation line could then 'smear' this effect over a larger region. This could perhaps suppress the effectiveness of the dislocation line in enhancing superfluidity compared to the stationary case. The dislocation line is moved along the positive y direction at three different velocities $V_D = 5 \times 10^{-4}, 7.5 \times 10^{-4}$ and 1.5×10^{-3}. The movement of the superfluid field due to the spatial displacement of the dislocation line is illustrated in Fig. 5.4 through a plot of $|\bar{\psi}(\bar{x} = 0, \bar{y}; \bar{t})|$ at different times. At time $\bar{t}$, the dislocation line is displaced in the positive y direction by a distance of $V_D\bar{t}$. The top panel of Fig. 5.4 shows a plot of $|\bar{\psi}(\bar{x} = 0, \bar{y}; \bar{t})|$ at $\bar{t} = 0$, 6000 and 14000 for $V_D = 5 \times 10^{-4}$. The bottom panel shows the same quantity for $V_D = 1.5 \times 10^{-3}$ at three different values of $\bar{t}$. For $\bar{t} = 6000$ and $V_D = 1.5 \times 10^{-3}$, the dislocation line has moved a distance of $\sim 9\ \xi_{el}$. The shift in the superfluid distribution as a result of dislocation motion at other values of $\bar{t}$ and V_D can be clearly observed. The plot of $|\bar{\psi}(\bar{x} = 0, \bar{y}; \bar{t})|$ has a maximum at $\bar{y} = \bar{y}_{max}$. At $\bar{t} = 0$, $\bar{y}_{max}$ is at -1.3.

As the dislocation line executes climb motion, it appears from the figures that the

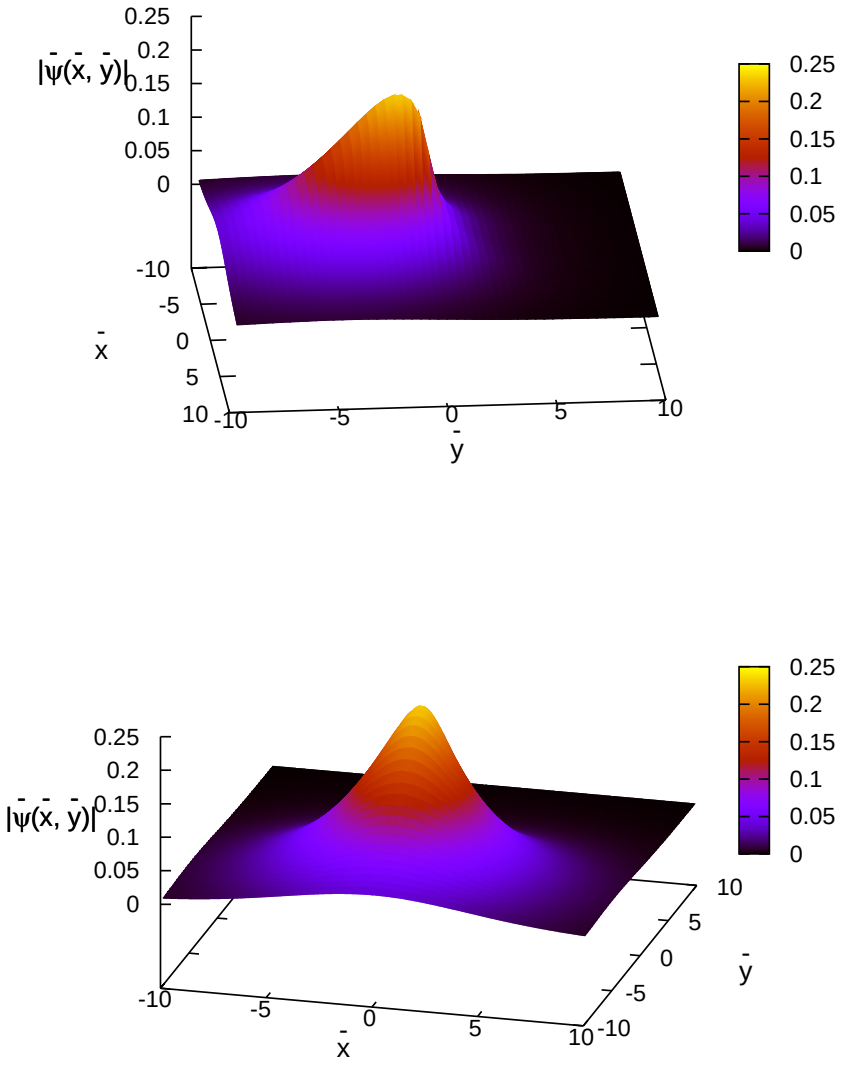

Figure 5.3: 2D equilibrium absolute value $|\bar{\psi}(\bar{x}, \bar{y})|$ of the superfluid field in the attractive part of the dislocation strain potential is shown at two different orientations. This is obtained by solving the time independent GPE.

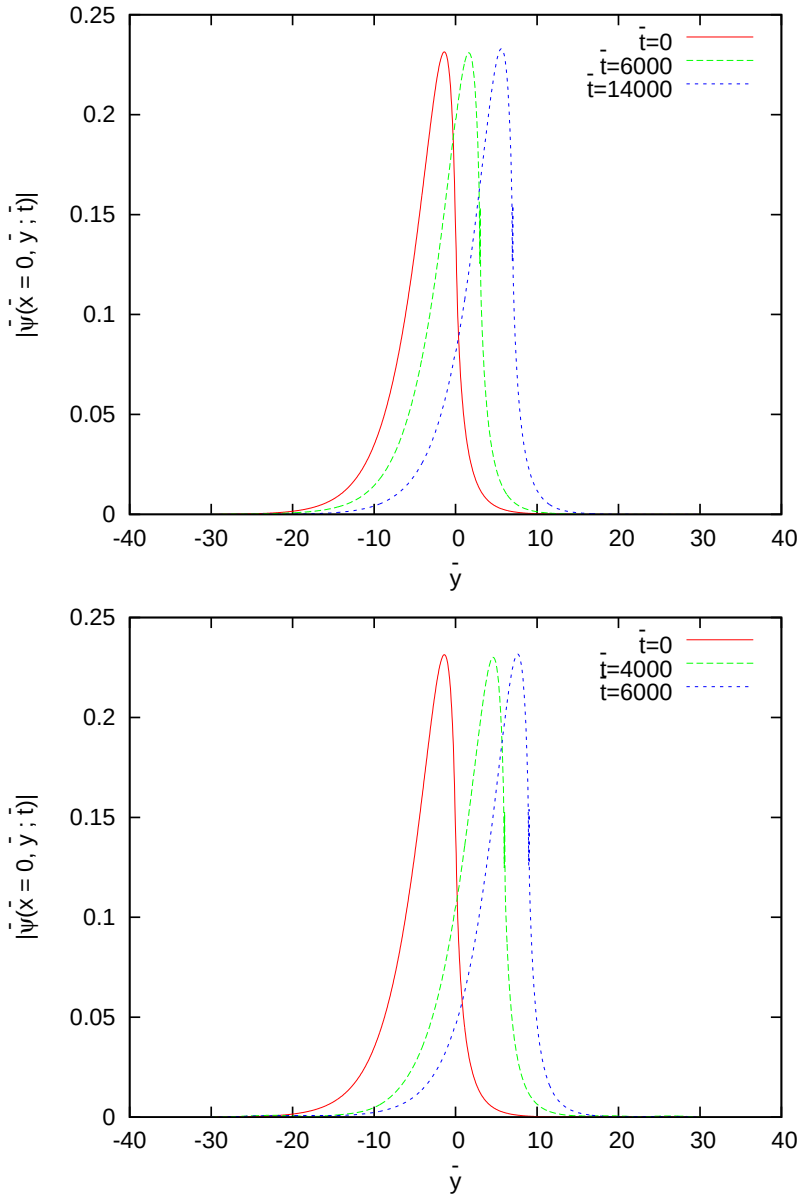

Figure 5.4: Plot of the 2D wavefunction $|\bar{\psi}(\bar{x}=0,\bar{y};\bar{t})|$ at different times for a climbing edge dislocation line. The top panel corresponds to $V_D = 5 \times 10^{-4}$ and the bottom panel $V_D = 1.5 \times 10^{-3}$.

superfluid distribution becomes more asymmetric in the y direction. Some of the superfluid amplitude is 'left behind.' In order to make this more evident, and to quantify it I define an asymmetry parameter B. The B parameter is defined in terms of the integrated norm of superfluid field in the region $\bar{y} < \bar{y}_{max}$ vs in the region $\bar{y} > \bar{y}_{max}$ over the 2D $x - y$ plane. Thus:

$$B = \frac{\int_{-\infty}^{+\infty} \int_{-\infty}^{\bar{y}_{max}} |\bar{\psi}|^2 \, d\bar{x} d\bar{y} - \int_{-\infty}^{+\infty} \int_{\bar{y}_{max}}^{+\infty} |\bar{\psi}|^2 \, d\bar{x} d\bar{y}}{\int_{-\infty}^{+\infty} \int_{-\infty}^{\bar{y}_{max}} |\bar{\psi}|^2 \, d\bar{x} d\bar{y} + \int_{-\infty}^{+\infty} \int_{\bar{y}_{max}}^{+\infty} |\bar{\psi}|^2 \, d\bar{x} d\bar{y}}. \tag{5.10}$$

If the superfluid field is 'left behind' due to the motion of the dislocation line, the distribution of $|\bar{\psi}|$ in the region $\bar{y} < \bar{y}_{max}$ will tend to increase while decreasing in the region $\bar{y} > \bar{y}_{max}$. The parameter B can therefore be used as a measure of asymmetry associated with the distribution of the superfluid field due to dislocation movement. The equilibrium solution shown in Fig. 5.4 i.e. $|\bar{\psi}(\bar{x} = 0, \bar{y}; \bar{t} = 0)|$ is asymmetric along the y direction and has a non zero value of the asymmetry parameter, $B(\bar{t} = 0) = B_0$. To study the change in asymmetry due to climb motion, we look at $B - B_0$ as a function of $\bar{t}$. Fig. 5.5 presents a plot of $B - B_0$ vs $\bar{t}$. The asymmetry of the superfluid field near the dislocation line and along the direction of motion increases due to climb. It is also seen that the rate of increment of parameter B slows as the dislocation line evolves for longer times. For higher climb velocities, more of the superfluid field tends to be 'left behind' compared to the slower velocities: faster moving dislocations are more efficient in leaving behind the superfluid field. The wavefunction at $\bar{y} = \bar{y}_{max}$ i.e. $|\bar{\psi}(\bar{x}, \bar{y} = \bar{y}_{max}; \bar{t})|$ shows that climb has no effect on the shape in the x direction. No change in superfluid field distribution is observed perpendicular to the direction of climb motion.

Next, glide motion of the dislocation line and the response of the superfluid field is considered. Eq. (5.7) is solved with the dislocation potential in Eq. (5.9) for glide along the positive x direction. The top panel of Fig. 5.6 shows $|\bar{\psi}(\bar{x}, \bar{y} = \bar{y}_{max}; \bar{t})|$ at $\bar{t} = 0$, 2196 and 6590 for $V_D = 5 \times 10^{-4}$. The superfluid field is carried along with the dislocation line. The maximum of $|\bar{\psi}|$ at $\bar{y} = \bar{y}_{max}$ shifts from $\bar{x} = 0$ to a value corresponding to $V_D \bar{t}$ referred to as $\bar{x}_{max}$. At $\bar{t} = 6590$, the maximum is expected to shift by $V_D \bar{t} = 3.3$ matching the results from the simulation. We look for evidence of asymmetry developing in the superfluid distribution due to glide motion. Glide evolution of $|\bar{\psi}|$ along x direction does not alter its symmetry characteristic: as can be seen in the bottom panel of Fig. 5.6.

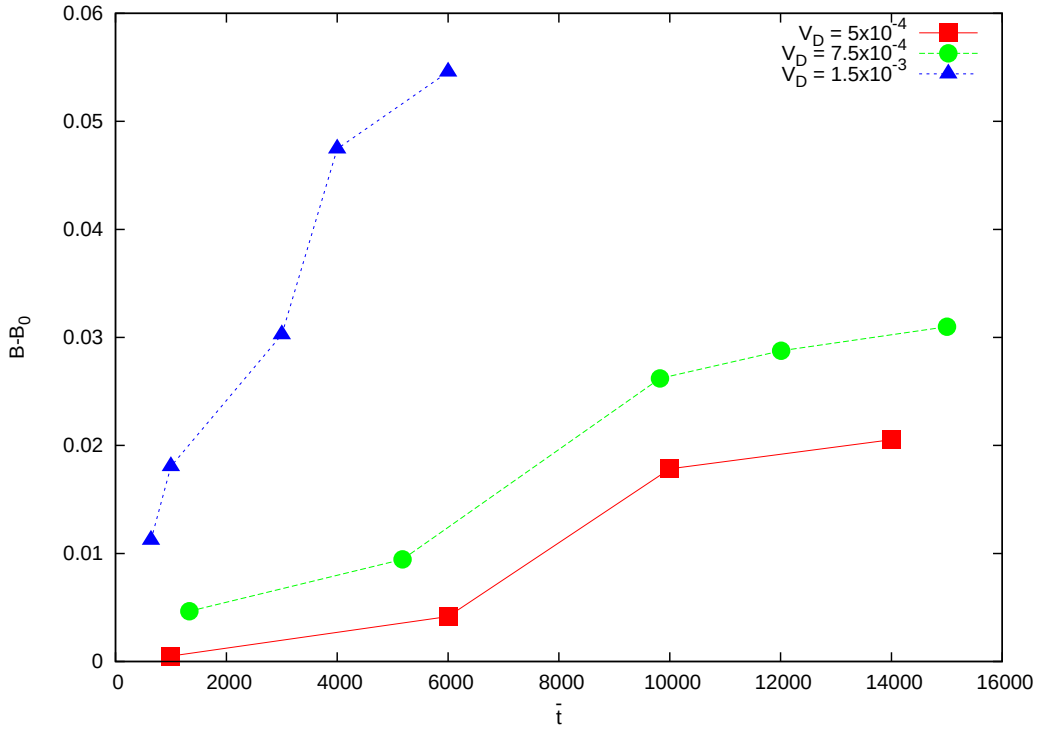

Figure 5.5: Plot of the asymmetry parameter $B - B_0$ at different times during climb motion is shown. $B - B_0$ vs $\bar{t}$ is plotted for three different values of V_D.

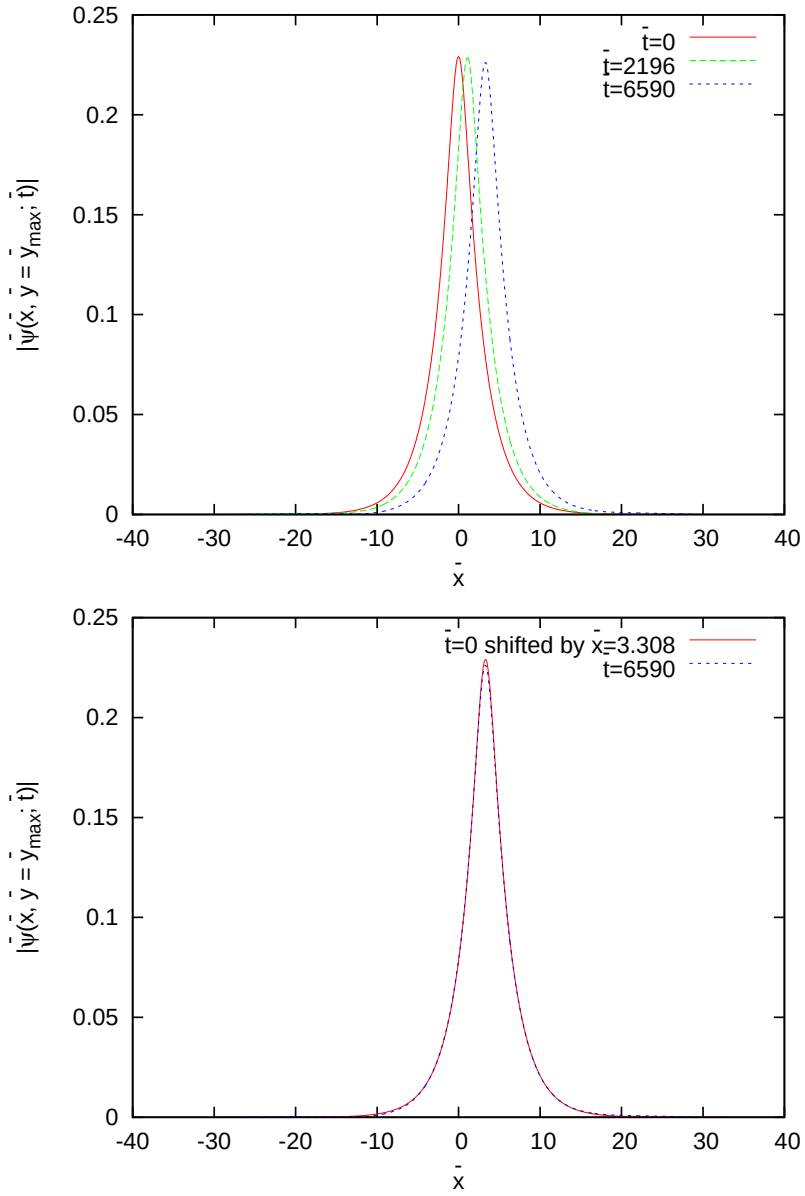

Figure 5.6: Plot of the wave function $|\bar{\psi}(\bar{x}, \bar{y} = \bar{y}_{max}; \bar{t})|$ for $\bar{t} = 0, 2196$ and 6590 during glide. $V_D = 5 \times 10^{-4}$ is used. In the bottom panel, the equilibrium $|\bar{\psi}(\bar{x} = \bar{x}_{max}, \bar{y}; \bar{t} = 0)|$ is offset by $\bar{x} = 3.308$ along the positive x direction in order to compare it to $|\bar{\psi}(\bar{x}, \bar{y} = \bar{y}_{max}; \bar{t} = 6590)|$.

The $\bar{y} = \bar{y}_{max}$ cross section of the equilibrium solution is shifted by $\bar{x} = 3.308$ in order to compare it to the time evolved $|\bar{\psi}(\bar{x}, \bar{y} = \bar{y}_{max}; \bar{t} = 6590)|$. This confirms that $|\bar{\psi}|$ along $\bar{y} = \bar{y}_{max}$ remains symmetric. The plot of $|\bar{\psi}|$ along the perpendicular direction at $\bar{x} = \bar{x}_{max}$ is presented in Fig. 5.7 for glide motion. We compare $|\bar{\psi}(\bar{x} = \bar{x}_{max}, \bar{y}; \bar{t})|$ at $\bar{t} = 0$ and 6590. No change in the asymmetry is observed.

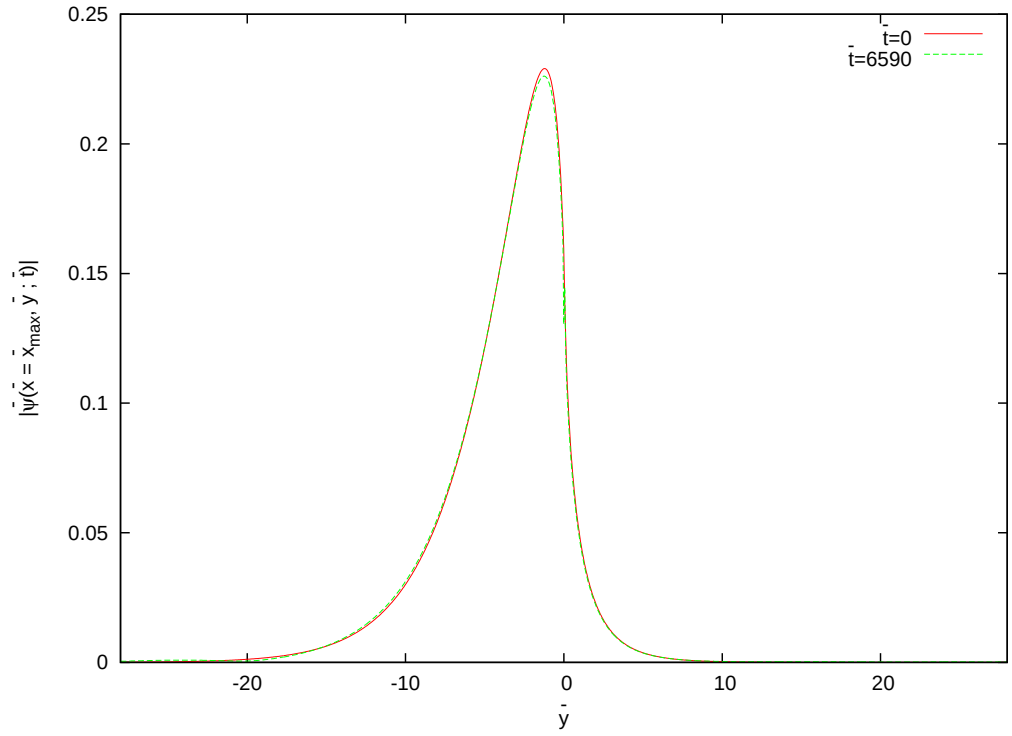

Figure 5.7: Plot of $|\bar{\psi}(\bar{x} = \bar{x}_{max}, \bar{y}; \bar{t})|$ at $\bar{t} = 0$ and $\bar{t} = 6590$ during glide for $V_D = 5 \times 10^{-4}$. No change in the asymmetry for $|\bar{\psi}|$ along $\bar{x} = \bar{x}_{max}$ is observed.

The time dependence of the total normalization of the wavefunction($\mathcal{N}$) is also studied. As noted earlier, the damping factor γ in the DGPE implies that $\mathcal{N}$ is not conserved. $\mathcal{N}$ for the superfluid field is observed to decrease for both climb and glide motion. Fig. 5.8 presents a plot of $\mathcal{N}$ vs $\bar{t}$ for climb and glide motion at different values of γ. The decay in $\mathcal{N}$ as a result of glide motion at $V_D = 5 \times 10^{-4}$ for $\gamma = 10^{-3}$ is too small to be seen and unimportant. An artificially larger value of $\gamma = 10^{-1}$ is used to amplify any possible decay effect. This results in a $\sim 5\%$ decay in $\mathcal{N}$ over a time interval of 800. Climb motion also results in the damping of superfluidity near an edge

dislocation line. At $\gamma = 10^{-3}$, again, the decay in $\mathcal{N}$ is minute. Using larger values for both $\gamma = 10^{-1}$ and $V_D = 0.0015$ the decay effect is much more visible. Approximately a 30% decay in $\mathcal{N}$ can now be observed over a time interval of 800. The physical origin of the decay in $\mathcal{N}$ can be roughly understood from the following arguments. Rewriting the DGPE in Eq. (5.6) as

$$i\hbar\frac{\partial\psi}{\partial t} = (1 - i\gamma)[H - \mu]\psi, \tag{5.11}$$

where $H = -\frac{\hbar^2}{2m}\nabla^2_{x,y} + v(x, y) + g|\psi|^2$ it can be seen from Eq. (5.4) that $H\psi = \mu(t)\psi$. By rescaling t in the equation above to $t' = (1 - i\gamma)t$ a solution of the form $\psi = \psi_0 e^{-i\Delta\mu(t)t'}$ is obtained where $\Delta\mu(t) = \mu(t) - \mu$ is the change in the effective chemical potential. This implies that

$$\psi = \psi_0 e^{-i(\mu(t)-\mu)t} e^{-\gamma(\mu(t)-\mu)t}, \tag{5.12}$$

where the damping contribution to ψ can be seen to depend on γ and $\mu(t) - \mu$. The motion of the dislocation line introduces excitations into the system thereby raising the $\mu(t)$. The quantity $\mu(t) - \mu$ in dimensionless units turns out to be roughly of order V_D. This is then responsible for the decay in the superfluid field amplitude.

5.4 Conclusion

In this chapter, the problem of an edge dislocation line moving at a constant velocity V_D and the response of an associated superfluid field is studied. Two types of dislocation motion are analyzed: climb and glide. Damping of the superfluid field due to dislocation motion is taken into account via the damping factor γ in the dissipative GPE as seen in Eq. (5.7). The split-step Crank-Nicolson method [151] is used to solve DGPE. The results give insight into how dislocation dynamics influences the superfluid distribution and its damping.

Initially, the equilibrium GPE with a stationary dislocation line was computed. Enhancement of superfluidity near a dislocation line is observed. The dislocation strain potential acts as a trap for the superfluid field and the equilibrium wave function $|\bar{\psi}(\bar{x}, \bar{y}; \bar{t} = 0)|$ reflects the symmetry characteristics of the strain potential: it is symmetric along $\bar{y} = \bar{y}_{max}$ and asymmetric along $\bar{x} = 0$. The superfluid field response to climb shows evidence of superfluidity being 'left behind' with the superfluid distribution

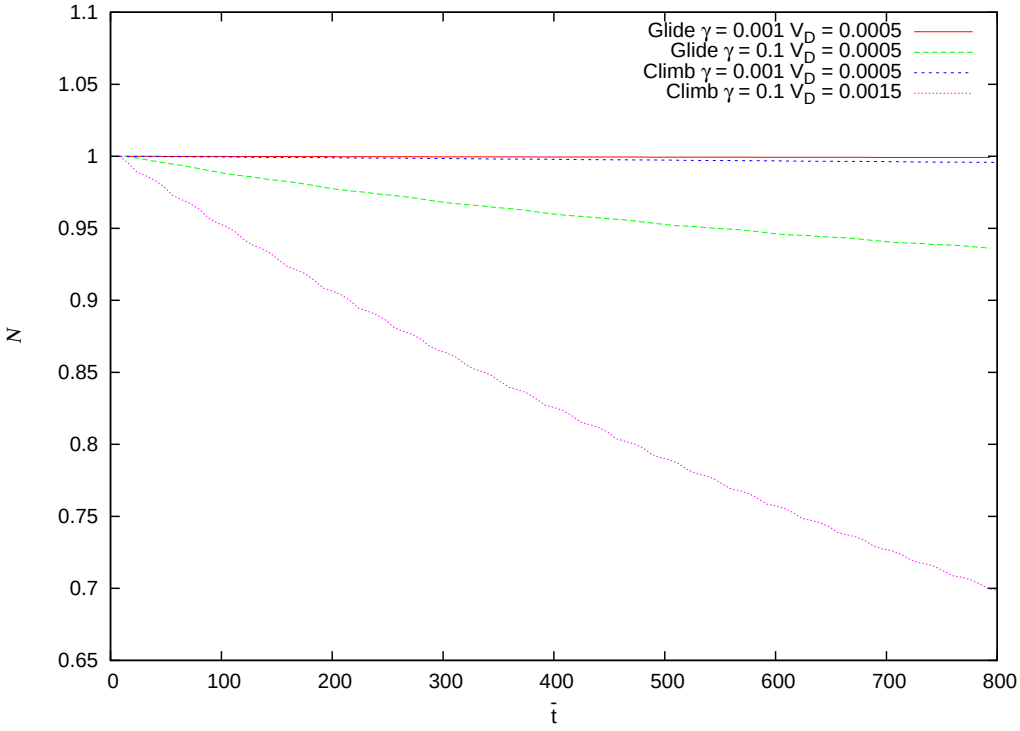

Figure 5.8: Plot of the total normalization $\mathcal{N}$ vs $\bar{t}$. Two different values of $\gamma = 10^{-3}$ and 10^{-1} are used for both climb and glide. Change in $\mathcal{N}$ due to $V_D = 1.5 \times 10^{-3}$ for climb at $\gamma = 10^{-1}$ is also shown.

becoming more asymmetric along the direction of climb. An asymmetry parameter B is used to quantify the superfluid field being 'left behind.' The parameter B increases as a function of time: it rises quickly at shorter times and flatten as the dislocation line evolves over longer time. Study of different climb velocities led to the conclusion that the magnitude of the asymmetry parameter B is proportional to how fast the dislocation line moves. For glide motion, the symmetry characteristics of the wave function along $\bar{x} = \bar{x}_{max}$ and $\bar{y} = \bar{y}_{max}$ are analyzed. No change in superfluid distribution symmetry characteristics are noted along the direction of motion unlike climb motion.

Both dislocation climb and glide lead to a small decay in $\mathcal{N}$ for the physical value of $\gamma = 10^{-3}$ considered in this study. Using a larger value of $\gamma = 10^{-1}$, an amplified decay effect can be observed. The asymmetry induced in the superfluid distribution due to climb is the most prominent physical effect observed in this study. During glide, however, no change in the superfluid field asymmetry characteristics is observed.

Chapter 6

Conclusion

In this thesis, a study of the interplay of dislocation line and superfluid field is presented at different levels of coarse-graining. In Chapter 2, a coarse-grained model of the behavior of superfluid field associated with dislocation lines in crystal ^{4}He was studied by looking at the hydrodynamics of superfluids confined to complex geometries. In Chapter 5, a quantum model for the effect of dislocation dynamics on the superfluid field within the Gross-Pitaevskii formalism was considered. Other models spanning different levels of coarse-graining in between the hydrodynamic model and the quantum GP model were also brought to bear on the problem of how dislocation dynamics affects the superfluid field near it.

To study the hydrodynamics of compressible superfluids in confined geometries, an analytic method is implemented in a perturbative manner in Chapter 2 with the relevant dimensionless parameter being the square of the ratio of the typical speed to the sound speed. This method is expected to complement numerical calculations based on more microscopic descriptions such as the GP equation and will be particularly useful in the study of cold atomic systems. It was shown that starting directly from the hydrodynamic equations, in the appropriate limit, is a good alternative to using the full GP equations. While compressibility corrections for superfluid ^{4}He were negligible, for practical cases of interest in cold atomic systems confined to complex geometries the corrections to the zero compressibility results are relevant.

A coupled field random Ising model with either quenched or annealed disorder is used in Chapter 3 to compare the shift in the superfluid transition temperature due to

the dynamics of a dislocation network. This network consists of four-fold coordinated Ising spins connected by spin chains. Real networks do evolve in time and the assumption of quenched disorder would be valid when the time scale over which the network changes is orders of magnitude larger than the time scale of the spin fluctuations. If these two time scales are comparable to each other, or at least not too different, then the disorder should be considered to be *annealed*. Based on this model, it is shown that the transition temperature for the Ising model on a random network in which the disorder is quenched (frozen) is always higher than the transition temperature for annealed disorder with the same distribution. The magnitude of the difference between the two transition temperatures is quantified by our study. The entropy associated with the one dimensional fluctuations is shown to be larger for the quenched case. Our model may be relevant also to the renewed interest on dislocation networks in solid ^{4}He. It presents a simplified version of the effect that dynamics of a dislocation network may have on the superfluid field in its vicinity. Our results indicate that in the annealed scenario when the time scale for dislocation line fluctuations becomes comparable to or smaller than the time scale associated with fluctuations of the superfluid field i.e. when fluctuations of dislocation line segments within a dislocation network become important the associated phase transition is subdued. On the other hand, superfluid ordering is observed to be enhanced in the vicinity of a dislocation if the dislocation network is considered to be frozen.

Moving towards less coarse-grained models of superfluidity associated with a dislocation line, I looked at the relation between the anomalous shear modulus effect in solid ^{4}He and the presence of a superfluid field in Chapter 4. Insight into how the motion of a dislocation line is affected by superfluidity in its vicinity was gained based on the superfluid contribution to the mobility co-efficient of a dislocation line. Based on general approach seen in [32] and [128] to calculate the mobility, the rate of work done by a force applied on the dislocation line, which causes the line to move with a constant speed V_D, was equated to the energy dissipation rate due to the fields associated with the dislocation line motion. The procedure [32] previously employed to compute the dislocation mobility in quasicrystals was extended, combined with the usual hydrodynamic equations [33, 34] for quantum crystals, to calculate the mobility of an edge dislocation line

in the presence of a surrounding superfluid field. The result for the mobility of the dislocation line is expressed in terms of the bulk "second viscosities" of the superfluid crystal hydrodynamics, and the value of ρ_s (the superfluid density). Numerical estimates of the mobility, although rather uncertain, indicate that an assumed superfluid field in the vicinity of dislocation lines, may play an important role in dislocation mobility and therefore in the stiffness of the crystal. An important consequence of this observation is that superfluid damping of dislocation motion can model the large and sudden increase in shear modulus observed experimentally in solid ^{4}He as the temperature is lowered. Our results also show that quenching of dislocation motion due to a superfluid field could be the dominant source of damping for dislocation motion in the low temperature limit. Numerical estimates of the change in shear modulus and the Q factor based on this effect models experimental behavior quite well.

The response of the superfluid field to the dynamics of the dislocation line was examined using a quantum model in Chapter 5. Based on the Gross-Pitaevskii formalism and the Dissipative Gross-Pitaevskii Equation (DGPE), how the superfluid field reacts to glide and climb motion of an edge dislocation was considered. Climb motion of the dislocaton line led to superfluidity being 'smeared' over a wider region: the superfluid field distribution tended to be more asymmetric as the dislocation line moved over longer times and distances. The higher the climb velocity of the dislocation line, the more pronounced the smearing of the associated superfluid field. Only a very small decay of superfluid amplitude was observed for both climb and glide motion. Higher dislocation glide velocities led to stronger damping of the associated superfluid field. A marked difference between climb and glide motion in how they affect the asymmetry properties of the superfluid distribution was observed.

Given the broad interest on the physics of dislocations within solids, effect of dislocation dynamics on superfluidity within solid ^{4}He is examined at different levels of coarse-graining. The hydrodynamics of compressible superfluid confined to complex geometries was studied in order to understand the flow behavior of superfluidity associated with dislocation networks. A perturbative analytic method was implemented for this purpose and the effect of compressibility on flow properties was documented. A study on the effect of the dynamics of the network of dislocation line was implemented via a coupled field random Ising model. The difference induced by quenched vs annealed

network of dislocation lines on the associated superfluid ordering led to the conclusion that dynamics of the dislocation line can indeed play an important role. Next, the effect of the superfluid field on the motion of the dislocation line was analyzed: with the evidence pointing to superfluid field making it harder for the dislocation line to move. This result was shown to be in good agreement with the experimentally observed anomalous shear modulus effect and dissipation at low temperatures. The effect of the dynamics of a dislocation line on the superfluid field was studied at the quantum level i.e. short time and length scales. The expected 'smearing' response of the superfluid field due to the movement of the dislocation line is quantified via an asymmetry parameter B.

In conclusion, the interplay of the superfluid field and edge dislocation lines within a quantum crystal was studied at different levels of coarse-graining. Results show that the dynamics of dislocation lines can have important consequences: it influences the elastic properties of solid ^{4}He, affects the superfluid transition temperature and dictates the presence and spatial distribution of the superfluid field.

References

[1] P.L. Kapitza, Nature **141** 74, (1938).

[2] J. F. Allen and A. D. Misener. Nature **141**, 75 (1938).

[3] Advanced information on the Nobel Prize in Physics, 7 October (2003).

[4] G.B. Hess, W.M. Fairbank. Phys. Rev. Lett. **19** 216, (1967).

[5] K. Huang. Statistical Mechanics (2nd Edition), Page 307.

[6] D.I.Khomskii.Basic Aspects of the Quantum Theory of Solids: Order and Elementary Excitations, Page 50.

[7] F. London. Superfluids Vol. II (1954).

[8] G.V. Chester. Phys. Rev. A, **2** 256, (1970).

[9] A.J. Leggett, Phys. Rev. Lett. **25**, 15431546 (1970).

[10] M.W. Meisel, Physica B **178**, 121 (1992).

[11] E. Kim and M. H. W. Chan. Nature **427**, 225 (2004).

[12] J. Beamish, Physics **3**, 51 (2010).

[13] D.Y. Kim and M.H.W. Chan. Phys. Rev. B **90**, 064503 (2014).

[14] I. Iwasa. Phys. Rev. B **81**, 104527 (2010).

[15] Z. Nussinov, A.V. Balatsky, M.J. Graf and S.A. Trugman. Phys. Rev. B **76**, 014530 (2007).

[16] Y. Vekhov and R.B. Hallock. Phys. Rev. B **91**, 180506(R) (2015).

[17] M.W. Ray and R.B. Hallock. Phys. Rev. Lett. **100**, 235301 (2008).

[18] A.T. Dorsey, P.M. Goldbart and J. Toner, Phys. Rev. Lett. **96**, 055301 (2006).

[19] D. Hull and D.J. Bacon. Introduction to Dislocations. Fourth Edition, Page 17.

[20]] I. Iwasa and H. Suzuki, J. Phys. Soc. Jpn. **49**, 1722 (1980).

[21] X. Rojas, A. Haziot, V. Bapst, S. Balibar and H.J. Maris. Phys. Rev. Lett. **105**, 145302 (2010).

[22] S. Balibar, Nature (London) **464**, 08913 (2010); Physics **3**, 39 (2010).

[23] A.C. Clark. PhD Thesis, The Pennsylvania State University, August (2007).

[24] S.I. Shevchenko, Sov. J. Low Temp. Phys **14**, 553 (1988).

[25] L. Pollet, M. Boninsegni, A.B. Kuklov, N.V. Prokofev, B.V. Svistunov and M. Troyer. Phys. Rev. Lett. **98**, 135301 (2007).

[26] M. Boninsegni, A.B. Kuklov, L. Pollet, N.V. Prokof'ev, B.V. Svistunov and M. Troyer, Phys. Rev. Lett. **99**, 035301 (2007).

[27] S.G. Soyler, A.B. Kuklov, L. Pollet, N.V. Prokof'ev and B.V. Svistunov. Phys. Rev. Lett. **103**, 175301 (2009).

[28] V. M. Nabutovskii and V. Ya. Shapiro, Sov. Phys. JETP, **48**, 480 (1978).

[29] J. Toner, Phys. Rev. Lett. **100**, 035302 (2008).

[30] L.D. Landau and E.M. Lifshitz, Theory of Elasticity, Third Edition, (1986).

[31] C. Dasgupta and O.T. Valls, Phys. Rev. E **79**, 016303 (2009).

[32] T.C. Lubensky, S. Ramaswamy and J. Toner. Phys. Rev. B **33**, 11 (1986).

[33] A.F. Andreev and I.M. Lifshitz. Sov. Phys. JETP, **29**, 6 (1969).

[34] W.M. Saslow. Phys. Rev. B **15**, 173 (1977); J. Low Temp. Phys. **169**, 248-263 (2012).

[35] W. Ketterle, D.S. Durfee and D.M. Stamper-Kum, arXiv/cond-mat/9904034 (1999).

[36] F. Dalfovo, S. Giorgini, L. P. Pitaevskii and S. Stringari, Rev. Mod. Phys. **71**, 463 (1999); S. Giorgini, L.P. Pitaevskii and S. Stringari, *ibid* **80**, 1215 (2008).

[37] O. Morsch and M. Oberthaler, Rev. Mod. Phys. **78**, 180, (2006).

[38] R. Onofrio, C. Raman, J.M. Vogels, J.R. Abo-Shaeer, A.P. Chikkatur and W. Ketterle, Phys. Rev. Lett. **85**, 2228 (2000).

[39] O.M. Marago, S.A. Hopkins, J. Arlt, E. Hodby, G. Hechenblaikner, and C. J. Foot, Phys. Rev. Lett. **84**, 2056 (2000).

[40] C. Ryu, M.F. Andersen, P. Clade, V. Natarajan, K. Helmerson and W.D. Phillips, Phys. Rev. Lett. **99**, 260401 (2007).

[41] K. W. Madison, F. Chevy, W. Wohleben and J. Dalibard, Phys. Rev. Lett. **84**, 806 (2000).

[42] B. Clancey, L. Luo and J.E. Thomas, Phys. Rev. Lett. **99**, 140401 (2007).

[43] A. Ramanathan, K.C. Wright, S.R. Muniz, M. Zelan, W.T. Hill III, C.J. Lobb, K. Helmerson, W.D. Phillips and G. K. Campbell, Phys. Rev. Lett. **106**, 130401 (2011).

[44] R.B. Blakestad, C. J. Lobb, W. D. Phillips, and G. K. Campbell, Phys. Rev. Lett. **110**, 025302 (2013).

[45] For a review, see S. Balibar and F. Caupin, J. Phys. Condens. Matter **20**, 173201 (2008).

[46] D. Kim and M. Chan, Phys. Rev. Lett.**109**, 155301 (2012).

[47] C. Dasgupta and O.T. Valls, Phys. Rev. B **82**, 024523 (2010).

[48] A. L. Fetter, J. Low Temp. Phys. **16**, 533 (1974).

[49] A.L. Fetter, Phys. Rev. **152**, 183 (1966).

[50] D. E. Sheehy and L. Radzihovsky, Phys. Rev. A **70**, 063620 (2004).

[51] A. L. Fetter, Rev. Mod. Phys. **81**, 647 (2009).

[52] C.J. Pethick and H. Smith, *Bose-Einstein Condensation in Dilute Gases*, Cambridge University Press, Cambridge, England (2002).

[53] See, for example, footnote [15] in S. Stringari, Phys. Rev. Lett. **77**, 2360 (1996).

[54] Chi-Tuong Pham, Caroline Nore, M.-É. Brachet, Physica D: Nonlinear Phenomena, **210**, 203 (2005).

[55] Sergio Rica, Physica D: Nonlinear Phenomena, **148**, 221 (2001).

[56] V. Bretin, S. Stock, Y. Seurin, and J. Dalibard, Phys. Rev. Lett. **92**, 050403 (2004).

[57] A. Aftalion and P. Mason, Phys. Rev. A **81**, 023607 (2010).

[58] L. Rayleigh, *The Theory of Sound*, Macmillan and Co, London (1877).

[59] C. Eckart, Phys. Rev. **73**, 68-76 (1948).

[60] S. Inouye, S. Gupta, T.Roseband, A.P. Chikkatur, A.Gorlitz, T.L. Gustavson, A.E. Leanhardt, D.E Pritchard and W.Ketterle, Phys. Rev. Lett. **87**, 080402 (2001).

[61] R. Desbuquois, L. Chomaz, T. Yefsah, J. Leonard, J. Beugnon, C. Weitenberg and J. Dalibard, Nature Physics **8**, 645-648 (2012).

[62] A.L. Fetter, C.J. Foot, `arXiv:1203.3183[cond-mat.quant-gas]` (2012).

[63] See Page 89 in M. Ueda, *Fundamentals and New Frontiers of Bose-Einstein Condensation*, World Scientific Publishing Co., Singapore (2010).

[64] James A. Joseph, PhD Thesis, Duke University, (2010).

[65] J.C. Findlay, A. Pitt, H.G. Smith, J.O. Wilhelm, Phys. Review, **54**,7 (1938).

[66] See page 142 in J. D. Jackson , *Classical Electrodynamics*, 3rd Edition, Wiley, New York (1999).

[67] C. Raman, M.Kohl, R.Onofrio, D.S. Durfee, C.E. Kuklewicz, Z.Hadzibabic and W. Ketterle, Phys. Rev. Lett. **83**, 2502-2505 (1999).

[68] T.C. Lubensky, in Ill Condensed Matter, Les Houches Session XXXI, Edited by R Balian, R Maynard and G Toulouse (North Holland, Amsterdam, 1979).

[69] R.B. Stinchcombe, in Phase Transitions and Critical Phenomena Vol. 7, edited by C. Domb and J.L. Lebowitz (Academic, New York, 1983).

[70] D. Stauffer and A. Aharony, Introduction to Percolation Theory, 2nd edition (Taylor and Francis, Philadelphia, 1994).

[71] A. S. Skal and B. I. Shklovskii, Fiz. Tekh. Poluprovodn. **8**, 1582 (1974) [Sov. Phys.-Semicond. **8**, 1029 (1975)].

[72] C. Dasgupta, A. B. Harris, and T. C. Lubensky, Phys. Rev. B **17**, 1375 (1978).

[73] Y. Gefen, A. Aharony and B.B. Mandelbrot, J. Phys. A **17**, 435 (1984).

[74] R.B. Stinchcombe, Phys. Rev. B **41**, 2510 (1990)

[75] R. Albert and A.-L. Barabasi, Rev. Mod. Phys. **74**, 47 (2002).

[76] S. N. Dorogovtsev and J. F. F. Mendes, Adv. Phys. **51**, 1079 (2002).

[77] S. N. Dorogovtsev and J. F. F. Mendes, Evolution of Networks: From Biological Nets to the Internet and WWW (Oxford University Press, Oxford, 2003).

[78] G. Fagiolo and M. Mastrorillo. Phys. Rev. E **88**, 012812 (2013).

[79] M. Boguna, C. Castellano, R. Pastor-Satorras. Phys. Rev. Lett. **111**, 068701 (2013).

[80] D.J.Watts and S.H.Strogatz, Nature (London) **393**,440 (1998).

[81] A.-L.Barabasi and R. Albert, Science **286**, 509 (1999).

[82] A. Majdandzic, B. Podobnik, S.V. Buldyrev, D.Y. Kenett, S. Havlin and H.E. Stanley. Nature Physics **10**, 34-38 (2014).

[83] A. V. Goltsev, S. N. Dorogovtsev, and J. F. F. Mendes, Phys. Rev. E **67**, 026123 (2003).

[84] S. N. Dorogovtsev, A. V. Goltsev and J. F. F. Mendes, Phys. Rev. E **66**, 016104 (2002).

[85] M. Leone, A. Vazquez, A. Vespignani, R. Zecchina, Eur. Phys. J. B **28**, 191 (2002).

[86] C. P. Herrero, Phys. Rev. E **77**, 041102 (2008).

[87] D.-H. Kim, G. J. Rodgers, B. Kahng, and D. Kim, Phys. Rev. E **71**, 056115 (2005).

[88] T. Hasegawa and K. Nemoto. Phys. Rev. E **80**, 026126 (2009).

[89] F. Igloi and L. Turban, Phys. Rev. E 66, 036140 (2002).

[90] S. N. Dorogovtsev, A. V. Goltsev, and J. F. F. Mendes, Eur. Phys. J. B **38**, 177 (2004).

[91] B. J. Kim, H. Hong, P. Holme, G. S. Jeon, P. Minnhagen, and M. Y. Choi, Phys. Rev. E **64**, 056135.

[92] M.I. Berganza and L. Leuzzi, Phys. Rev. B **88**, 144104 (2013).

[93] F.W.S Lima and J.A. Plascak, J. Phys.: Conf. Ser. **487**, 012011 (2014).

[94] R.F.S. Andrade, J.S. Andrade Jr. and H.J. Herrmann, Phys. Rev. E **79**, 036105 (2009).

[95] M. Serva, U. L. Fulco and E. L. Albuquerque, Phys. Rev. E **88**, 042823 (2013).

[96] A. B. Harris, J. Phys. C **7**, 1671 (1974).

[97] M. E. Fisher, Phys. Rev. **176**, 257 (1968).

[98] M.F. Thorpe and D. Beeman, Phys. Rev. B **14**, 188 (1976).

[99] H. Falk, J. Phys. C: Solid State Phys., **9**, L213 (1976).

[100] M.F. Thorpe, J. Phys. C: Solid State Phys., **11**, 2983 (1978).

[101] S. Balibar and F. Caupin, J. Phys. Condens. Matter **20**, 17320 (2008).

[102] C. Dasgupta and O.T. Valls, Phys. Rev. B **82**, 024523 (2010).

[103] V.M. Galitski, A. Kaminski, and S. Das Sarma, Phys. Rev. Lett. **92**, 177203 (2004).

[104] A. Kaminski and S. Das Sarma, Phys. Rev. Lett. **88**, 247202 (2002).

[105] I. Ya. Korenblit, E. F. Shender and B. I. Shklovskii, Phys. Lett. **A 46**, 275 (1973).

[106] R. N. Bhatt and P. A. Lee, Phys. Rev. Lett. **48**, 344 (1982).

[107] D. Aleinikava, E. Dedits, A.B. Kuklov and D. Schmeltzer, Europhys. Lett. **89**, 46002 (2010).

[108] J.H. Hetherington. Phys. Rev. **176**, 231 (1968).

[109] E.Polturak and N.Gov, Contemporary Physics 44, No.2, 145-151, (2003).

[110] A.S.C. Rittner and J.D. Reppy. Phys. Rev. Lett. **98**, 175302 (2007).

[111] J. Day and J. Beamish. Nature (London) **450**, 853 (2007).

[112] J. Day, O. Syshchenko and J. Beamish. Phys. Rev. B **79**, 214524 (2009).

[113] I. Iwasa. J. Low Temp. Phys. **171**, 287 (2013).

[114] A.D. Fefferman, F. Souris, A. Haziot, J.R. Beamish and S. Balibar. Phys. Rev. B **89**, 014105(2014).

[115] C. Zhou, J-J. Su, M.J. Graf, C. Reichhardt, A.V. Balatsky, I.J. Beyerlein. Philos. Mag. Lett. **92** (11), 608-616 (2012).

[116] C. Zhou, J-J. Su, M.J. Graf, C. Reichhardt, A.V. Balatsky, I.J. Beyerlein. Phys. Rev. B **88**, 024513 (2013).

[117] A.B. Kuklov, L. Pollet, N.V. Prokof'ev and B.V. Svistunov. Phys. Rev. B **90**, 184508 (2014).

[118] F. Souris, A.D. Fefferman, A. Haziot, N. Garroum, J.R. Beamish and S. Balibar. J. Low Temp. Phys. **178**, 149-161 (2015).

[119] X. Rojas, C. Pantalei, H.J. Maris and S. Balibar. J. Low Temp. Phys. **158**, 478-484 (2010).

[120] A. N. Malmi-Kakkada, O.T. Valls and C. Dasgupta. Phys. Rev. B. **90**, 024202 (2014).

[121] A. Haziot, A.D. Fefferman, F. Souris, J.R. Beamish and S. Balibar. Phys. Rev. B **87**, 060509 R(2013).

[122] A. Haziot, A.D. Fefferman, F. Souris, J.R. Beamish and S. Balibar. Phys. Rev. Lett. **110**, 035301(2013).

[123] H. Suzuki. J. Phys. Soc. Jpn. **35**, 1472 (1973).

[124] H. Suzuki. J. Phys. Soc. Jpn. **42**, 1865 (1977).

[125] J. A. Gorman, D. S. Wood and T. Vreeland, Jr. J. Appl. Phys. **40**, 2 (1969).

[126] J. Day, O. Syshchenko and J. Beamish. Phys. Rev. Lett. **104**, 075302 (2010).

[127] O. Syshchenko, J. Day and J. Beamish. Phys. Rev. Lett. **104**, 195301 (2010).

[128] G.N. Lazareva and A.S. Bakai. J. Phys.:Condens. Matter **21**, 295401 (2009).

[129] The first of Eqs. (4.8) differs slightly from the corresponding expression in the first of Ref. [34]. That expression contains a small error, which we are very grateful to Prof. Saslow for pointing out to us.

[130] G.I. Taylor. Proc. R. Soc. Lond. A **145**, 362 (1934).

[131] E. Orowan. Proc. Phys. Soc. **52**, 8 (1940).

[132] A. Granato and K. Lucke. J. Appl. Phys. **27**, 583 (1956). We consider the limit whereby the effective mass per unit length as well as the effective tension per unit length of the dislocation line is negligible.

[133] The acceleration time constant is given by the ratio of mass per unit length to the inverse mobility of the dislocation line. This time constant is very small $\sim 10^{-13}$ sec.

[134] A. D. B. Woods and A. C. Hollis Hallett. Can. J. Phys. **41**, 596-609 (1962).

[135] J. T. Tough, W. D. McCormick, and J. G. Dash. Phys. Rev. **132**, 2373-2378 (1963).

[136] S. Putterman. Phys. Rev. Lett. **26**, No. 8 (1971).

[137] C-I Um. Technical Report - Office of Naval Research (1992).

[138] D. Aleinikava, E. Dedits and A.B. Kuklov. J Low Temp Phys. **162**: 464-475 (2011).

[139] M. H. W. Chan, K. I. Blum, S. Q. Murphy, G. K. S. Wong, J. D. Reppy. Phys. Rev. Lett. **61**, 1950(1988).

[140] A. Haziot, A.D. Fefferman, F. Souris, J.R. Beamish and S. Balibar. Phys. Rev. B **88**, 014106(2013).

[141] A.S.C. Rittner, PhD Thesis, Cornell University, May (2008).

[142] N.V. Prokof'ev and B.V. Svistunov. Phys. Rev. Lett. **94**, 155302 (2005).

[143] D. Goswami, K. Dasbiswas, C.-D. Yoo, and A.T. Dorsey. Phys. Rev. B **84**, 054523(2011).

[144] E.P. Gross. Nuovo Cimento **20** 3(1961).

[145] L.P. Pitaevskii. Sov. Phys. JETP **13** 2(1961).

[146] L.P. Pitaevskii. Sov. Phys. JETP. **35**, 282(1959).

[147] S. Choi, S.A. Morgan, and K. Burnett. Phys. Rev. A **57**, 4057(1998).

[148] A. H. Cottrell and M. A. Jaswon, Proc. R. Soc. London, Ser. A. **199**, 104(1949).

[149] K. Kasamatsu, M. Tsubota and M. Ueda. Phys. Rev. A. **67**, 033610 (2003).

[150] N.P. Proukakis, N.G. Parker, C.F. Barenghi C F and C.S. Adams. Phys. Rev. Lett. **93**, 130408(2004).

[151] P. Muruganandam and S. K. Adhikari, Comput. Phys. Commun. **180**, 1888(2009).

[152] Z. Hadzibabic, P. Kruger, M. Cheneau, S.P. Rath and J. Dalibard. New Jour. of Phys. **10**, 045006(2008).

[153] I. Bloch, J. Dalibard and W. Zwerger. Rev. Mod. Phys. **80**, 885(2008).

[154] M. Boninsegni and N.V. Prokofev. Rev. Mod. Phys. **84**, 759(2012).

[155] K. Dasbiswas, D. Goswami, C.-D. Yoo and A.T. Dorsey. Phys. Rev. B **81**, 064516(2010).

[156] D. Hull and D.J. Bacon. Introduction to Dislocations. Fourth Edition, Page 70.

[157] R. A. Aziz. Inert Gases (M. L. Klein, ed.). Springer-Verlag, (1984).